Ultrafast Structural Dynamics in $4H_b$-$TaSe_2$ observed by Femtosecond Electron Diffraction

by

Nicolas Erasmus

Dissertation presented for the degree of
Doctor of Philosophy in Physics
at Stellenbosch University

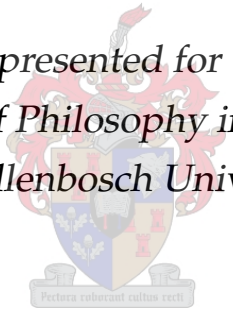

Department of Physics,
University of Stellenbosch,
Private Bag X1, Matieland 7602, South Africa.

Supervisors:

Prof. Heinrich Schwoerer
Prof. Erich Rohwer

March 2013

Stellenbosch University http://scholar.sun.ac.za

Stellenbosch University http://scholar.sun.ac.za

Declaration

By submitting this thesis/dissertation electronically, I declare that the entirety of the work contained therein is my own, original work, that I am the sole author thereof (save to the extent explicitly otherwise stated), that reproduction and publication thereof by Stellenbosch University will not infringe any third party rights and that I have not previously in its entirety or in part submitted it for obtaining any qualification.

Copyright © 2013 Stellenbosch University
All rights reserved.

Stellenbosch University http://scholar.sun.ac.za

Stellenbosch University http://scholar.sun.ac.za

Abstract

Ultrafast Structural Dynamics in $4H_b$-$TaSe_2$ observed by Femtosecond Electron Diffraction

N. Erasmus

Department of Physics,
University of Stellenbosch,
Private Bag X1, Matieland 7602, South Africa.

Dissertation: PhD Physics

March 2013

In this thesis the structural dynamics, upon photo-excitation, of the charge-density-wave (CDW) material $4H_b$-$TaSe_2$ is investigated on the time-scale of atomic motion and simultaneously on the spatial-scale of atomic dimensions.

CDW materials have been of interest since their discovery in the 1970's because of their remarkable non-linear and anisotropic electrical properties, gigantic dielectric constants, unusual elastic properties and rich dynamical behaviour. Some of these exotic properties were extensively investigated in thermal equilibrium soon after their discovery but only recently have ultrafast techniques like femtosecond spectroscopy become available to study their out-of-equilibrium behaviour on the time-scale of atomic motion. By studying their behaviour on this time-scale a more in-depth understanding of their macroscopic properties can be gained. However, to do investigations on the atomic time-scale and simultaneously directly observe the evolution of the atomic arrangements is another challenge. One approach is through the previously mentioned technique of femtosecond pump-probe spectroscopy but converting the usual ultrashort optical probing source to an ultrashort electron or x-ray source that can diffract off the sample and reveal structural detail on the atomic level.

Stellenbosch University http://scholar.sun.ac.za

Here, the femto-to-picosecond out-of-equilibrium behaviour upon photo-excitation in $4H_b$-$TaSe_2$ is investigated using an ultrashort electron probe source. Two variations of using an electron probe source are used: conventional scanning Femtosecond Electron Diffraction (FED) and a new approach namely Femtosecond Streaked Electron Diffraction (FSED). The more established FED technique, based on femtosecond pump-probe spectroscopy, is used as the major investigating tool while the FSED technique, based on ultrafast streak camera technology, is an attempt at broadening the scope of available techniques to study structural dynamics in crystalline material on the sub-picosecond time-scale.

With these two techniques, the structural dynamics during the phase transition from the commensurate- to incommensurate-CDW phase in $4H_b$-$TaSe_2$ is observed through diffraction patterns with a temporal resolution of under 500 fs. The study reveals strong coupling between the electronic and lattice systems of the material and several time-constants of under and above a picosecond are extracted from the data. Using these time-constants, the structural evolution during the phase transition is better understood and with the newly gained knowledge, a model of all the processes involved after photo-excitation is proposed.

Stellenbosch University http://scholar.sun.ac.za

Uittreksel

Die waarneming van Ultravinnige Strukturele Dinamika in $4H_b$-$TaSe_2$ deur middel van Femtosekonde Electron Diffraksie

("Ultrafast Structural Dynamics in $4H_b$-$TaSe_2$ observed by Femtosecond Electron Diffraction")

N. Erasmus

Departement van Fisika,
Universiteit van Stellenbosch,
Privaatsak X1, Matieland 7602, Suid Afrika.

Proefskrif: PhD Fisika

Maart 2013

In hierdie tesis word die strukturele dinamika van die lading-digtheid-golf (LDG) materiaal $4H_b$-$TaSe_2$ ondersoek op die tydskaal van atomiese bewegings en gelyktydig op die ruimtelikeskaal van atomiese dimensies.

LDG materie is al van belang sedert hul ontdekking in die 1970's as gevolg van hul merkwaardige nie-lineêre en anisotrope elektriese eienskappe, reuse diëlektriese konstantes, ongewone elastiese eienskappe en ryk dinamiese gedrag. Sommige van hierdie eksotiese eienskappe is omvattend ondersoek in termiese ewewig kort na hul ontdekking, maar eers onlangs is dit moontlik deur middle van ultravinnige tegnieke soos femtosekonde spektroskopie om hulle uit-ewewigs gedrag te bestudeer op die tydskaal van atomiese beweging. Deur die gedrag op hierdie tydskaal te bestudeer kan 'n meer insiggewende begrip van hul makroskopiese eienskappe verkry word. Om ondersoeke in te stel op die atomiese tydskaal en gelyktydig direk die evolusie van die atoom posisie te waarneem is egter 'n moeilike taak. Een benadering is deur middle van femtosekonde "pump-probe" spektroskopie maar dan die gewone optiese "probe" puls om te skakel na 'n electron of x-straal puls wat van die materiaal kan diffrak en dus strukturele inligting op die atomiese vlak kan onthul.

Stellenbosch University http://scholar.sun.ac.za

Hier word die femto-tot-pico sekonde uit-ewewig gedrag in $4H_b$-$TaSe_2$ ondersoek met behulp van elektron pulse. Twee variasies van die gebruik van 'n elektron bron word gebruik: konvensionele "Femtosecond Electron Diffraction" (FED) en 'n nuwe benadering, naamlik, "Femtosecond Streaked Electron Diffraction" (FSED). Die meer gevestigde FED tegniek, wat gebaseer is op femtosekonde "pump-probe" spektroskopie, word gebruik as die hoof ondersoek metode terwyl die FSED tegniek, wat gebaseer is op die ultra vinnige "streak camera" tegnologie, 'n poging is om beskikbare tegnieke uit te brei wat gebruik kan word om strukturele dinamika in materie te bestudeer op die sub-picosekonde tydskaal.

Met behulp van hierdie twee tegnieke, word die strukturele dinamika tydens die fase oorgang van die ooreenkomstige tot nie-ooreenkomstige LDG fase in $4H_b$-$TaSe_2$ deur diffraksie patrone met 'n tydresolusie van minder as 500 fs waargeneem. Die studie toon 'n sterk korrelasie tussen die elektroniese sisteem en kristalrooster. Verskeie tydkonstantes van onder en bo 'n picosekonde kon ook uit die data onttrek word en gebruik word om die strukturele veranderinge beter te verstaan. Hierdie nuwe kennis het ons in staat gestel om 'n model van al die betrokke prosesse voor te stel.

Stellenbosch University http://scholar.sun.ac.za

Acknowledgements

First and foremost I would like to thank my supervisor Prof. Heinrich Schwoerer for his never-ending enthusiasm and dedication. Without his guidance and influence I would not be the researcher I am today. Thank you for always having an "open door" policy for discussion and advice. Thank you for encouraging and facilitating my numerous participations in international collaborations and scientific conferences. For your continued involvement in my day-to-day research, but also allowing space for my own scientific creativity, I will be forever grateful.

To my fellow colleagues, past and present. Kerstin Haupt, Günther Kassier, Ilana Boshoff, René Siegmund, Olufemi Olaoye and Andrea von Flotow, thank you for creating a relaxed and enjoyable research environment where productive team work was always encouraged and successfully implemented. I would like to thank especially Kerstin and Günther, the two senior members of the group. Kerstin, for her meticulous and hard working approach, since without her contributions none of our measurements would have been a success or even possible. Günther, for involving me in his often ingeniously simple approaches to perform extremely exciting and novel experiments. For always offering useful advice upon request I also thank both of you. René, a temporary member of our group from Germany, I thank for his contribution to the design of our new streak camera which was instrumental in the streaking electron diffraction experiment.

To the extended "physics family" of the Stellenbosch physics department. Laser Research Institute members, administrative and technical staff. Thank you for support, assistance and the friendly environment you help create at the department which makes it a pleasure to come to work every day.

Lastly I would like to thank Maximilian Eichberger and Prof. Jure Demsar for hosting me during my three month extended visit to the University of Konstanz. My visit and resultant collaboration lead to some extremely fruitful research outputs and was fundamental in the analysis of the measurements done for this thesis. Thank you for your expertise scientific input as well as your hospitality during my stay in Germany.

Stellenbosch University http://scholar.sun.ac.za

Stellenbosch University http://scholar.sun.ac.za

Dedications

Hierdie tesis word opgedra aan

Gillian

&

Oupa Tobie

Stellenbosch University http://scholar.sun.ac.za

Stellenbosch University http://scholar.sun.ac.za

Contents

Stellenbosch University http://scholar.sun.ac.za

Stellenbosch University http://scholar.sun.ac.za

Introduction

Trying to explain macroscopic properties of materials from a microscopic perspective has been the challenge for many physicists, past and present. In the early 20^{th} century the free electron model was one of the first attempts to describe some properties of a material from an atomic viewpoint. In the meantime, several exotic states such as superconductivity and ferromagnetism have also been discovered in various materials. Unfortunately, these unusual states can not be explained by the free electron model where no correlation between the electronic and lattice systems is included. Only models that include correlation suffice, and therefore strong correlation seems to be a decisive property governing these exotic phenomena. A particular class of materials which was discovered in the 1970's undergoes phase transitions above and below room temperature to an unorthodox state where the valence electrons are no longer uniformly distributed but rather modulated into clusters with a periodicity different to that of the lattice periodicity. A modulation with the same periodicity is also induced in the positions of the ion cores of the lattice (see figure 2.8 (c)). This modulated formation of the electrons and ion cores is known as a "charge density wave" (CDW) and was already theoretically predicted by Rudolf Peierls in the 1950's [1] for a one-dimensional metal. After they were discovered, CDW materials were extensively studied and characterised [2, 3] but all investigations were done in thermal equilibrium. At the time, dynamics on the atomic-temporal scale of these CDW's upon perturbation were not accessible since the time scales involved were not resolvable with the available technology.

In the past two decades several technological advancements have resulted in new techniques being developed that now enable the atomic dynamics within CDW materials to be studied on the sub-picosecond time scale. This allows for the investigation of CDW formations in a strong non-equilibrium scenario. By instantaneously disrupting the CDW, with a femtosecond optical pulse for example, and following the evolution of its destruction and/or reformation in real time, valuable insight can be gained behind the principles and physical properties responsible for the CDW in the first place. Initial time-resolvable techniques were however purely spectroscopically based and

Stellenbosch University http://scholar.sun.ac.za

since the core aspect of CDW formation is a structural deformation, a method that can directly view the structure of the material on the picosecond time scale would be highly desirable.

However, to directly observe dynamics in materials on the sub-picosecond timescale, as well as on the atomic level, is by no means trivial. One option is by means of a slightly altered stroboscopic technique used in spectroscopy known as femtosecond pump-probe spectroscopy [4]. The modification on the technique being that the probe source must be able to resolve atomic spatial co-ordinates in some way. Implementing a probe that could generate a diffraction pattern from the crystal structure would for example suffice. A probe which has a wavelength in the order of atomic spacing, i.e. the Ångström regime or 10^{-10} m, will fulfill the diffraction requirement, but the probe also has to have a duration shorter than the dynamics being observed, i.e the sub-picosecond regime or $<10^{-13}$ s. Two candidates for such a probe are femtosecond x-ray pulses and femtosecond electron pulses, both of which can have a wavelength or de Broglie wavelength in the sub-Ångström regime if the x-ray photons have sufficient energy or the electrons are accelerated to a sufficient kinetic energy.

Femtosecond x-ray pulses in the form of K_α photons can be generated by the interaction of intense femtosecond laser pulses with solid state metal targets [5, 6] as well as in the form of synchrotron radiation emitted from sliced picosecond electron bunches passing through an undulator [7, 8]. Generating a photon flux high enough for an actual pump-probe diffraction experiment with these two techniques has been challenging, but there has been success so far [9, 10]. Higher fluxes can be achieved using free electron lasers [11] but these are currently only at extravagant, multi-collaborative facilities with limited user experimental time. Some impressive results especially with biological samples have however been published [12].

On the other hand, sub-relativistic femtosecond electron pulses with a high flux are relatively easy to generate with a standard, commercial, femtosecond laser in combination with a photo-cathode driven electron gun [13, 14, 15, 16] (see also chapter 1). Generating electron pulses with a high electron number (>5000 e/pulse), however, results in severe Coulomb repulsion within the electron bunch yielding a pulse duration of several picoseconds after only a few centimetres of propagation [17, 18] (see also figure 1.8). The easiest solution to overcome this problem is to limit the electron generation-to-sample distance but this is practically limited to around 4 cm which still means the electron number has to be kept below 2000 e/pulse in order to maintain sub-picosecond resolution. Coping with this low electron flux necessitates a sample that can be repeatedly pumped or replaced after each excitation since constant fresh or rejuvenated sample is required for extensive averaging in order to extract diffrac-

Stellenbosch University http://scholar.sun.ac.za

tion signals from the background. Nevertheless, this approach has already resulted in many successful experiments [19, 20, 21, 22]. New approaches to counteract the problem of Coulomb explosion at higher electron number have also been considered. For example: recompressing the expanded pulse by means of several different approaches [23, 24, 25, 26, 27]. This in turn adds several technical difficulties to an already challenging experiment but experiments incorporating compression techniques have also produced promising results so far [28] and seem to be the most hopeful solution for the future. There are three other solutions that have also gained some attention. The first is using a relativistic source where the Coulomb repulsion is suppressed, but unfortunately these high energy electrons have the ability to damage the sample especially if an organic material is investigated. The second approach is implementing a higher repetition-rate, thereby increasing the flux but still maintaining low electron numbers within the individual pulses. Here, the problem could arise that some class of materials do not have enough time to rejuvenate back to its original state before the next pump-probe event. Lastly, an approach that probes the sample with a several picosecond long electron pulse has also been proposed. The different temporal components of the diffracted electron pulse are then spatially separated with a streak camera which has a sub-picosecond resolution [29] (see also section 3.2).

Scattering cross-section is also another consideration that could make an electron probe more favourable to a x-ray probe. X-rays have a scattering cross-section 10^{-6} smaller than that of electrons. This has the consequence that the flux required to generate an equivalent diffraction signal from a thin sample is significantly higher for a x-ray source. Put another way: a bulk sample is required to ensure that enough scattering events occur to generate a diffraction pattern. This might seem only mildly disadvantageous but from the previous discussion it is clear that generating a high flux of coherent x-ray photons is not effortless. Using a bulk sample is also not favourable for two reasons: firstly growing large crystals can be intricate and secondly matching the pump-probe volume of an optical-pump and x-ray-probe source is also not a straightforward exercise. Matching the pump-probe volume is problematic since the optical pulse only has a penetration depth of a few hundred nanometers for most materials while the same material is almost transparent to the x-rays. Performing experiments with x-ray pulses at a grazing incident angle to limit the penetration depth has been one solution but one is still dependant on simulations and estimations to calculate what the actual penetration depth is. Sub-relativistic electrons on the other hand, with their much higher scattering cross section require samples in the order of sub-100 nm thickness to allow for the formation of a usable diffraction pattern. This befittingly matches the penetration depth of the optical pump pulse so it is ensured that all of the

Stellenbosch University http://scholar.sun.ac.za

sample being probed is being pumped. Producing sub-100 nm thick samples can of course be challenging but several techniques do exist (see chapter 1.4).

Ultimately laboratory-based setups, whether it be x-ray or electron based, allow for a more ad-lib experimental approach and in my personal experience this has been the most rewarding as an experimentalist. I therefore believe that considering the various advantages and disadvantages discussed above of an electron probe versus a x-ray probe, Femtosecond Electron Diffraction will become an attractive investigating tool for various structural time-resolved measurements of many research groups in the near future.

In this thesis, the experimental components and technique required to perform a successful Femtosecond Electron Diffraction experiment is covered in the first chapter. In the second chapter the broader concept of strongly correlated materials, and more specifically charge density wave materials, is introduced. The properties of the charge density wave material: $4H_b$-$TaSe_2$, which is the investigated sample in this thesis, is then discussed in greater detail. After briefly motivating why time-resolved measurements are important to gain a deeper understanding of the investigated material, chapter three demonstrates how two ultrafast electron diffraction methods are used to study the structural dynamics of $4H_b$-$TaSe_2$ on the sub-picosecond time scale. The first method used as the primary investigating tool, is the now well-established sub-relativistic Femtosecond Electron Diffraction (FED). The second method, Femtosecond Streaked Electron Diffraction (FSED), is used as an attempt at increasing the signal-to-noise ratio (i.e. increasing the electron flux through the sample) while still maintaining sub-picosecond resolution. The thesis is concluded by discussing the future outlook and further experimental avenues to be considered.

Stellenbosch University http://scholar.sun.ac.za

1. Femtosecond Electron Diffraction

1.1 Basics of Femtosecond Electron Diffraction

Femtosecond Electron Diffraction (FED) is a derivative of the well established research field of Femtosecond Laser Spectroscopy (FLS) [30]. FLS facilitates the study of photo-physical and photo-chemical processes in various physical, biological and chemical molecular systems. The technique utilises femtosecond laser pulses to investigate dynamics in a sample in the sub-picosecond regime by using one laser pulse (pump-pulse) to trigger the dynamics and another pulse (probe-pulse) to observe the evolution of the dynamics. The evolution is for example recorded by measuring the change in absorption of the probe-pulse as a function of delay time between the pump- and the probe-pulse. The relative delay between the two pulses is introduced by having the pump- and probe-pulse travel different optical path lengths and including a mechanical delay stage in one of the arms (see fig 1.1). Sub-picosecond resolution is achievable because the pulses themselves are in the order of 10's of femtoseconds while introducing a 1 μm change in optical path length, which is easily achieved with a mechanical stage, equates to a 3.3 fs relative delay between the pulses. By measuring absorption changes of the probe-pulse the technique of FLS monitors the evolution of electronic state populations as electrons flow from the reactants ground state through transient electronically excited states to the final product state. While this is of course extremely valuable in attaining insight into the inner workings of the system under investigation, it is not directly sensitive to actual structural dynamics. The information obtained from FLS can hint at structural changes upon photo-excitation but a more direct technique would be attractive.

Femtosecond Electron Diffraction offers this attractive insight, where the usual optical prope-pulse is exchanged by a femtosecond electron pulse [14, 31]. The major motivation behind this amendment is that time-resolved structural information can be directly obtained by producing diffraction patterns as the sample undergoes its photo-induced evolution. The time-resolved structural information obtained can give complimentary information to FLS and could assist in understanding and describing macroscopic properties like optical, magnetic, conductivity and chemical properties of the sample under investigation from a microscopic perspective. One limitation however is that because the method relies on the generation of a diffraction pattern, only periodic structures and therefore mainly crystalline solids can be investigated.

Stellenbosch University http://scholar.sun.ac.za

1.2 Experimental Setup

There are six main experimental components required in order to perform a successful FED experiment. These are: (1) a femtosecond laser system which can be commercially obtained with a variety of specifications in pulse duration, pulse energy, repetition rate and central wavelength; (2) a means to generate and accelerate femtosecond electron pulses i.e. an "electron gun"; (3) a vacuum chamber to house the experiment; (4) some electron optics like magnetic lenses to image the diffraction pattern on the detector; (5) a detection system to detect the diffracted electrons and finally; (6) an optical beam splitter and delay stage combination to actualise the "pump-probe" technique. Each of these components will now briefly be discussed but for a more in depth discussion and detail, I refer to my MSc. thesis [13].

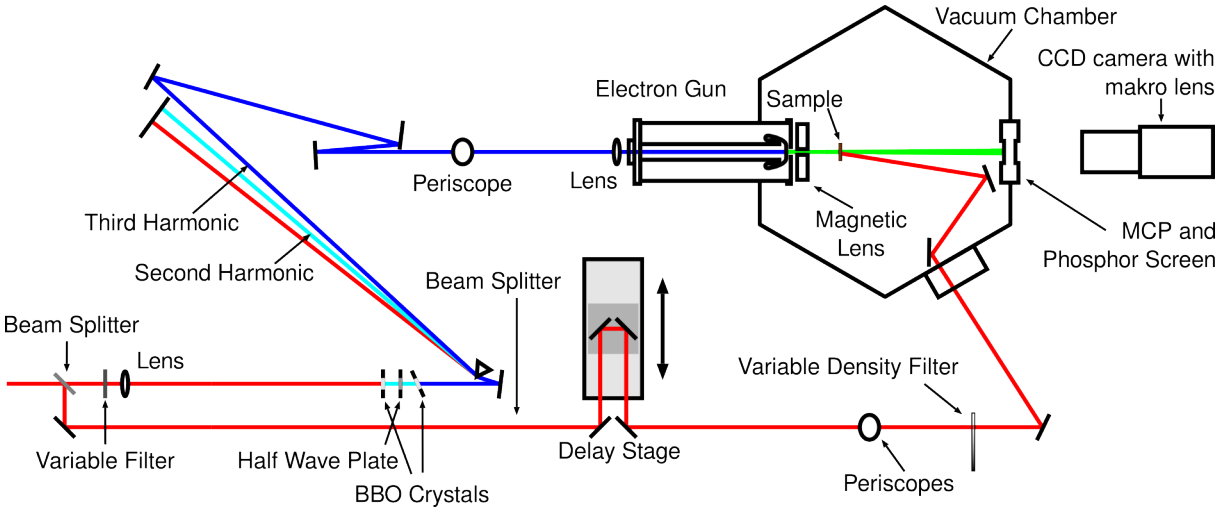

Figure 1.1: The FED setup is headed by a femtosecond laser system delivering 150 fs pulses at a central wavelength of 775 nm and a repetition rate of 1 kHz. A fraction of the pulse is diverted by a beam splitter and frequency tripled (λ = 258 nm, E = 4.8 eV). The resulting UV pulses are focused to a spot diameter of 30 μm on a rear-illuminated, sapphire photocathode coated with 10 nm of gold, on which an ultrashort bunch of photo-electrons is generated . The cathode potential is set to 30 kV and a grounded anode cap with a 2 mm extraction hole placed at a distance of 5 mm from the cathode to ensure rapid acceleration (also see figure 1.2). A magnetic lens is placed 30 mm from the cathode which is used to focus the electron beam through the sample and onto the detector, a micro-channel plate (MCP). The light from the phosphorescent screen behind the MCP is imaged onto a 16-bit, Peltier-cooled CCD camera. The electron gun, sample and MCP are housed within a vacuum chamber and the remainder of the initial pulse is used to pump the sample.

Stellenbosch University http://scholar.sun.ac.za

Femtosecond Laser System

The entire FED experiment is headed by chirp pulse amplified laser (CPA2101) manufactured by ClarkMXR. The Ti:Sapphire regenerative amplifier is pumped by a frequency doubled Nd:YAG laser and seeded by a Erbium-doped fiber ring-laser. The CPA2101 ultimately produces roughly 900 μJ pulses with a duration of 150 fs at a repetition rate of 1 kHz. The central wavelength is 775 nm. The FED setup shares this laser with several other groups in the laboratory and therefore only receives about 250 μJ of the total available pulse energy which is more than sufficient. The laser is a complete 'turn-key' device and almost no alignment on a daily basis is required.

Electron Gun

An ultrashort electron pulse can be generated by utilising the photo-electric effect with a femtosecond laser pulse. A fraction of the main laser beam is diverted by a beam splitter and frequency tripled to $\lambda = 258$ nm. The photon energy of 4.8 eV of the resultant UV pulse is sufficient to generate an ultrashort bunch of photo-electrons [32, 33] on the front surface of a rear-illuminated gold photo-cathode (see figure 1.2). Electrons generated throughout the 10 nm gold layer can move freely through the layer to the surface since electrons in metals have long mean free paths. For gold, the mean free path of a 5 eV electron is around 10 nm [34]. This allows an electron generated at the rear of the gold layer with an energy $E_k = 4.8$ eV ($v = 1.3 \times 10^6$ m/s) to reach the front surface within 10 fs, resulting in an initial pulse duration at the surface similar to the 150 fs UV pulse. The photo-cathode is housed within a stainless steel mount and the electron pulses are accelerated to the desired energy, in this case 30 keV, by placing a -30 kV potential on the mount. A grounded anode cap with a 2 mm extraction hole is placed at a distance of 5 mm from the cathode to ensure acceleration. The cathode, anode cap and high voltage feedthrough are the main components assembled to form the "Electron Gun" (see figure 1.3 and [13]).

It is evident from the description of the electron gun that to generate sub-picosecond electron pulses is rather trivial. However, the generated ultrashort electron pulse is very different to the generating optical pulse in the sense that there is strong interaction among the negatively charged electrons within the pulse. This is unlike the non-interacting photons within the laser pulse. Therefore, even though the electron bunch generated at the photo-cathode has the same duration as the incoming UV pulse, it does not necessarily remain that way. This issue has to be addressed since it is essential to have a sub-picosecond electron pulse at the sample, rather than at the point of

Stellenbosch University http://scholar.sun.ac.za

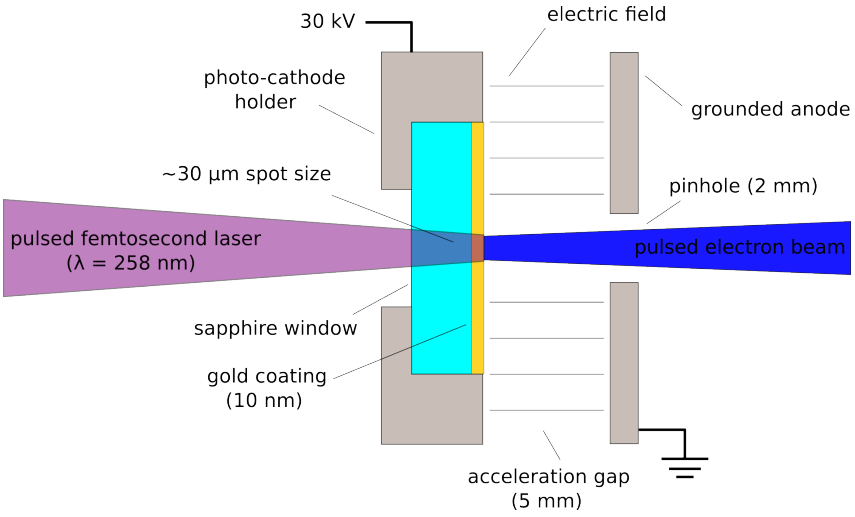

Figure 1.2: Femtosecond electron pulses are generated by illuminating a thin coating of gold deposited onto a UV transparent substrate. The incoming laser pulses must have a photon-energy high enough to overcome the work function of the deposited metal, in this case ~ 5 eV [35, 15]. An electric field is introduced to accelerate the electron pulses to the required energy.

generation, in order to perform a successful FED experiment. There are mainly three factors that can temporally broaden the electron pulse: broadening under acceleration due to the energy spread, broadening due to the energy spread after acceleration, and Coulomb repulsion within the pulse. It has been shown that the broadening due to the energy spread during acceleration can be reduced by increasing the extracting electric field [17]. With an energy spread of 100 meV, which is typical for photo-cathode like ours [15], the broadening can be limited to around 100 fs if an extraction field of 10 MV/m is used [36]. The broadening due to the energy spread in the post-acceleration region has been shown to be negligible with an broadening of roughly 2 fs after 10 cm of propagation of a 30 keV pulse [36]. The Coulomb repulsion is however a major issue. Here it has been shown that a pulse containing 10 000 electrons with an initial pulse duration $\sim$100 fs and beam diameter of 150 μm will already have a pulse duration of over 1 ps after only 10 cm of propagation while a pulse containing 1 000 electrons will have a duration of around 300 fs [17].

Because of the above arguments, there are two parameters that have to be considered in the design of an electron gun in order to ensure sub-picosecond pulses at the sample. Firstly, the acceleration gap has to be kept short in order to generate a strong electric field. This of course comes with the challenges of avoiding electrical breakdown across the gap. An electric field of 10 MV/m is achievable without breakdown occurring if sufficient care is taken into polishing the anode surface and cathode mount (see [13] for more details). The fact that the electron gun is housed in vacuum is also beneficial. The electron gun design used in this setup has an acceleration gap of 5 mm and potential

Stellenbosch University http://scholar.sun.ac.za

of 30 kV and therefore has an extracting field of 6 MV/m which ensures a broadening of $<$ 200 fs in the acceleration region. Secondly, the distance to the sample should be kept to a minimum. With the electron optics in place (i.e. the magnetic lens seen figure 1.4) the distance to the sample can be limited to about 7 cm. All the above parameters are sufficient to generate electron pulses with an electron number of 1000 e/pulse and a duration of $\sim$ 500 fs at the sample (see figure 1.8).

One other consideration when generating electron pulses is the transverse coherence length of the electrons. This has to be (significantly) larger than the crystal constant of the sample in order to generate well defined peaks in the diffraction pattern. Well defined, sharp diffraction peaks will result in a better signal-to-noise ratio. The transverse coherence length is inversely proportional to the transverse emittance at the electron source [36] while the transverse emittance is minimised by limiting the emission region (i.e. UV spot size on the cathode) and keeping the photon-energy close to the work function [33]. Therefore to maximise the transverse coherence length, the UV spot on the cathode should be made as small as possible and the metal coating of the photo-cathode chosen to match the UV photon energy or vice versa. There is however a compromise in the UV spot size since a smaller spot size has two negative impacts. Firstly, it will result in a higher UV intensity and therefore possible ablation of the thin metal coating on the cathode, resulting in a substantial decay in electron number. Secondly, a smaller emission region results in a higher charge density at the source which in turn causes stronger Coulomb repulsion and hence rapid pulse duration broadening. In our setup the UV was focused down to 30 μm and gold, with a reported work function of 4.5 eV [15] which is close to the third harmonic (4.8 eV) of the laser system, was chosen as the photo-cathode material. With these parameters the electron gun generates electron pulses with a measured transverse coherence length of around 10 nm (see section 1.3) which is $\sim$30 times larger than the crystal constant of the investigated sample (see figure 2.6).

How the the pulse duration at the sample as well as the coherence length are experimentally determined is shown in section 1.3.

Vacuum Chamber

The mean free path of an electron in a gas is given by [37]:

$$L = \frac{kT}{4\pi\sqrt{2}r^2p}, \tag{1.1}$$

with k the Boltzmann constant, T the temperature, r the radius of the gas molecules and p the pressure of the gas. The mean free path of an electron at room temperature

Stellenbosch University http://scholar.sun.ac.za

through nitrogen at atmospheric pressure is calculated to be around 400 nm, which means that an electron will not propagate far at atmospheric pressure (nitrogen has a $\sim$2 cm stopping distance for 30 keV electrons [38]). This is a problem for the probing electron pulse if the sample has to placed at least 7 cm from the source (see previous section) and the detector is placed another 20-30 cm downstream. A vacuum system is therefore required which will also aid in avoiding electric breakdown occurring at the high voltages used in the electron acceleration and the micro-channel plate detector. The electron gun, magnetic lens and detection are all housed in vacuum chamber of roughly $50 \times 50 \times 50$ cm in size (see figure 1.3). Vacuum is obtained by means of a rotary-vane rough-pump and a turbo-pump. The vacuum achieved with the system is in the order of 1×10^{-6} mbar which gives a mean free path of 400 m, well above the required propagating distance.

An emergency anti-suckback cut-off valve which closes within 30 ms if there is a power failure and a molecular sieve trap filled with Zeolite are also included to prevent any oil from the rotary-vane pump contaminating the chamber. The chamber is also fitted with several viewing ports, electrical feedthroughs and laser windows to gain access.

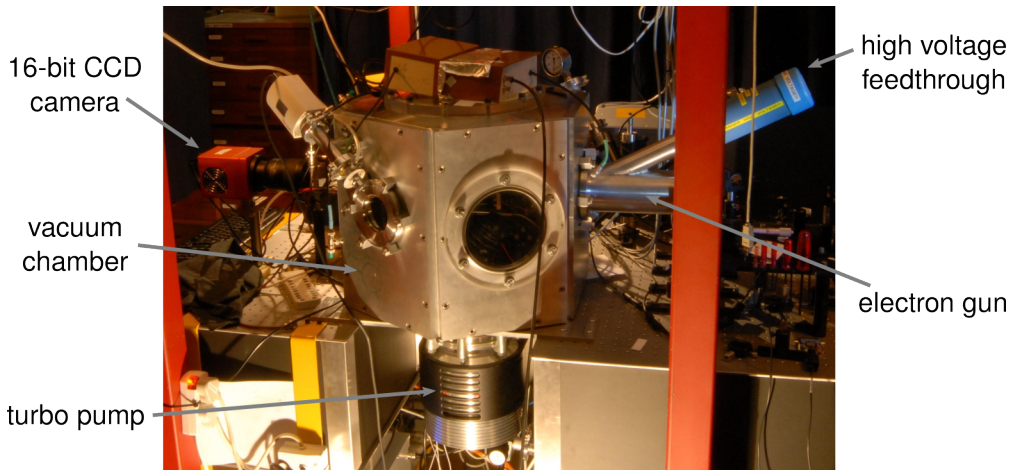

Figure 1.3: The vacuum chamber with 16-bit CCD camera, electron gun and turbo pump visible.

Magnetic Lens

A solenoid magnetic lens is incorporated into the setup to focus the electron beam through the sample and onto the detector. To minimise the distance from the electron source to the sample only one lens is used and it is designed to be as thin as possible (see figure 1.4). The lens is constructed from 585 windings of 0.6 mm thick enameled copper wire encased in a vacuum-compatible epoxy-sealed lens chamber. With a bore

Stellenbosch University http://scholar.sun.ac.za

radius of 7 mm the peak magnetic field was measured to be 125 mT at a typical operating current of 1.25 A. At this current electron pulses with 1000 e/pulse could be focused onto to the detector with the FWHM diameter of the beam around 200 μm at the sample. The calculated thermal power output at this current is around 5-8 Watts and therefore some form of cooling is required. This is done by encapsulating the lens in a aluminium mount which is in turn thermally coupled to the vacuum chamber to ensure passive cooling. This appears to be sufficient and the lens reaches thermal equilibrium at a temperature of around 60 degrees Celsius which is monitored by means of a Pt100 thermal sensor.

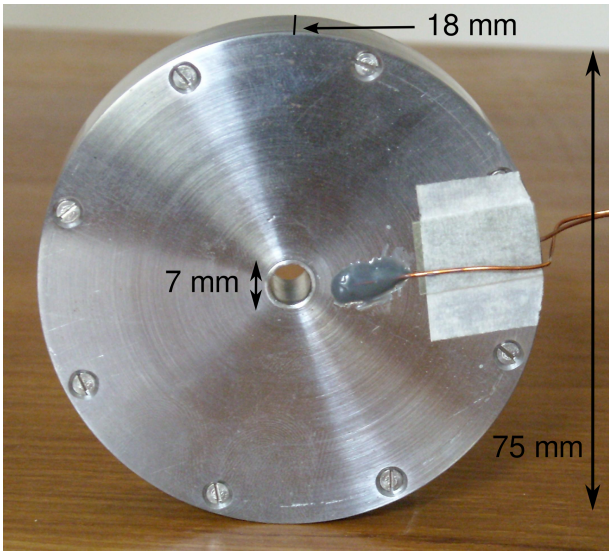

Figure 1.4: Solenoid magnetic lens.

Electron Detection

Electrons are detected by means of micro-channel plate (MCP) coupled to a phosphorescent screen (P43). The photons emitted from the phosphor are imaged by a commercial macro lens (Nikon AF-S Micro 60mm f/2.8) onto a 16-bit CDD chip with a dimension of 2048 $\times$ 2048 px (15 $\times$ 15 mm). The MCP detection surface has diameter of 40 mm (see figure 1.5), consisting of 12 μm capillaries with a 1-2 μm separation (open area ratio: 60%). A double gain (chevron stacked) configuration is employed which gives an amplification of 5×10^6 [39] at a operating voltage of 2000 V (1000 V for each each plate) . The typical operating voltage is in the vicinity of 4500 V (1000 V per plate and 2500 V to accelerate the electrons onto the phosphorescent screen).

Stellenbosch University http://scholar.sun.ac.za

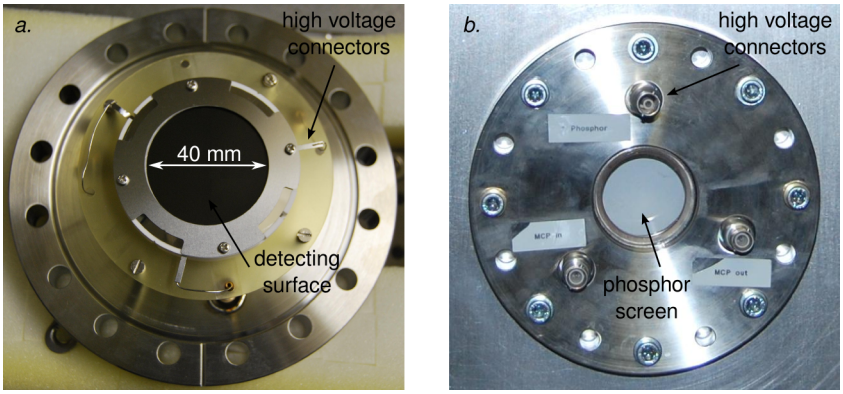

Figure 1.5: Micro-channel plate (MCP) with (a) front electron collecting surface and (b) rear phosphor surface emitting visible photons

1.3 Electron Pulse Characterisation

Two important parameters of the electron pulse that have to be experimentally determined are the pulse duration at the sample and the transverse coherence length of the electrons.

The pulse duration has to be measured since this will ultimately determine the temporal resolution of the experiment. It is also essential that the duration is measured with the appropriate electron number and at the sample position since the duration is highly dependent on electron number and distance the pulse has propagated (see figure 1.8). Because these two parameters and other factors which effect the pulse duration, like UV spot size on the cathode, have the potential to change from one experiment to the other it is also desirable that the method of measuring the pulse duration is easily accessible. In other words, it should be of little disruption to the experiment if the pulse duration has to be quickly measured.

The transverse coherence is important because this will determine which periodic structures within the sample can be monitored. While the coherence length might be large enough do produce a diffraction pattern from the crystal structure itself periodic features like charge density waves (see section 2.2), which can appear or disappear upon photo-excitation, can have periodicities that are larger than the crystal periodicity itself. Since the dynamics of these features contain the desired information for the topic of this study it is essential that the coherence of the electron beam is appropriately large enough. The transverse coherence length however does not have to be measured on a day-to-day timescale as this is mainly affected by the emission region (the UV spot size on the cathode) which does not change on its own accord but only when purposefully adjusted by the user. Therefore the coherence only needs to measured once to verify that it is good enough for the sample under investigation. If required, the

Stellenbosch University http://scholar.sun.ac.za

coherence can also quickly be optimized before each experiment by adjusting the UV lens position and monitoring the the sharpness of the diffraction pattern.

Pulse Duration

The most common method currently implemented to measure femtosecond electron pulses is based on the scattering of electrons by an intercepting femtosecond laser pulse. The method is analogous to an auto- or cross-correlator [40, 41] implemented routinely in femtosecond spectroscopy to measure femtosecond laser pulses. The essence of an all optical correlator technique is that the duration of an ultrashort laser pulse is measured via non-linear interaction with another femtosecond laser pulse, which can either be a duplicate of itself (auto) or another pulse entirely (cross). As in the pump-probe method, explained in the beginning of this chapter, the delay between the pulses can be varied with femtosecond resolution using mechanical delay stages, and the magnitude of the interaction measured as a function of the relative delay. For example: the interaction can take the form of frequency mixing between the two pulses in a non-linear crystal where the energy of a photon from one pulse is added to the energy of a photon from the other pulse resulting in a single higher energetic photon (known as sum-frequency mixing). Plotting the intensity of the resultant light from the frequency mixing process, as a function of delay between the two pulses will yield the convolution of the two pulse durations. If the pulses are copies of each other and therefore have the same duration the individual pulse duration is then simply the convoluted duration.

In a similar fashion the duration of a femtosecond electron pulse can be measured via interaction with a femtosecond laser pulse. Here the interaction takes the form of scattering of the electrons by the ponderomotive potential of the laser pulse [42, 43]. The magnitude of the scattering as a function of delay time between the two pulses can be used to calculate the electron pulse duration. More recently this technique has been improved by using two counter-propagating laser pulses to form a standing wave and thereby increasing the ponderomotive potential by orders of magnitude [44, 26]. While this method is relatively simple to implement there are some limitations. While the pulse duration is easily determined the temporal structure of the pulse is not retrieved because this is smeared out by the scattering process. Determining the temporal structure is not always necessarily required but could be of interest in some cases. Having the setup mobile to measure the pulse duration at different positions or moving the setup into the beam path to quickly measure the pulse duration without major disruption to the experiment can also be a challenge.

Stellenbosch University http://scholar.sun.ac.za

Over the past three years, our group has developed an alternative method do determine the pulse duration of sub-picosecond electron pulses. The technique is based on the concept of a streak camera [45] but now with an improved temporal resolution of 150 fs [18]. The idea is that the pulse duration is measured by interacting the electron pulse with a rapidly changing electric field. Electrons at the temporal front of the pulse are deflected into a different direction to those at the rear of the pulse. The sweep in deflection creates a streak on the detector (see figure 1.8 (b)). The pulse duration is determined by measuring the length of the streak and the streaking velocity. The biggest obstacles with measuring femtosecond electron pulses with this technique is generating a sweep in electric field that is fast enough as well as intense enough, in other words a large enough temporal field gradient: $\frac{dE}{dt}$. The large sweeping speed is required to ensure that electrons at different temporal positions experience a different electric field and the strength is required to impose a large enough deflection in order to generate a streak on the detector longer than the width of the unstreaked beam on the detector. The second obstacle is synchronising the timing of the sweep with the arrival of the electron pulse. Another key factor is that the interaction length of the electron pulse with the electric field has to be short enough such that the duration of the electron pulse does not significantly change while it is being streaked. This is because, as discussed previously and seen in figure 1.8 (a), the electron pulse duration can change dramatically over only a few centimeters of propagation, especially for highly charged bunches. Therefore the interaction length has to be kept to the millimeter regime.

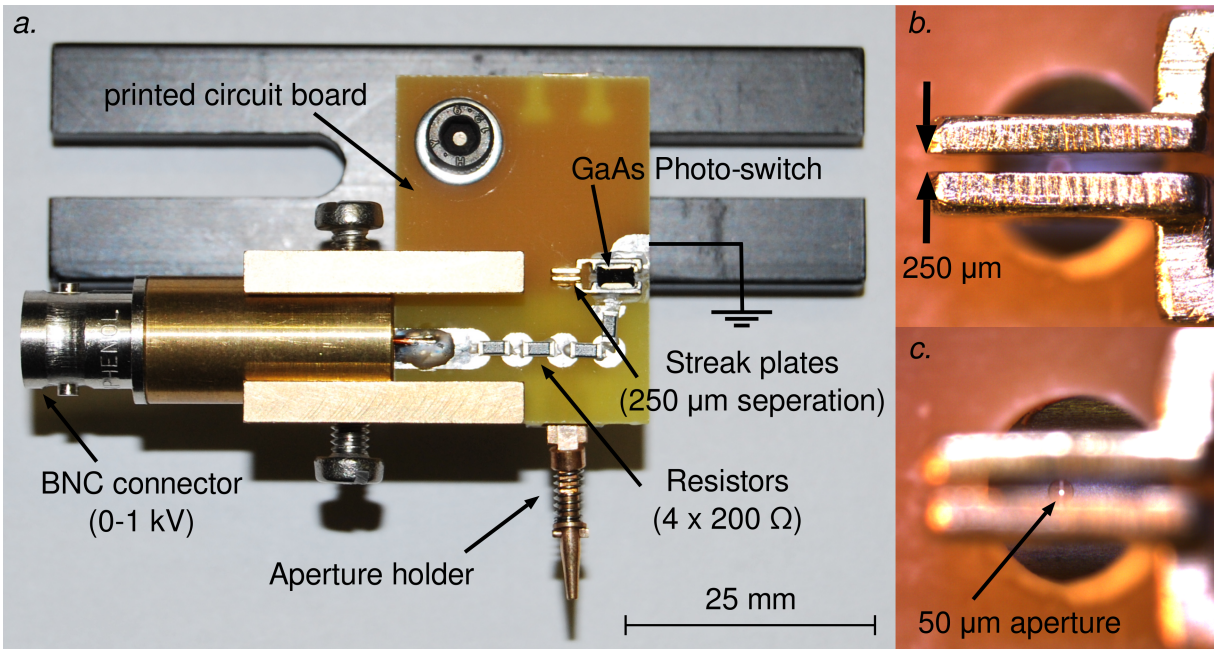

Figure 1.6: (a) Streak camera with (b) enlarged view of streak plates in focus and (c) 50 μm aperture in focus.

Stellenbosch University http://scholar.sun.ac.za

To generate an electric field to fulfill the requirements discussed above the following is done: Two streaking plates of size 4×4 mm are separated by a gap of 250 μm and electrically connected to one another by means a of Gallium-Arsenide (GaAs) photo-switch of size 6×3 mm (see figure 1.6). A potential of ~ 1 kV is placed across the plates by means of a HV pulser (20 ns) triggered at the same repetition-rate as the laser/-electron pulses. The voltage is pulsed to hinder surface tracking across the photo-switch and the 20 ns is much longer than the electron propagation time of ~ 40 ps between the streaking plates, therefore effectively seen by the electrons as a constant voltage. Acting as a RLC circuit the electric field between the plates starts oscillating with measured frequency of 6 GHz after a 50 μJ laser pulse is used to illuminate the GaAs photo-switch. The electrons pass through a 50 μm aperture, pass between the streak plates and the oscillation of the electric field is mapped out by measuring the deflection of the electrons as function of the photo-switch's trigger pulse delay (see figure 1.7). From this the streaking velocity is calculated in pixels/ps and converted to mm/ps by calibrating (pixels-to-mm) the imaging system from the MCP onto the CCD camera. The linear streak velocity is finally converted to an angular streak velocity given in mrad/ps by measuring the distance from the streak camera to the MCP detector. When measuring the electron pulse duration, the trigger-pulse delay for the photo-switch is adjusted such that center of the electron pulse arrives at $E = 0$ (zero deflection) to limit the effect of jitter (see middle image of figure 1.7 (b)).

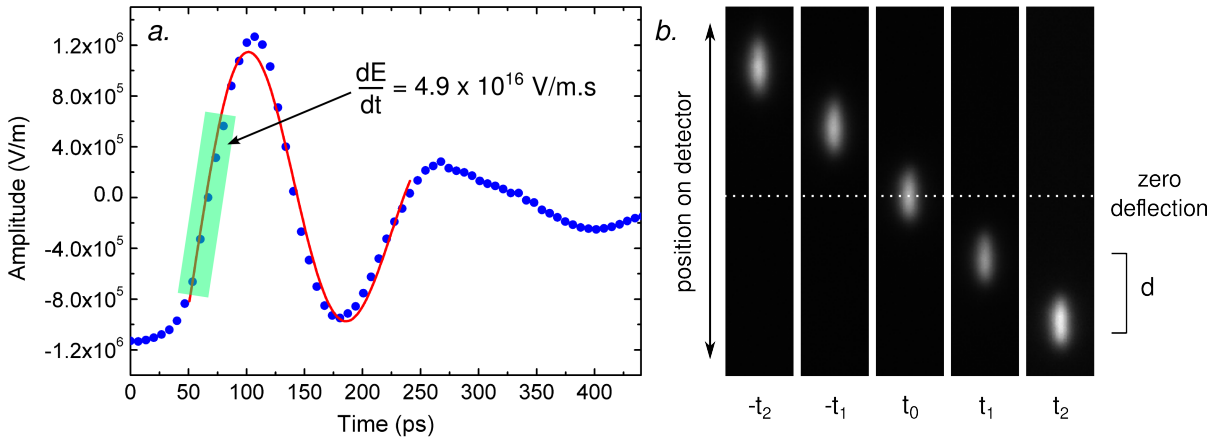

Figure 1.7: Plotted in panel (a) is the electron beam deflection as a function of laser trigger time. Red curve indicates a damped sinusoidal fit with a frequency of 6 GHz. Panel (b) shows the deflection of the five highlighted data points in panel (a). $\frac{dE}{dt} = 4.9 \times 10^{16}$ V/m.s is calculated by determining the electric field required to deflect a 30 keV electron by a distance d on the detector with a temporal trigger delay of dt $= t_2 - t_1$. The streak velocity is also calculated from the magnitude of the deflection and the step size of the trigger delay.

The resolution of the streak camera is given by the ratio of the unstreaked beam's

Stellenbosch University http://scholar.sun.ac.za

angular spread ϕ and the angular streak velocity ω_s:

$$\Delta\tau_s = \frac{\phi}{\omega_s}. \tag{1.2}$$

For the measurement shown if figure 1.8, the angular beam spread of the unstreaked electron beam was measured as 0.5 mrad which is typical for an electron gun setup like ours. An angular streak velocity of 2.2 mrad/ps was measured at an operating voltage of 600 V. Using equation 1.2 a temporal resolution of 230 fs is calculated. It has however been demonstrated that with a operating voltage of >1000 V a resolution of 150 fs is achievable [18]. There is however added risk of damaging the photo-switch at higher voltages and is the reason for operating the streak camera at the lower 600 V.

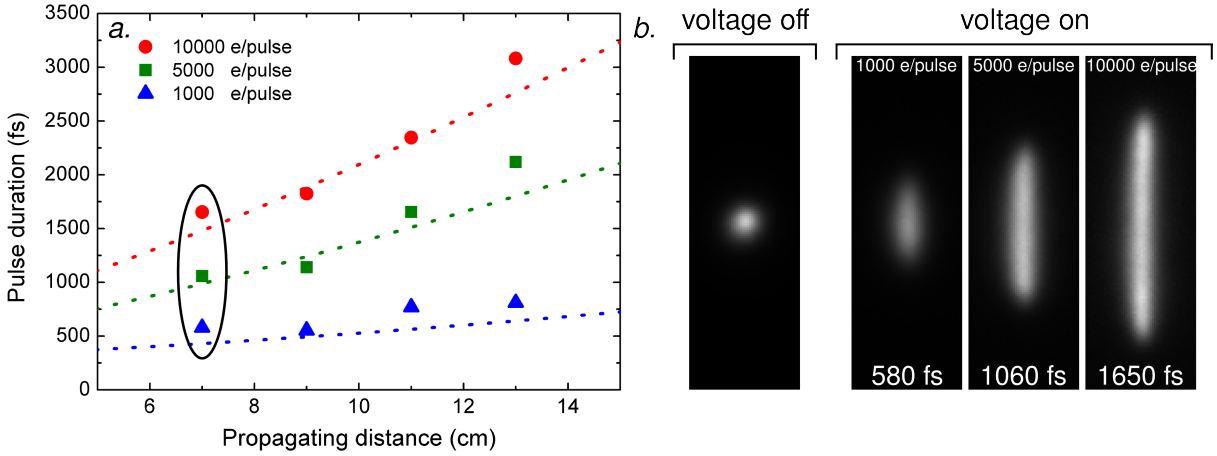

Figure 1.8: Plotted in panel (a) is the electron pulse duration as a function of propagating distance for electron pulses containing 1000, 5000 and 10000 electrons. The ASTRA simulated pulse durations for the corresponding electron numbers are also plotted as dotted lines. Panel (b) shows the unstreaked electron beam and streaked pulses for for pulses circled in panel (a). Here it is clear the increasing the electron number has a drastic effect on the pulse duration at a typical sample position of 7 cm from the cathode.

Coherence Length

The transverse coherence of the electron beam can be determined as follow: generate a diffraction pattern; measure the distance between two diffraction spots; measure the FWHM of the spots themselves. The ratio of these two values will give the number of scattering planes and multiplying this with the crystal constant of the relevant crystal planes will give the transverse coherence length of the electron beam. The reason for this can be explained by considering the intensity distribution of a multiple slit diffraction pattern. In optics the intensity distribution from a multiple slit grating illuminated

Stellenbosch University http://scholar.sun.ac.za

by a monochromatic plane wave is given by [46, 47]:

$$I(\theta) \sim \frac{\sin^2\left(\frac{\pi}{\lambda}a\sin\theta\right)}{\left(\frac{\pi}{\lambda}a\sin\theta\right)^2} \times \frac{\sin^2\left(\frac{N\pi}{\lambda}b\sin\theta\right)}{\sin^2\left(\frac{\pi}{\lambda}b\sin\theta\right)}, \tag{1.3}$$

where a is the width of the slits, b the center-to-center spacing of the slits, λ the wavelength of the light, θ the angle of observation and N the number of slits. Plotted in figure 1.9 is the normalised intensity distribution obtained from equation 1.3 for $N = 2, 4$ and 6. It is evident that increasing N does not change the position of the main maxima but only decreases the width of the peaks as well as increasing the minima between the main peaks. The number of minima is given by $N - 1$. It can also be noted that the ratio of the distance between the main maxima x and the the FWHM of the maxima Δx is equal to N, such that:

$$N = \frac{x}{\Delta x}. \tag{1.4}$$

For example, in figure 1.9 for $N = 2$ the distance between the peaks is 1 while the FWHM of the main peak is 0.5.

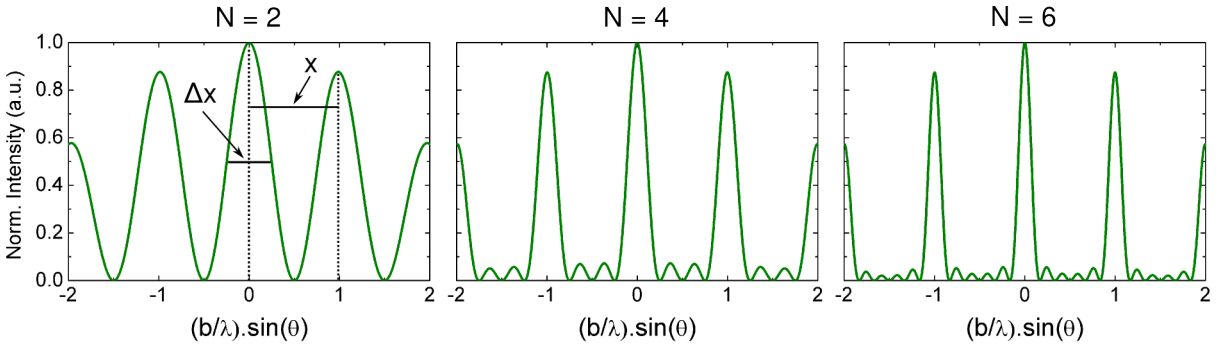

Figure 1.9: The normalised intensity distribution from a multiple slit grating with the number of slits, $N = 2$, 4 and 6. The distance between the main peaks are indicated by x with the FWHM of the peaks given as Δx. The number of slits is given by the ratio such that: $N = \frac{x}{\Delta x}$.

In a similar fashion the number of slits, or number of scattering planes in this case, can be calculated for a given crystal sample when generating a diffraction pattern with the electron beam. Once the number of scattering planes is known the transverse coherence length can be determined by multiplying this number with the distance between the planes i.e. the crystal constant for that specific crystal axis. In figure 1.10 the diffraction pattern from two crystal samples are shown: (a) for $4H_b$-$TaSe_2$ and (b) for an organic crystal, Cu(dicyanoquinonediimine)$_2$ or Cu(DCNQI)$_2$. The intensity profiles along the lines indicated on the diffraction pattern are also plotted. From these profiles the separation as well as the FWHM of the peaks is determined and the number of scattering planes (N) for each sample calculated using equation 1.4 (see figure

Stellenbosch University http://scholar.sun.ac.za

1.10). The crystal constants for the relevant crystal axes of $4H_b$-$TaSe_2$ is $a = b = 3.46$ Å and $c = 3.9$ Å for $Cu(DCNQI)_2$. The transverse coherence of the electron beam is calculated to be 9.2 nm and 7.7 nm respectively for the two samples, so it can be concluded that the transverse coherence length of the beam is in the order of 10 nm. This is of course only a lower limit for the coherence length and it could be larger since the diffraction peaks can also be broadened due to properties of the sample itself.

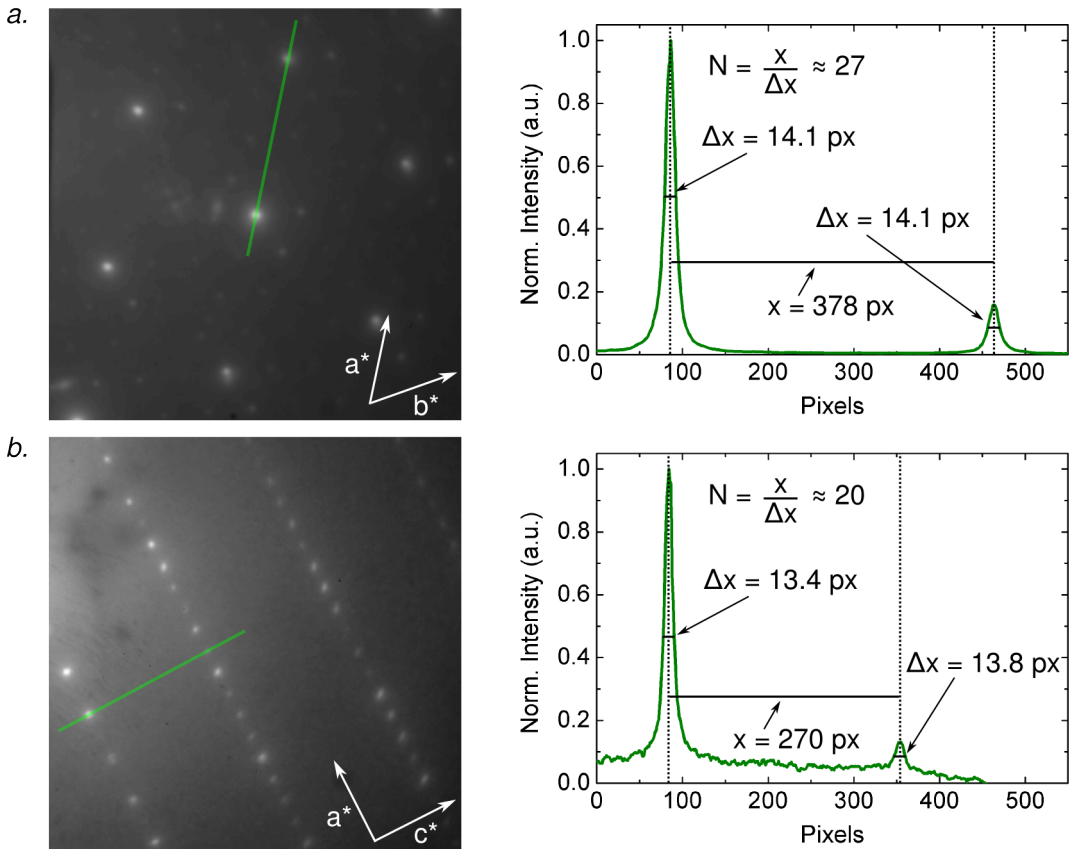

Figure 1.10: Shown are diffraction patterns of (a) $4H_b$-$TaSe_2$ and (b) $Cu(DCNQI)_2$. The profiles adjacent to the images are along the lines indicated on the diffraction pattern. The number of scattering planes, N is calculated from the ratio of the peak separation and the peak width. The transverse coherence length can then be calculated by multiplying this with the crystal constant of the relevant crystal axis. From the $4H_b$-$TaSe_2$ diffraction pattern which has a crystal constant $a = 3.46$ Å the transverse coherence is calculated to be 9.2 nm and 7.7 nm from the $Cu(DCNQI)_2$ diffraction pattern which has a crystal constant $c = 3.9$ Å.

As discussed previously the transverse coherence length is determined by the electron source size (i.e. the UV spot size on the cathode) and the excess kinetic energy of the electrons at generation. The position of the lens ($f = 300$ mm) that is used to focus the UV light on the photo-cathode (see figure 1.1) can be varied to change the electron source size. To illustrate the effect of the source size on the transverse coherence length of the electron beam, a diffraction peak from a $4H_b$-$TaSe_2$ sample is shown if figure

Stellenbosch University http://scholar.sun.ac.za

1.11 (a) as a function of the lens position. The transverse coherence for each of these positions is calculated as discussed before and plotted in 1.11 (c) and it is clear that a maximum coherence is achieved when the photo-cathode is situated at the focus of the lens (see 1.11 (b)). The signal from the charge-density-wave (the six peaks surrounding the Bragg spot) which has a larger periodicity than the crystal structure (see section 2.3) also becomes more pronounced as the coherence length increases, as one would expect.

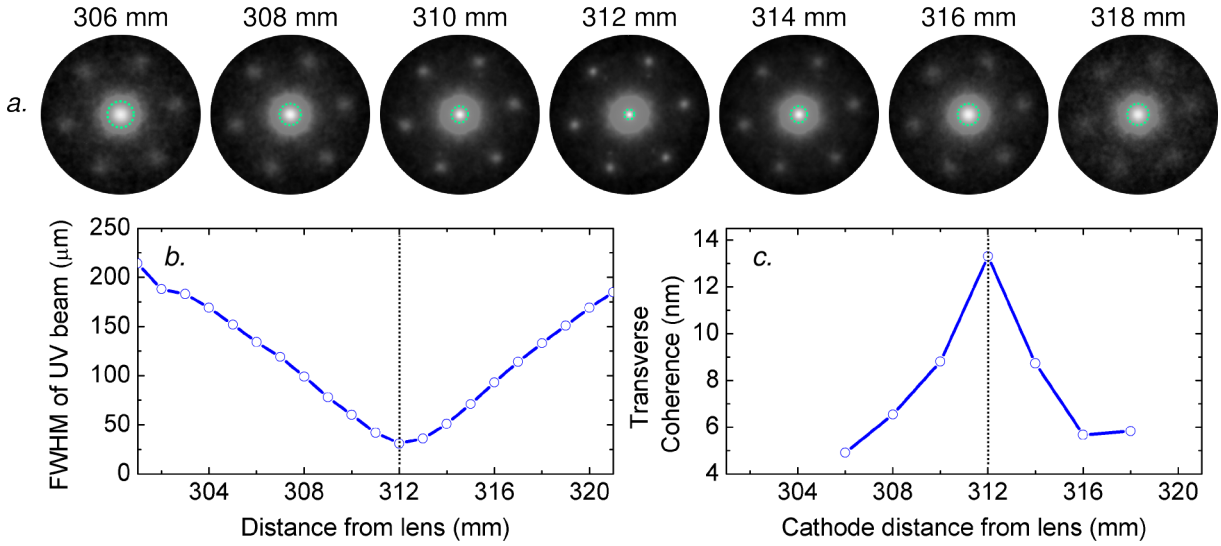

Figure 1.11: (a) A diffraction peak from a $4H_b$-$TaSe_2$ sample as a function of the UV lens position. The FWHM of the peak, indicated by a dashed circle to guide the eye, reaches minimum when the photo-cathode is situated at the focus of the lens. (b) The size of the UV beam on the photo-cathode as a function of the distance from the lens to the cathode. (c) The transverse coherence plotted as a function of the lens position and it is clear that a maximum coherence is achieved when the photo-cathode is situated at the focus of the lens.

1.4 Sample Preparation

The final and often most challenging task to be mastered in order to perform a successful FED experiment is preparing samples into a suitable format. Samples have to be electron transparent but still possess enough material for sufficient scattering events in order to generate a diffraction pattern. For most solid state samples and for an electron energy around 50 keV this is a sample thickness in the order of 10-100 nm. If the sample can not be repeatedly pumped, either because it is destroyed upon photo-excitation or does not recover to its original state within the period of the repetition-rate of the laser (e.g. 1 ms for a 1kHz laser system), then not only are thin samples required but also a large quantity of it. Each sample also has to have the same crystal orientation if a single crystalline sample is investigated. The large quantity is required because to generate

Stellenbosch University http://scholar.sun.ac.za

a reasonably "good" diffraction pattern from a $\sim$ 50 nm thick sample about $10^5 - 10^6$ electrons are needed. Since the electron number per pulse has to be kept to $10^3 - 10^4$ electrons per pulse to ensure sub-picosecond pulses (see section 1.3) the sample has to be probed (and pumped) 10-100 times in accumulation mode for a single diffraction pattern and this is only for a single pump-probe time-delay. Diffraction patterns at several time delays are required for a transient signal and so it is clear that preparing enough of a sample that cannot be repeatedly pumped is a major hurdle for a successful experiment. This is why it is highly desirable and sometimes even essential to have a sample that can be repeatedly pumped without having to be replaced with a fresh sample after each excitation pump. Even if a sample that allows for multiple pumping is identified as an interesting candidate for a FED experiment, it can still be challenging to produce thin samples. There are however several methods available which will now be discussed.

One method is to thermally evaporate or sputter the desired sample onto a substrate that is then dissolved in a liquid that does not dissolve the sample itself, for instance water. There are two approaches to this method, either the whole substrate can be dissolved [14] or a thin soluble layer of material can be deposited between a non-soluble substrate (glass) and the sample (figure 1.12 (a) is an example of the latter). The substrate is slowly lowered into the chosen liquid (again, mostly water) and the whole substrate or the soluble sandwiched layer is dissolved. The sample is floated off onto the surface of the liquid aided by the surface tension and can then be lifted from the surface and transferred onto a TEM mesh (see figure 1.12 (b)). This method was mostly employed for first-generation FED experiments where the non-thermal melting [19, 48, 49] or phonon oscillations [16] in metals like aluminium, gold, copper and bismuth were investigated.

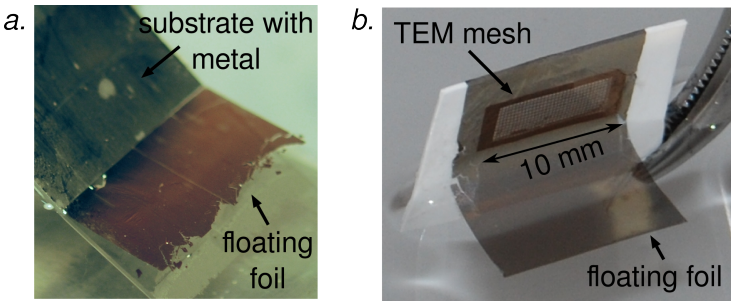

Figure 1.12: Image (a) shows a 50 nm thin gold layer deposited onto a glass substrate, with a water-soluble layer deposited between the substrate and the gold, being lowered into water. A large section of the gold foil has already parted with the substrate and is floating on the surface of the water. Image (b) shows how the foil can be transferred to a TEM mesh by slowly raising the mesh from underneath.

Stellenbosch University http://scholar.sun.ac.za

The "floating foil" method is however no longer sufficient as samples are becoming more complex. Generating thin films on substrates of complex inorganic or organic crystalline samples can be difficult or even sometimes impossible and an alternative method is required. A standard method used for sample preparation for conventional TEM measurements known as ultra-microtoming [50] has of late been the preferred method [20, 51, 52]. In this method a diamond knife is used to slice extremely thin layers from a bulk sample and was also the method used to produce the 4*Hb*-$TaSe_2$ investigated for this thesis. The method entails embedding the bulk sample in resin for support and mounting it onto the front of the microtome arm. The arm can be mechanically oscillated up and down while moving forward in sub-100 nm steps between each oscillation. The diamond knife is positioned in front to of the arm such that with each oscillation a thin slither of the sample is sliced and floated onto the surface of a liquid reservoir attached to the knife (see figure 1.13 (a)). The reservoir can be filled with any liquid that does not dissolve the sample or the glue that attaches the diamond knife to the reservoir. The floating samples can then be transferred onto a TEM mesh using the same method as before (see figure 1.13 (b)).

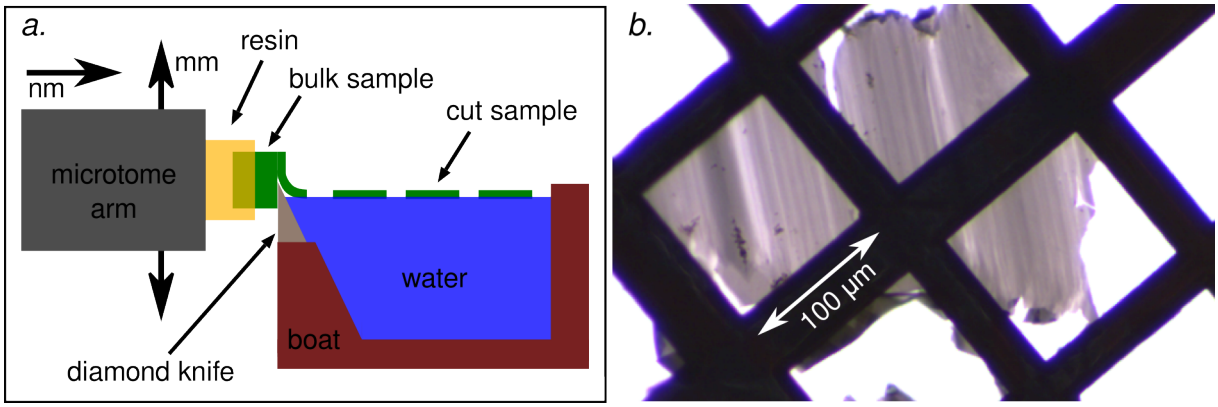

Figure 1.13: (a) Principle of ultra-microtoming: the bulk sample, inbedded in resin for support, is cut into thin slices as the microtome arm moves up and down while also moving forward the desired thickness which can be sub-100 nm. The sample is cut with a diamond-knife and guided onto the surface of a small water resovoir. The floating samples can then be transferred onto a TEM mesh. (b) A 100 nm thick microtomed 4*Hb*-$TaSe_2$ sample mounted on a TEM mesh.

A final method, namely Focused Ion Beam (FIB) milling [53, 54] could pave the way for future FED sample preparation. This method has the advantage that it can produce high quality electron transparent samples from fragile and ultra-fine specimens. Since the samples being investigated by FED are increasing in complexity this method could be a solution for preparing samples for future experiments. In this method a beam of Ga+ ions is used to mill a slab of sample from a bulk crystal. The initial slab can have an area of several 100 μm and a thickness of a few micrometers (see fig 1.14 (a) and (d)).

Stellenbosch University http://scholar.sun.ac.za

A precursor gas can be injected into the vacuum chamber and the same ion beam used to selectively deposit a metal (in this case platinum) where the beam is directed. This technique can be used to ”weld“ an extraction needle onto the slab and lift it out of the bulk sample and move it onto a TEM grid (see fig 1.14 (a)-(d))[1]. Once positioned using the attached needle the sample can be ”spot welded“ and secured onto the TEM grid in the same way the needle was attached. The ion beam can then be used to detach the needle and a free standing slab is left behind. Polishing the sample surface down with the ion beam at a glancing angle to a few nanometers is then the final step (see fig 1.14 (f)). While this technique is extremely precise and well controlled it is rather time consuming and expensive so not ideal for samples that can only be pumped once.

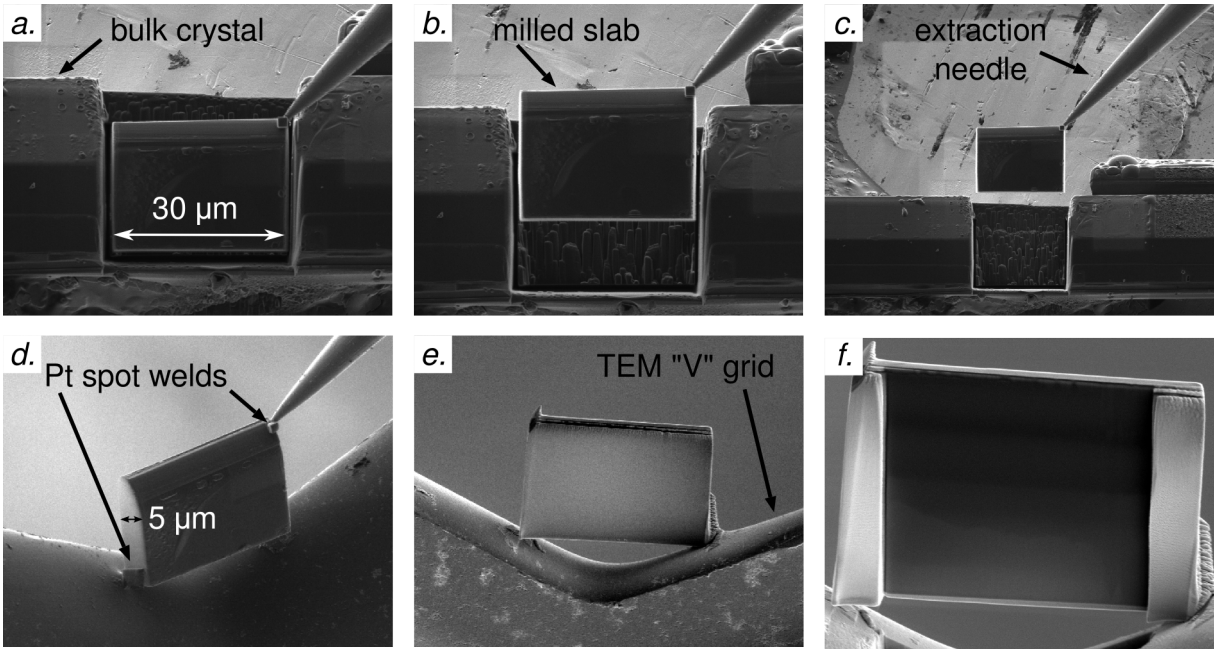

Figure 1.14: Focused Ion Beam (FIB) milling procedure: panel (a) shows a 20×30 μm slab of $Cu(DCNQI)_2$ milled from a bulk crystal. Panel (a) - (d) shows how an extraction needle can be ”welded“ onto the slab and lifted from the bulk sample. Once secured onto a TEM grid, (d) and (e), the final step is to use the ion beam at a glancing angle to polish the sample surface down to a few nanometers as seen in panel (f).

[1]Images courtesy of Florian Hüwe and Prof. Martin Kamp from the University of Würzburg

Stellenbosch University http://scholar.sun.ac.za

2. Strongly Correlated Materials

2.1 Introduction to Correlated Materials

The free electron model or Drude-model for solids, developed by Paul Drude in 1900, proposes the idea of describing a metal as having the positive ion-cores of the metal stacked in a lattice while a "sea" of valence electrons are free to flow like an "electron gas" between the cores. Electron-electron interaction is completely neglected and the only interaction these valence electrons have with the lattice is possible scattering during a collision, in other words there is no correlation between the dynamics of the lattice and the free electrons. Although simple, this model is able to explain many phenomena observed in metals like electronic and thermal conductivity, thermionic emission as well as magnetic susceptibility [55, 56]. It does however have its limitations and in particular can not explain why some materials are insulators and others are conductors or semi-conductors. In 1928 Arnold Sommerfeld modified the model and included the notion that the ion-cores generate a periodic lattice of potential wells that the free electron experiences, in other words there is some sort of correlation between the lattice and the free electrons. The introduction of the periodically occurring potential wells results in the overlap of identical (degenerate) electron wave functions at the edge of the Brillouin zones which leads to a lifting of the degeneracy and the occurrence of bands and band gaps . The concept of electronic energy bands and band gaps within a material is hence included (see figure 2.1). Known as the nearly free electron or Drude-Sommerfeld model, it could explain the difference between an insulator, conductor and semi-conductor using the Fermi-level and electronic band structure of the material.

Other classes of materials that display newly discovered exotic states can also only be explained by including strong correlation between the free electrons and the lattice. For instance, iron and nickel become ferromagnetic below temperatures of several hundred degrees while lead and aluminium become superconductors at cryogenic temperatures. Materials known as charge density wave (CDW) conductors have also been discovered. They have remarkable non-linear and anisotropic electrical properties, gigantic dielectric constants, unusual elastic properties and rich dynamical behaviour. The unorthodox properties of CDW materials arise from a phase transition into a state with a periodic modulation of the conduction electron density that is accompanied by a modulation of the positions of the ion cores in the lattice [57]. One such material is

Stellenbosch University http://scholar.sun.ac.za

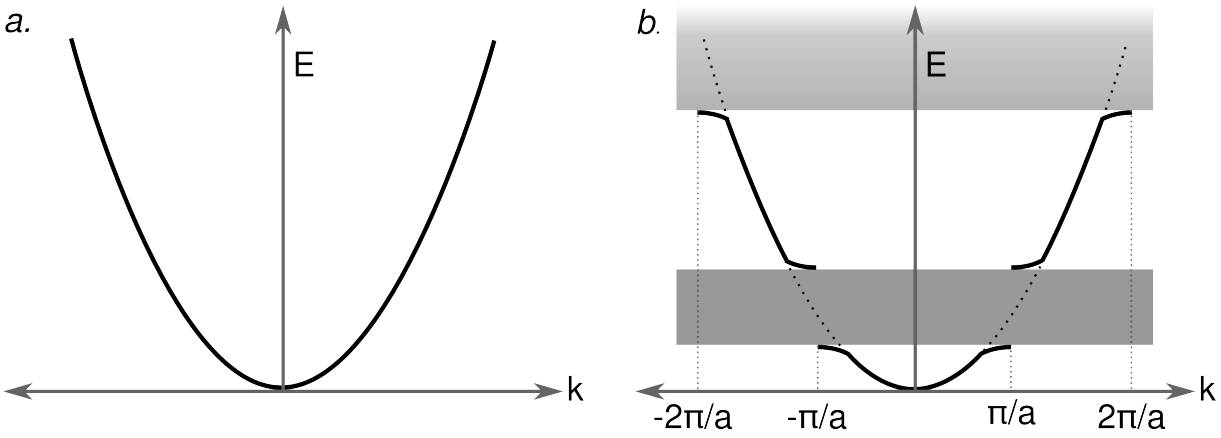

Figure 2.1: (a) Plotted is the energy as a function of wavevector for a free electron. Panel (b) shows the effect of including the periodic lattice of potential wells of the ion cores as in the Drude-Sommerfeld model. A degeneracy of electron energy at the intersection of adjacent wells where $k = \pm\frac{n\pi}{a}$ (with a the lattice constant and $n = 1, 2, 3...$) causes the splitting of the energy and hence lowering and raising of the electron energy at wavevectors corresponding to multiples $\pm\frac{\pi}{a}$. This in turn results in the formation of band gaps such that there are forbidden (shaded areas) and allowed bands. Using the Fermi-level and electronic band structure of the material the difference between an insulator, conductor and semi-conductor can be explained.

the topic of investigation for this thesis and therefore, to start off, the principles behind the formation of CDW's will be discussed in the following section.

2.2 Charge Density Wave Materials and Transition-metal Dichalcogenides

Charge density wave (CDW) materials are materials that have a stable state where the electron density has a modulation different to that of the lattice. This charge modulation induces a slight modulation of the lattice atoms positions with the same periodicity which is also referred to as a periodic lattice distortion (PLD). The two modulations together constitute what is know as the CDW (see figure 2.2 (b)).

If the periodicity of the CDW is a rational fraction or multiple of the lattice periodicity it is know as a commensurate CDW (C-CDW) otherwise it is called an incommensurate CDW (I-CDW). The formation of a CDW was first theoretically described and predicted by Rudolf Peierls [1] in the 1950's and is therefore also know as a Peierls instability or Peierls transition [58]. In the same way the native lattice periodicity is responsible for band gap generation as explained by the Drude-Sommerfeld model (see figure 2.1), the new superimposed periodicity of the CDW also generates band gaps. However, the CDW and the resultant band gap will only be favourable if in the process

Stellenbosch University http://scholar.sun.ac.za

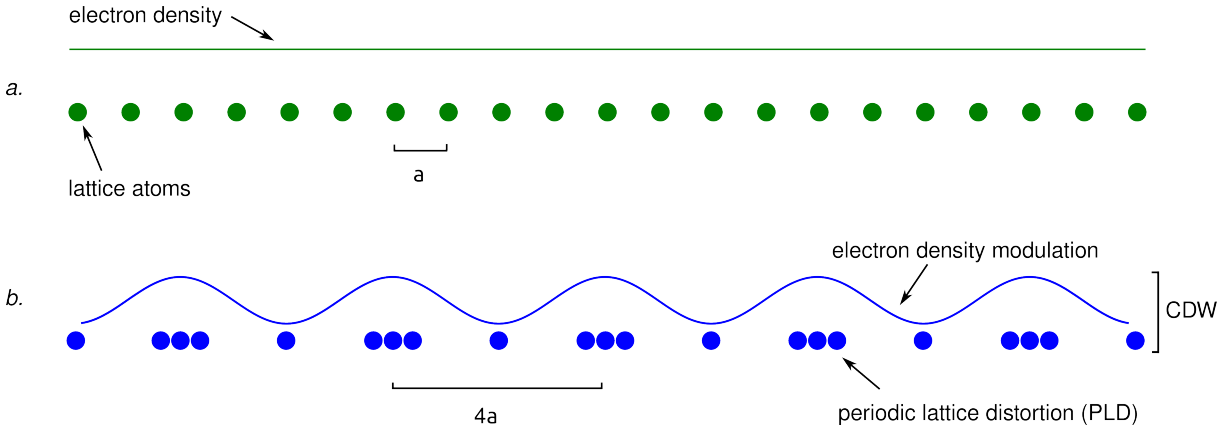

Figure 2.2: Panel (a) shows the position of the atoms in the lattice with a uniform electron density while panel (b) illustrates the formation of a charge density wave (CDW) where there is a modulation of the electron density. The modulation in the electron density induces a slight modulation in the position of the atoms also referred to as periodic lattice displacement (PLD). The magnitude of the PLD is highly exaggerated in the sketch for clarity and the actual displacement is only a few percent of the lattice constant. The two modulations together constitute what is know as the CDW.

there is net loss in electronic energy. For there to be a lowering of total electron energy, due to the band gap formation, the gap has to develop at the Fermi surface such that the energy of the occupied states is lowered and the energy of unoccupied states is raised (see figure 2.3). Since the gap occurs at the the Fermi surface, the wave vector of the CDW that produces the gap has to be $q_{\mathrm{CDW}} = 2k_F$ (see figure 2.3).

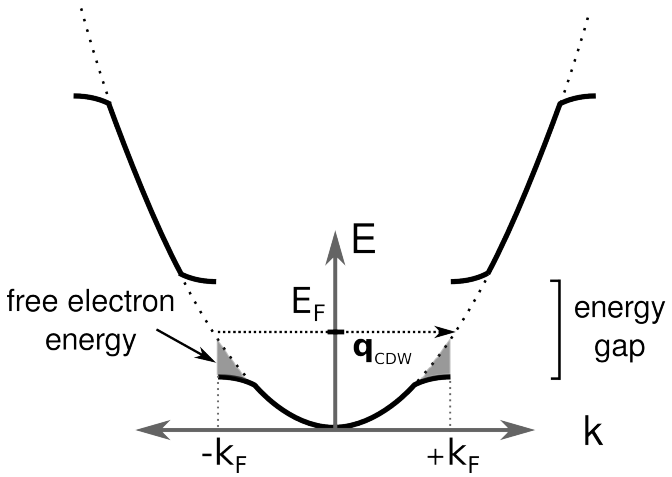

Figure 2.3: The new periodicity of the the CDW ($q_{\mathrm{CDW}} = 2k_F$), results in a gap formation at $k = \pm k_F$. A lowering of the energy of the electrons below the gap causes the CDW to be favourable and stable if the free electron energy is more than the elastic energy required to modulate the lattice.

The question is now: why does a CDW not form in all metals? To modulate the lattice requires energy, so the CDW will only be favourable and stable in a metal where the

Stellenbosch University http://scholar.sun.ac.za

free electron energy due to the lowering of occupied states (see shaded areas in figure 2.3) is more than the elastic energy required to modulate the lattice in the first place. The energy required to modulate the lattice is dependent on the lattice rigidity and is therefore element specific. Peierls also added that CDW formation will be favourable in one-dimensional metals (i.e. a metal which is only conductive along a single crystal axis), where the Fermi-surface is represented by two parallel flat surfaces (see figure 2.4). Here, a CDW wavevector $q_{\mathrm{CDW}} = 2k_F$ will be able to overlap more of the Fermi surface than in the two- and three-dimensional case and hence more overlapping of electron wave functions at the surfaces. This will result in a higher degeneracy and therefore a more efficient gap formation. This is referred to as good Fermi surface nesting conditions. Lastly, at high temperatures the free electron energy that can be potentially gained is reduced by thermal excitation of the electrons across the gap and therefore the CDW state is also only stable below a certain phase transition temperature.

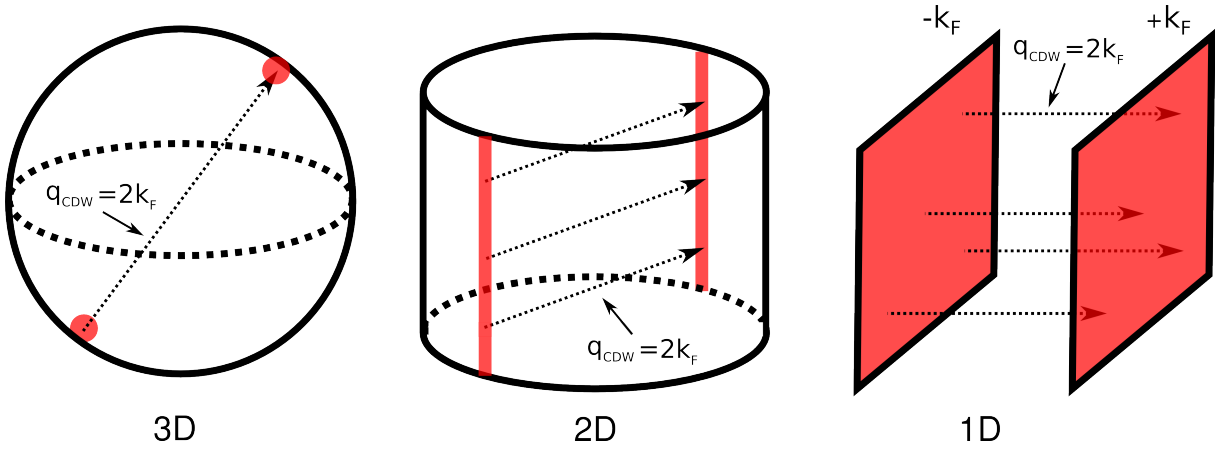

Figure 2.4: Comparison of Fermi surface nesting qualities in different dimensionalities. With a wave vector $q_{\mathrm{CDW}} = 2k_F$ more of the Fermi surface can be overlapped in a one- or two-dimensional system than for a three-dimensional system resulting in a more efficient gap formation at reduced dimensionality. Therefore a reduced dimensionality is favourable for the formation of a CDW

The structure of crystal lattices have been characterised and investigated by means of electron, x-ray or neutron diffraction for decades now. Since the formation of the CDW includes a slight modulation of the lattice atoms positions, the presence of a CDW is also observable in a diffraction pattern. The periodicity of the CDW is larger than the host lattice periodicity and so the CDW is seen as the appearance of diffraction peaks with a smaller periodicity in the reciprocal domain of the diffraction pattern. Since the amplitude of the superimposed CDW modulation is very weak, the periodicity is much less defined than the host lattice periodicity and therefore the intensity of CDW

Stellenbosch University http://scholar.sun.ac.za

diffraction peaks is also much fainter. This can be seen in figure 2.8 (d) where the faint CDW peaks are visible between brighter host-lattice diffraction peaks. In this way, CDW's were observed for the first time in the 1970's in several inorganic materials. The most studied being transition-metal dichalcogenides, MX_2 where M is typically one of the transition metals: Vanadium, Niobium, Titanium or Tantalum and X is a chalcogenide: Sulphur, Selenium or Tellurium [3]. More recently the formation of a CDW has also been observed in organic compounds like ($Cu(DCNQI)_2$) [59]. The common property of all these materials is that they are all quasi one- or two-dimensional which agrees with Peierls prediction that reduced dimensionality would aid the instability that causes the formation of a CDW.

In thermal equilibrium, the CDW compounds $TaSe_2$, TaS_2 and $NbSe_2$ were extensively studied and characterised in the 1970's [2, 3]. Recently time-resolved methods like femtosecond optical pump- probe spectroscopy [60], femtosecond x-ray [10] and electron diffraction [20] as well as femtosecond ARPES [61] have given researchers the ability to study some of these CDW materials in an out-of-equilibrium scenario. This approach has allowed for a deeper understanding of the processes involved that govern the formation, destruction and stability of the observed CDW. Transition-metal dichalcogenides in particular have become the preferred choice as a "toy-model" since changing the metal or chalcogenide, the polytypes involved in the layers or even intercalating of other elements into the material can effect the phase transition temperature, stability or primary principle behind the formation of the CDW [62].

2.3 The CDW material $4H_b$-$TaSe_2$

Crystal Structure of $4H_b$-$TaSe_2$

The material investigated in this thesis, $TaSe_2$, a quasi two-dimensional, layered, transition-metal dichalcogenide. The crystal structure within a layer consists of hexagonally arranged Se-Ta-Se atom sandwiches which can form two polytypes namely: trigonal prismatic, referred to as an H-layer, or octahedral, referred to as a T-layer (see figure 2.5).

There are strong covalent bonds between the tantalum and selenium atoms within a layer while the individual layers are only weakly bonded to another by van der Waals interaction. When the crystal consists of only T-layers it is known as $1T$-$TaSe_2$, and $2H$-$TaSe_2$ when there are only H-layers present. The numbers "1" and "2" indicate the number of layers required to define a unit cell. The specific polytype investigated here

Stellenbosch University http://scholar.sun.ac.za

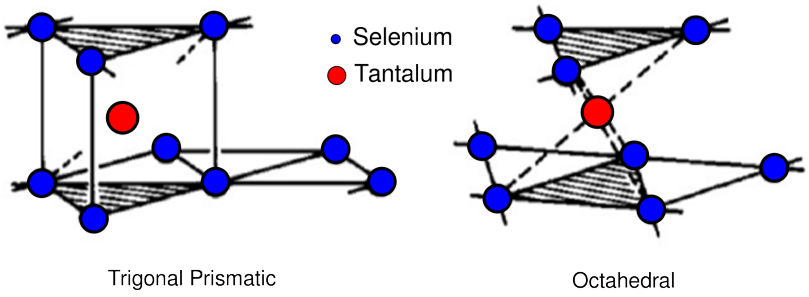

Figure 2.5: The different stacking structure of the Trigonal Prismatic and the Octahedral polytype.

is $4H_b$-$TaSe_2$ which consists of alternating H- and T-layers (see figure 2.6) and belongs to the space group $P6_3/mmc$ with the hexagonal lattice parameters of $a = b = 3.46$ Å and $c = 25.18$ Å [63].

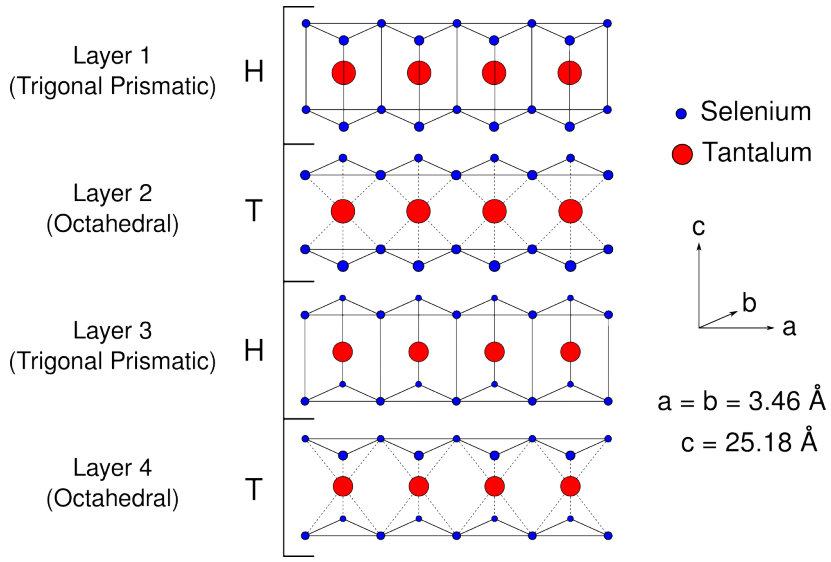

Figure 2.6: Crystal Structure of $4H_b$-$TaSe_2$: The crystal is composed of alternating layers of octahedral (T-layers) and trigonal-prismatic (H-layers) crystal structures. The hexagonal lattice constants are $a = b = 3.46$ Å and $c = 25.18$ Å [63].

Phases and Phase Transitions of $4H_b$-$TaSe_2$

Several phases, metallic, incommensurate-CDW and commensurate-CDW can be observed in $4H_b$-$TaSe_2$ depending on the temperature. Above 600 K the entire crystal is in the metallic phase with no CDW present in either the T- or the H-layers. Reducing the temperature below 600 K results in the formation of an incommensurate-CDW in only the T-layers with a modulation wave vector of $\mathbf{q}_{ic}^{T} = 0.265\mathbf{a}^*$. This is similar in the pure

Stellenbosch University http://scholar.sun.ac.za

	Commensurate Phase		Incommensurate Phase		Metallic Phase
	Temp.	CDW	Temp.	CDW	Temp.
T-layer	< 410 K	$q_c^T = 0.277a^*$ $\mathbf{q}_c^T \angle \mathbf{a}^* = 13.9°$	$410 - 600$ K	$\mathbf{q}_{ic}^T = 0.265\mathbf{a}^*$	> 600K
H-layer	not known	not known	< 75 K	$\mathbf{q}_{ic}^H = \frac{1}{3}(1+\delta)\mathbf{a}^*$ $\delta = 0.04$ at 10 K	> 75K

Table 2.1: Summary of the different phases in the T- and H-layers and at which temperatures the phases are present. The wave vectors for the relevant CDW's are also given [64].

1T-$TaSe_2$ (only T-layers present) except that the modulation wave vector in 1T-$TaSe_2$ is $\mathbf{q}_{ic}^T = 0.285\mathbf{a}^*$. Reducing the temperature further to below 410 K results in the formation of a commensurate-CDW, again only in the T-layers, where 13 Ta atoms cluster with a periodicity of $\sqrt{13}a \times \sqrt{13}a$ (see figure 2.8 (c)) and therefore it has a modulation wave vector $q_c^T = 0.277a^*$ with $\mathbf{q}_c^T \angle \mathbf{a}^* = 13.9°$. The displacement of the Ta atoms from their unmodulated positions is only 0.2 Å [65] and hence the much fainter CDW peaks. This commensurate-CDW is identical to the one in the pure 1T-$TaSe_2$ except that transition temperature in 1T-$TaSe_2$ is at 473 K. In both cases however the transition is of first order which can be seen in the sudden resistivity change at the respective temperatures (see fig 2.7). At this temperature there is still no CDW present in the H-layers but a slight structural modulation has been observed through neutron diffraction [64] and suggested to be due to elastic coupling with the T-layers. Only once the temperature is reduced even further to below 75 K does an incommensurate CDW form in the H-layers with a modulation wave vector of $\mathbf{q}_{ic}^H = \frac{1}{3}(1+\delta)\mathbf{a}^*$. This is again similar to the pure 2H-$TaSe_2$ except that the transition temperature is at 122 K for 2H-$TaSe_2$ and the CDW becomes commensurate at 90 K (δ becomes 0) while in 4H_b-$TaSe_2$ the CDW persists in the incommensurate phase down to 10 K where δ is still 0.04 [66, 64]. The incommensurate-CDW in the H-layers co-exists with the commensurate-CDW in the T-layers. The phases for 4H_b-$TaSe_2$ and the involved layers are summarised in table 2.1 [64] and the transitions can be seen in the resistivity changes shown in figure 2.7 [66].

Optically Induced Phase Transitions

Since the formation of a CDW includes a structural deformation of the lattice, a phase transition to the metallic or to a different CDW phase with a different modulation will entail atomic motion. Therefore a more in-depth understanding of their nature could

Stellenbosch University http://scholar.sun.ac.za

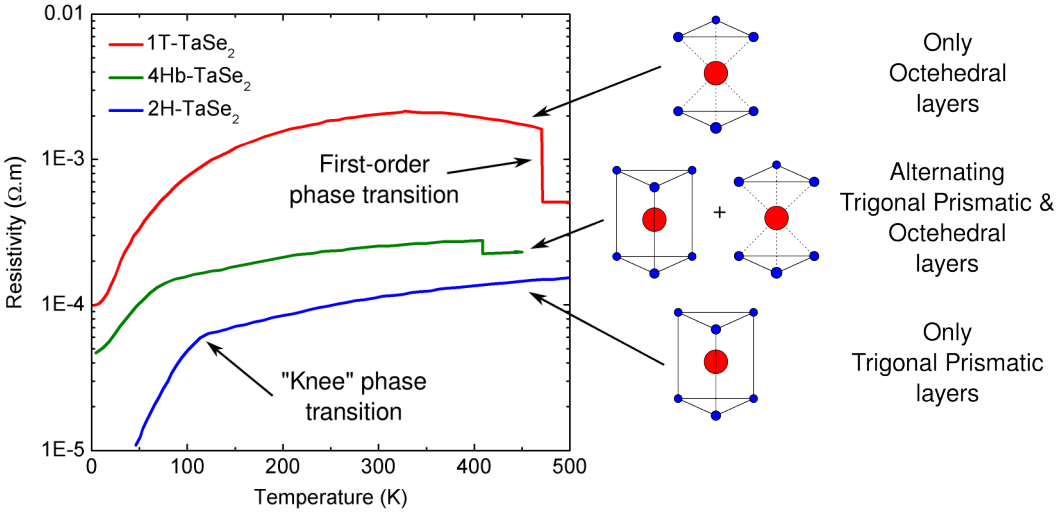

Figure 2.7: Plotted are the resistivity measurements from Di Salvo et. al. [66] for three polytypes of $TaSe_2$: $1T$, $4H_b$ and $2H$. $1T$-$TaSe_2$ composed of only T-layers has a first-order phase transition at 473 K from an incommensurate- to commensurate-CDW where the resistivity changes suddenly. $2H$-$TaSe_2$ composed of only H-layers has a non first-order, "knee" phase transition from the metallic to the incommensurate-CDW phase at 122 K. $4H_b$-$TaSe_2$ with alternating layers of T- and H-layers has both a first-order phase transition in only the T-layers at 410 K and a "knee" phase transition in only the H-layers at 75 K. Below 75K a commensurate-CDW in the T-layers co-exists with a incommensurate-CDW in the H-layers.

be gained by studying the phase transition on the time-scale of atomic motion.

This time-scale can be estimated by calculating the period of an acoustic phonon in the lattice. In other words, how fast will a lattice atom oscillate back and forth as the wave moves across it. By considering a system of identical atoms in a one-dimensional chain separated by a and elastically coupled to each other by a spring, the dispersion relation between angular frequency ω and the wave vector k of the wave is given by [56]:

$$\omega = \omega_m |\sin \frac{ka}{2}|, \tag{2.1}$$

with ω_m the maximum frequency. From this the maximum frequency is achieved when $k = \frac{\pi}{a}$ and from the definition of the wave-vector $k = \frac{2\pi}{\lambda}$ the minimum wavelength of an acoustic wave is therefore $\lambda_{min} = 2a$. The velocity of a sound wave in a transition-metal dichalcogenide, for instance $TiSe_2$, has been measured to be in the order of $v_s = 2000$ m/s [67]. With crystal constants for $TiSe_2$ of $a = b = 3.54$ Å [68], the frequency of the wave with the fastest oscillation is calculated to be: $f_s = \frac{v_s}{\lambda_{min}} = \frac{v_s}{2a} \approx 3$ THz which will have a oscillation period of roughly 400 fs. Therefore, in order to study the phase transition in its out-of-equilibrium state an experimental method with sub-picosecond resolution is required.

Stellenbosch University http://scholar.sun.ac.za

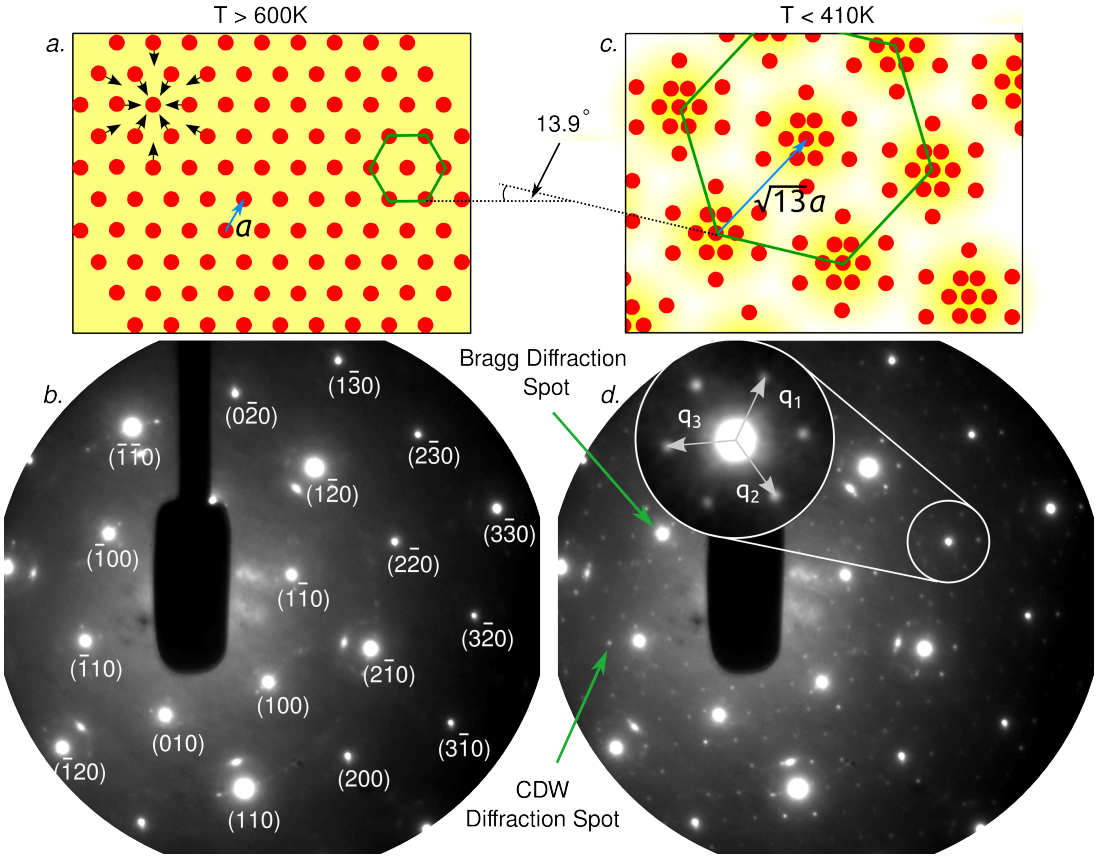

Figure 2.8: Shown in (a) and (c) are the positions of the Ta atoms in the T-layer in the a-b crystal plane for the metallic phase ($T > 600$ K) and the commensurate CDW phase ($T < 410$ K) respectively. In the metallic phase the Ta atoms are in their undistorted positions with a hexagonal arrangement which result in a hexagonal diffraction pattern shown in (b). Below 410 K the commensurate CDW is formed and 13 Ta atoms cluster (displacement exaggerated in the sketch) with a new periodicity of $\sqrt{13}$a $\times$ $\sqrt{13}$a. The larger periodicity manifests into a smaller periodicity in the reciprocal space of the diffraction pattern, resulting in CDW peaks appearing between the Bragg peaks in the diffraction pattern shown in (d) with a wave vector $\mathrm{q} = \frac{1}{\sqrt{13}}\mathrm{a}^* = 0.277\mathrm{a}^*$ and $\mathbf{q}\angle\mathbf{a}^* = 13.9°$.

Femtosecond pump-probe experiments with electron or x-ray probe pulses are therefore perfect candidates since the phase transition can be induced by depositing energy into the system optically with a femtosecond laser pulse and the structural evolution of the phase transition monitored with sub-picosecond resolved diffraction patterns. The phase transition can be optically induced because light couples directly to the electronic system and the electrons couple to the lattice because of strong electron-phonon coupling. In the chapter to follow the optically induced commensurate-to-incommensurate phase transition in $4H_b$-$TaSe_2$ is investigated by means of optical-pump and electron-probe experiments on the sub-picosecond timescale.

Stellenbosch University http://scholar.sun.ac.za

Stellenbosch University http://scholar.sun.ac.za

3. Time-resolved Structural Studies of $4H_b$-$TaSe_2$

In this chapter, two methods are used to investigate the sub-picosecond structural evolution of $4H_b$-$TaSe_2$ upon photo-excitation. More specifically, the structural changes within the crystal lattice are monitored while optically driving the commensurate-to-incommensurate (C-IC) charge density wave (CDW) phase transition in the T-layers (see figure 2.6 and table 2.1). The first method, conventional scanning Femtosecond Electron Diffraction (FED), is used as the main investigating tool while a new approach namely Femtosecond Streaked Electron Diffraction (FSED) is an attempt at significantly increasing the signal-to-noise ratio of the transient signals for the same data acquisition time.

3.1 Investigation of $4H_b$-$TaSe_2$ by means of Scanning Femtosecond Electron Diffraction

Experimental Procedure

From bulk $4Hb$-$TaSe_2$ single crystals, 100 nm thin sheets with a diameter of $\sim$100 μm were cut along the a-b crystal plane using an ultramicrotome as discussed in section 1.4. The cut samples were transferred to on TEM mesh as seen in figure 1.13.

The FED experiments were performed in a transmission geometry at room temperature with the sample being pumped nearly anti-parallel to the electron beam (see fig 1.1). Electron pulses with roughly 1000 e/pulse were generated to ensure a pulse duration of $<$ 500 fs at the sample position of 6 cm from the cathode. The current of the magnetic lens was adjusted such that the electron beam was focused onto the MCP which resulted in a weakly converging beam with a beam diameter (FWHM) of 200 μm at the sample. A 1000 mm lens was utilised to focus the pump pulse (775 nm) to a spot size of 1-2 mm onto the sample to ensure that all of the probed sample was pumped homogeneously. The fraction of the pump light reflected of the laser window on the vacuum chamber was directed onto a CMOS camera (Thorlabs DCC1545M, 1280 x 1024 pixels at 5.2 μm pixel size). The distance from the CMOS camera to the focusing lens was set equal to the distance from the sample to the same lens. The FWHM-area

Stellenbosch University http://scholar.sun.ac.za

of the pump beam at the sample could therefore be determined from the spatial profile obtained from the CMOS camera and the fluence calculated as follow:

$$F = \frac{P}{A \times f} \tag{3.1}$$

with P the average power and A the FWHM-area of the pump beam on the sample. The repetition rate of the laser is f. The average power of the pump beam was measured and adjusted to perform measurements at the desired fluence.

A 100 μm TEM aperture was also superimposed and secured on top of the TEM mesh where the best quality sample was located for three reasons. Firstly, the fringes of the electron beam (FWHM = 200 μm) covers several surrounding "squares" of the TEM mesh where the sample is located (see figure 1.13 (b)) and the aperture prevents any diffraction signal generated from these adjacent crystallites. Adjacent crystals could have a slightly different orientation to the main sample and produce unwanted "double" Bragg spots which could interfere with data extraction (see figure 3.1). Secondly, some of the remaining UV light that passes through the photo-cathode is prevented from reaching the MCP. The MCP is also sensitive to UV light and this causes unnecessary noise. Lastly, the aperture is used to align the pump beam such that there is spatial overlap of the electron and pump beam on the sample. Alignment is done with an infra-red viewer, used to detect and optimise the pump light passing through the aperture and therefore through the sample.

Once everything is aligned the experiment is commenced by running an in-house developed *Labview* program that executes as follow: A short, 5 seconds exposure image of the diffraction pattern is taken and the position (centre-of-mass) of a selected Bragg spot stored. The same is done for the position of the pump beam directed onto the CMOS camera used to also determine the FWHM-area of the pump beam. A 60 second exposure (60 000 shots) diffraction image is taken of the sample being pumped and another image for unpumped. The time delay between the optical pump pulse and the electron probe pulse is then adjusted by moving the delay stage. Again, a 5 seconds exposure image of the diffraction pattern is taken and the position of the selected Bragg spot is compared with the previously stored position. The same is done for the pump beam position and the positions are corrected, by means of piezo driven mirrors located in the relevant arm, if required. The next pair of pump and unpumped image can then be taken and the whole process repeated for the required time steps to generate a transient signal. After pumped and unpumped images at all the delay times are taken a "scan" is completed. Typically 6-10 scans are taken and averaged to generate a transient signal as seen in figure 3.4. With 30-40 data points, each derived

Stellenbosch University http://scholar.sun.ac.za

from a 60 seconds exposed pumped and unpumped image pair, a single scan takes in the order of 1 hour if beam correction time is also considered. With several scans required for good signal-to-noise ratio a single transient could take up to 10 hours to obtain.

Another measurement done was fixing the pump-probe time delay to about 1 ps after time-zero and measuring the suppression of the CDW signal as a function of pump fluence. This delay roughly corresponds to the time where the minimum of the CDW signal for all fluences was achieved (see figure 3.6 (b) and inset of figure 3.8).

Data Extraction Procedure

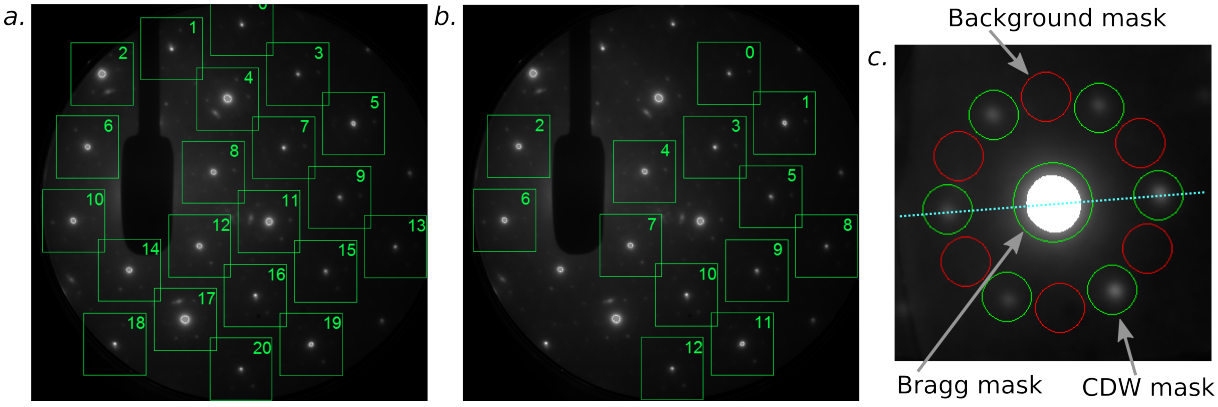

Figure 3.1: Panel (a) shows all the Bragg peaks initially detected by the circle detection algorithm while panel (b) shows the selected Bragg peaks after the user has deselected peaks that were partially obscured or containing strange intensity artefacts. In panel (c) the intensity-averaged image of all the selected Bragg spots is shown. Here the central Bragg spot is surrounded by six well defined CDW peaks. The position of the Bragg, CDW and background masks are also shown, which are used to calculate the relative signal intensity. Note that the Bragg peaks are not saturated as it appears but that the images are scaled to make the CDW signals more visible.

A *Labview* program (see Appendix A) was written to extract the data from the diffraction images. A generic *Labview* circle detection function was firstly used to detect the positions of the Bragg peaks in each image (see figure 3.1 (a)). The program then allowed the user to deselect Bragg peaks together with the surrounding CDW peaks that were either partially obscured by the beam block or partially off the detector (see figure 3.1 (a) peaks 0, 1, 2, 14 & 18). Bragg peaks that had any strange intensity artefacts in close vicinity (see figure 3.1 (a) bottom left of peak 4) that could compromise the CDW signal were also deselected which resulted in the final selected Bragg peaks shown in figure 3.1 (b). All the selected Bragg peak images, indicated by the green squares,

Stellenbosch University http://scholar.sun.ac.za

were extracted and intensity averaged. In all visible diffraction orders (see figure 2.8 for Miller indices), both CDW and Bragg peaks showed identical temporal evolution. Thus, for the sake of increasing the signal-to-noise ratio, all available diffraction orders were averaged over. Suitable masks for the Bragg, CDW and background signals were chosen as seen in figure 3.1 (c).

The total pixel count within the Bragg and CDW masks was calculated and the appropriately scaled pixel count obtained from the background (bg) mask was subtracted from each. This was done for a pair of "pumped" (p) and "unpumped" (u) diffraction images (for a certain pump-probe delay) and the signal for the Bragg and CDW is then separately calculated as follow:

$$\frac{\Delta I}{I_0} = \frac{(I_p - I_{bg}) - (I_u - I_{bg})}{(I_u - I_{bg})}. \tag{3.2}$$

Here a signal of zero indicates no change in intensity while a signal of -1 and 1 indicates a full suppression or doubling of intensity respectively. This whole procedure can then be repeated for each pair of "pumped" and "unpumped" diffraction images for all the pump-probe delays and plotted as seen in figure 3.4.

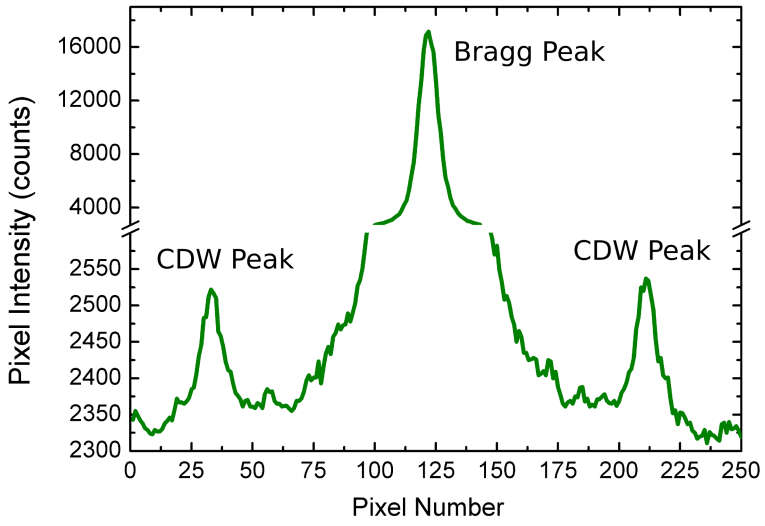

Figure 3.2: Plotted is the pixel count along the dashed line indicated in figure 3.1 (c). The break in the vertical axis of the graph highlights the bit-depth of the CCD detector since the small CDW signals (∼200 counts) as well as the large Bragg signal (∼14 000 counts) can be resolved in the same image without saturation of the detector occurring.

From the data-extracting image shown in figure 3.1 (c), the quality of the extracted data can now be discussed in more detail. Plotted in figure 3.2 is the intensity profile along the dotted line intersecting two of the CDW peaks and the central Bragg peak.

Stellenbosch University http://scholar.sun.ac.za

Firstly, the break in the vertical axis of the graph highlights the bit-depth of the CCD detector since the small CDW signals (∼200 counts) as well as the large Bragg signal (∼14 000 counts) can be resolved in the same image without saturation of the detector occurring. Actually only a quarter of the 16-bit bit-depth ($2^{16} = 65536$) is utilised with the exposure time of this image (60 seconds), electron beam current (1000 e/pulse) and MCP voltage (4500 V i.e. maximum voltage). The low electron number is chosen to ensure $<$ 500 fs electron pulses at the sample (see figure 1.8) and the shorter than optimal exposure is chosen as a compromise to facilitate two other benefits. Short exposures prevent the smearing of diffraction peaks due to possible beam drift occurring during an image exposure. Beam-direction correcting procedure can take place between successive images (see previous subsection). Shorter exposure times are also beneficial since minimising the time spent collecting data for a single data point in the transient decreases the time it takes to complete a transient "scan". This minimises the risk of getting a "scan" interrupted unexpectedly which could make previously collected data redundant. In other words it is better to average over many quick, higher-noise "scans" than to take one time-consuming, lower-noise "scan".

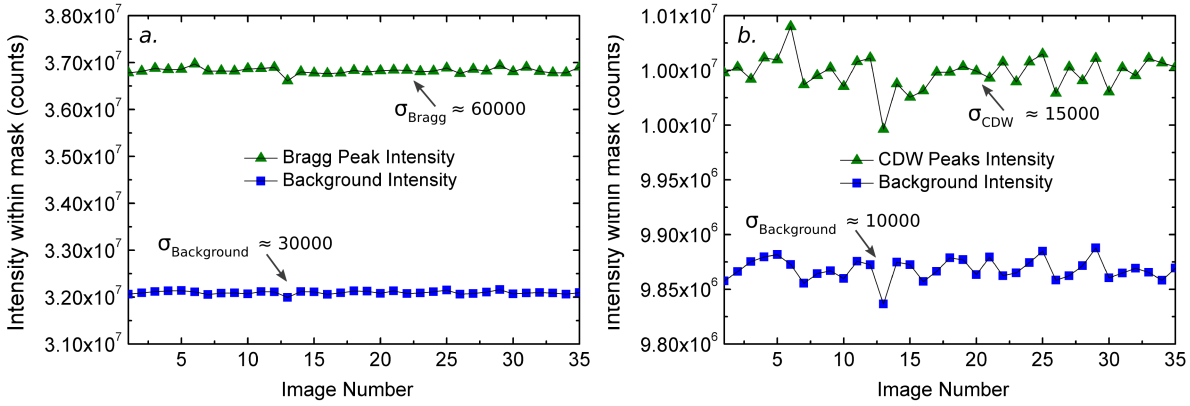

Figure 3.3: Plotted in panel (a) is the sum of the pixel counts within the Bragg mask and the Bragg background mask (see figure 3.1 (c)) for 35 consecutive unpumped diffraction images. The experimental conditions were the same as during the pump-probe experiment i.e. 60 seconds exposure, 1000 e/pulse and a MCP voltage of 4500 V. Panel (b) shows the equivalent plots for the CDW mask and the CDW background mask. The standard deviation σ is also indicated for each plot.

The other thing that can be learned from figure 3.2 is that with a background of around 2300 counts the CDW signal is about 200 counts whereas the Bragg is around 14 000 counts. This makes the CDW signal strength only ∼1.5 % of the Bragg signal. Therefore the expected signal-to-noise will be much worse for the CDW signal. Plotted in figure 3.3 (a) are the total pixel counts obtained from the Bragg and Bragg background masks (after averaging over all available diffraction orders, see figure 3.1 (b)) for 35

Stellenbosch University http://scholar.sun.ac.za

consecutive unpumped images. The experimental conditions were the same as during the pump-probe experiment i.e. 60 seconds exposure, 1000 e/pulse and an MCP voltage of 4500 V. Panel (b) shows the equivalent data for the CDW and CDW background mask. The standard deviation σ is also indicated for each plot.

Assuming that the standard deviation for the pumped images is identical to the unpumped images, the standard deviation for each variable in equation 3.2 is determined and so also the standard deviation (error bars) for the data points of the transient signals. For the normalised change in the Bragg signal $\frac{\Delta I}{I_0}$, the error is calculated to be ± 0.015 and for the CDW signal ± 0.13. For the transients shown in figure 3.4 the error bars are shown. Since these transients are the result of averaging over 6 "scans" (i.e. averaging over 6 images per data point) the error is $\pm\frac{0.015}{\sqrt{6}} = \pm 0.006$ for the Bragg signal and $\pm\frac{0.13}{\sqrt{6}} = \pm 0.05$ for the CDW signal.

Results and Discussion

In figure 3.4 the transient signals of the Bragg and CDW diffraction peaks are shown with the pump fluence high enough to fully suppress the CDW signal, 2.6 mJ/cm^2 in this case. In the Bragg signal there is an initial rise of 4% of the signal within the temporal resolution of the experiment ($\sim$500 fs) and then it decays to just under the original unpumped value on a slightly longer time-scale of around 1 ps. The CDW signal decays down to zero intensity on a time-scale of around 1 ps and remains that way for the visible future time of 3.5 ps. The decay of the CDW signal as well as the initial rise of the Bragg signal indicates that during this time the crystal structure has begun to revert back to its unmodulated state where the scattering efficiency into the Bragg peaks would increase and the scattering efficiency into the CDW peaks lowered. Once the Bragg signal has reached its maximum (see solid line) it starts to decay, the CDW signal also decays further indicating that the lattice is not returning to its modulated state but rather undergoing a change or motion that would lower the scattering efficiency into both the CDW and the Bragg peak. For instance incoherent vibration of the lattice.

From the behaviour of the two transients the following model is proposed that describes two processes simultaneously occurring at the onset of time zero: (1) photo-excitation of the electrons and initial e-e scattering drastically modifies the electron density distribution which in-turn smears out the inter-atomic potential related to the CDW periodicity. This causes a coherent relaxation or "breathing" mode of the 13 Ta atoms back to their original unclustered positions (i.e. non-thermal melting of the PLD, see figure 2.8 (c) and (a)), which results in a rise in the Bragg signal and decay in the

Stellenbosch University http://scholar.sun.ac.za

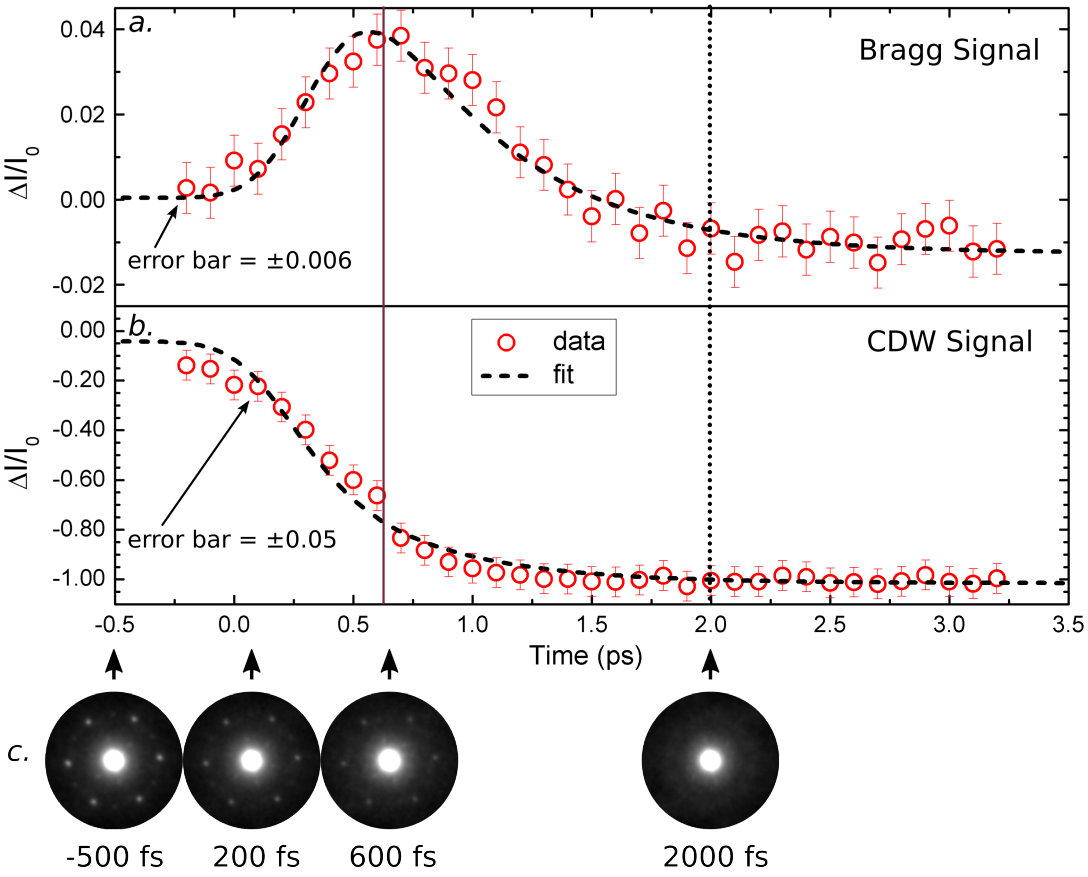

Figure 3.4: Plotted are the transient signals of (a) the Bragg and (b) the CDW diffraction signals for a pump fluence high enough, 2.6 mJ/cm^2 in this case, to fully supress the CDW peaks. Panel (c) shows the change in intensity of the CDW diffraction peaks at the indicated pump-probe delays.

CDW signal. (2) electron-phonon coupling causes the energy in the electronic system to be transferred to the lattice and results in incoherent vibration of the lattice, in other words the Debye-Waller effect. This incoherent vibration causes a decay in the Bragg as well as in the CDW signal. This model can be fitted to the data by the sum of two exponential functions with two time constants namely τ_{coh} (for the coherent "breathing" motion) and τ_{icoh} (for the incoherent lattice vibration) such that:

$$\frac{\Delta I}{I_0}(t) = C_1(1 - e^{-t/\tau_{\text{coh}}}) + C_2(1 - e^{-t/\tau_{\text{icoh}}}), \tag{3.3}$$

with $C_1 < 0$ and $C_2 < 0$ for the CDW signal since both the coherent and incoherent processes causes the decay of the CDW signal and $C_1 > 0$ and $C_2 < 0$ for the Bragg signal since the coherent process causes a rise in the Bragg signal and the incoherent process causes a decay in the Bragg signal (see also figure 3.5).

Several amplitude modes around 70 cm^{-1} (i.e. a period of ∼480 fs) have previously

Stellenbosch University http://scholar.sun.ac.za

been reported in $4H_b$-TaS_2 [69]. In the proposed model, the Ta atoms are back at their original unclustered positions at $\frac{1}{4}$ period of the coherent "breathing" oscillation. Therefore, in the fitting procedure τ_{coh} was fixed to $\frac{480}{4} = 120$ fs. The fitted function was also convolved with a Gaussian function with a FWHM of 400 fs to include the temporal response of the setup. With these in place the extracted time constant τ_{icoh} was 550 fs. This is related to the electron-phonon coupling strength and with this short time it is indicative to strong coupling. The extracted time constant was equal for both the Bragg and CDW signals and the time constant also agrees with a previous FED study on another transition-metal dichalcogenide, $1T$-TaS_2 [20].

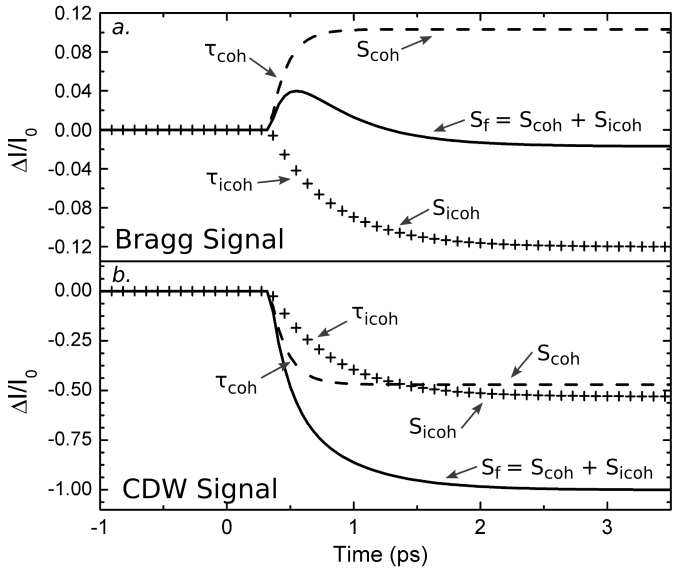

Figure 3.5: Plotted are the two exponential functions modelling the coherent "breathing" mode (dashed lines) and incoherent vibrations (crosses) of the lattice upon excitation. The coherent amplitude mode pushes the lattice to its unmodulated state thereby increasing the Bragg intensity and decreasing the CDW peak intensity. The incoherent vibrations (Debye-Waller effect) cause a drop off in both the Bragg as well as in the CDW peak intensities. The final fitted function (solid lines) is the sum of the two exponential functions (see fits in figure 3.4). See also Appendix A for *Matlab* code of fitting procedure.

Plotted in figure 3.6 is the same measurement as in the previously discussed transients shown in figure 3.4 but now for different pumping fluences. The time constant extracted for τ_{icoh} for all fluences was the same (550 fs) but it is clear that there are two pumping regimes: either a perturbation or a full suppression of the CDW signal is achieved. In the perturbative regime with pump fluences of 1.7 mJ/cm^2 (30% suppression) and 2.3 mJ/cm^2 (70 % suppression) the CDW is not completely destroyed and there is evidence of a recovery process even on the short time-window displayed. With a fluence of 2.6 mJ/cm^2 the CDW signal is completely suppressed and no recov-

Stellenbosch University http://scholar.sun.ac.za

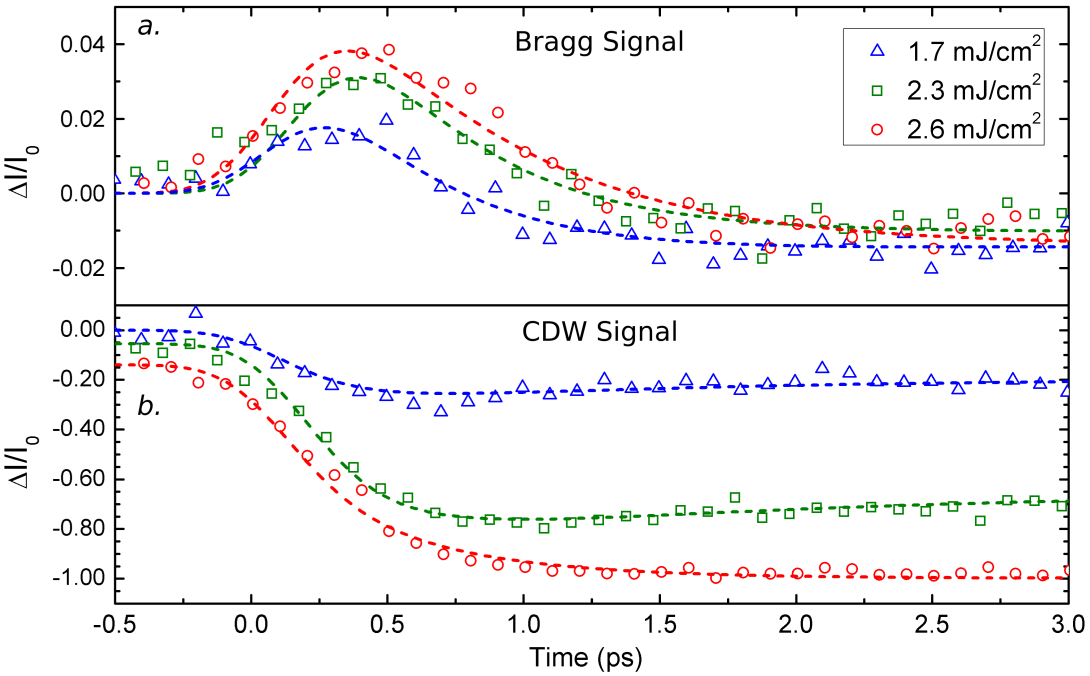

Figure 3.6: Plotted are the transient signals of (a) the Bragg and (b) the CDW diffraction signals for three different pump fluences: 1.7 mJ/cm^2, 2.3 mJ/cm^2 and 2.6 mJ/cm^2. In the perturbative regime with pump fluences of 1.7 mJ/cm^2 (30% suppression) and 2.3 mJ/cm^2 (70 % suppression) the CDW is not completely destroyed and there is evidence of a recovery process. With a fluence of 2.6 mJ/cm^2 the CDW signal is completely suppressed and no recovery is evident on the displayed time-scale.

ery is evident on the displayed time-scale. To get a better idea of the recovery times, a measurement at larger pump-probe delays was done and the results for the CDW signals are shown in figure 3.7 for pumping fluences of 2.3 mJ/cm^2 (perturbative) and 2.6 mJ/cm^2 (full suppression).

The 150 ps recovery time for the perturbative regime is almost two orders of magnitude slower than the 4 ps observed for 1T-TaS_2 in a previous femtosecond electron diffraction study [20]. A suggested explanation for the longer recovery time in $4H_b$-$TaSe_2$ vs. 1T-TaS_2 is the following: In $4H_b$-$TaSe_2$ there are alternating T- and H-layers (see figure 2.6) with only a CDW present in the T-layers at room temperature. 1T-TaS_2, which is only comprised of T-layers, has a CDW present in all its layers. We propose that in $4H_b$-$TaSe_2$ the non-CDW carrying H-layers act as shielding layers, hindering any coupling between the CDW carrying T-layers. This could result in a less stable CDW formation and hence the longer recovery time required. Our proposed model therefore suggests that a single isolated layer would not easily host a CDW. However, this suggestion would contradict the idea that lower dimensionality favours CDW formation (see section 2.2) since a single isolated layer would be lower dimensional than

Stellenbosch University http://scholar.sun.ac.za

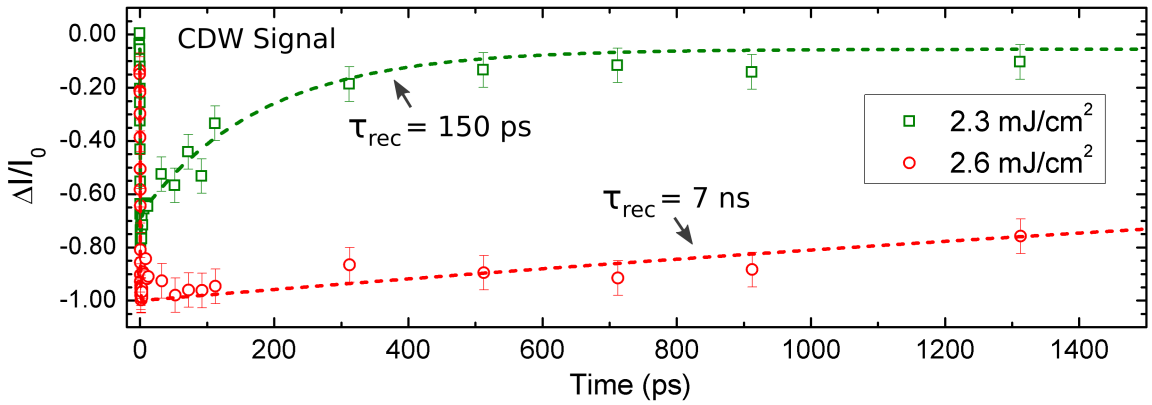

Figure 3.7: Plotted are the transient signals of the CDW diffraction signals for the two higher fluences seen in figure 3.6 but for longer pump-probe delay times. In the perturbative regime with a pump fluence of 2.3 mJ/cm^2 (70% suppression) the recovery time is in the order of 150 ps. With a fluence of 2.6 mJ/cm^2, where the CDW signal is completely suppressed, the recovery time is in the order of several nanoseconds.

several coupled layers. Recently in other studies, the classical picture of lower dimensionality favouring CDW has been challenged [70] since the nesting condition derived from the topology of the Fermi surface and the observed CDW modulation vectors are not generally equal. Our results could support this new notion.

The much longer several nanoseconds required for the recovery of the fully suppressed CDW is accredited to completely destroying the commensurate CDW and possibly driving the lattice into the incommensurate CDW phase. Therefore the commensurate CDW has to either reform from thermal noise with no modulation in the crystal lattice still present (an unordered state) or a modulation with a different geometry present (an ordered state but with a different geometry). This is different to the partially destroyed CDW in the perturbative pumping regime where the commensurate CDW can reform and recover from a still-present modulation with the same geometry.

The final measurement done was measuring the degree of CDW suppression as a function of pumping fluence. Plotted in figure 3.8 is the normalised change intensity $\frac{\Delta I}{I_0}$ of the CDW signal at its minimum (i.e $\sim$ 1 ps after t_0) as a function of pumping fluence. Although this is a profoundly non-equilibrium state, the lattice is at its maximum temperature at $\sim$1 ps since the electron-phonon coupling time of 550 fs means that the energy has been transferred to the lattice already. When the sample is pumped a certain amount of energy is deposited and this results in a temperature increase within the sample. This temperature increase is dependent on the absorbed energy. The absorbed

Stellenbosch University http://scholar.sun.ac.za

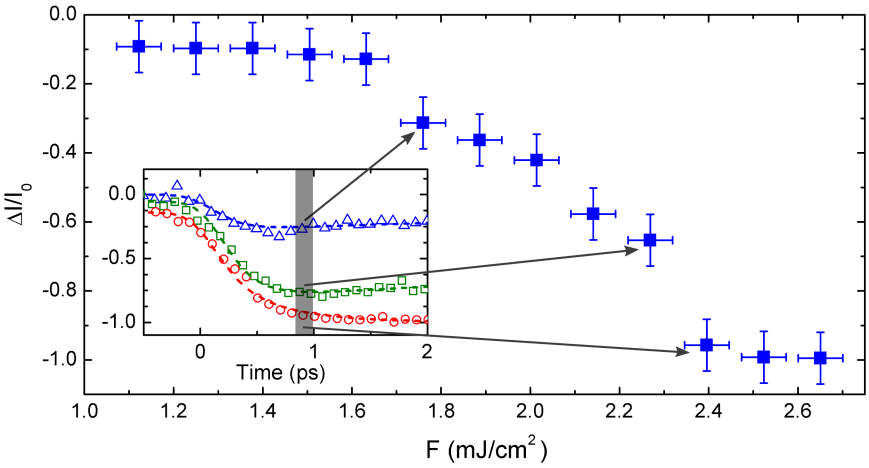

Figure 3.8: Plotted is the degree of suppression of the CDW signal as a function of the pump fluence roughly 1 ps after time zero (i.e. when the minimum at all fluences is achieved). A value of zero indicates no change in diffraction signal while a value of -1 means full suppression of the signal (see equation 3.2). The inset illustrates three examples of which data points were used. Here it is clear a fluence of $\sim$2.5 mJ/cm^2 is sufficient to fully suppress the CDW diffraction signal.

energy per unit volume at a certain fluence is given by:

$$E_a = F \times \frac{T(1 - \mathrm{e}^{-d/\alpha})}{d}, \tag{3.4}$$

with $T = (1 - R)$ the transmittance of the sample, α the absorption coefficient and d the thickness of the sample. Note that this is the average absorbed energy per unit volume and that the absorbed energy is only homogeneous throughout the whole sample if $d < \frac{1}{\alpha}$, which is the case for this experiment with $d = 100$ nm and $\alpha = 110\ \mathrm{nm}^{-1}$ at a wavelength of 775 nm [71]. For a fluence of 2.5 mJ/cm^2 corresponding to the threshold fluence for full suppression of the CDW signal (see figure 3.8), a sample thickness of 100 nm and a reflectivity of $R = 0.23$ [71] the absorbed energy per unit volume is calculated to be $E_a = 115$ J/cm^3. The temperature increase is then calculated as follow:

$$\Delta T = \frac{E_a \times V_\mathrm{n}}{C}, \tag{3.5}$$

with C the heat capacity and $V_\mathrm{n} = V_\mathrm{uc} \times N_A$ the molar volume. $V_\mathrm{uc} = a^2 c \sin(60^\circ)$ is the unit cell volume of a hexagonal crystal and N_A Avogadro's constant. The heat capacity of $4H_b$-$TaSe_2$ is $C = 171.3$ J/mole.K at 300 K [72] and the molar volume of $4H_b$-$TaSe_2$ is $V_\mathrm{n} = 157$ cm^3/mole. With a fluence of 2.5 mJ/cm^2 ($E_a = 115$ J/cm^3) the temperature increase is then $\Delta T = 106$ K. Considering the starting room temperature

Stellenbosch University http://scholar.sun.ac.za

of 300 K, the final temperature is 406 K which matches nicely with the phase transition temperature of 410 K (see fig 2.7 and table 2.1).

The above calculation can be done for all fluences used in figure 3.8 and the x-axis converted to temperature. The intensity of the CDW peaks is related to the square of the CDW modulation amplitude (i.e. by how much the Ta atoms are displaced from their unmodulated positions) such that $I \propto (\mathbf{q}_{cdw} \cdot \mathbf{A})^2$ with $\mathbf{q}_{cdw}$ the CDW wave vector and $\mathbf{A}$ the atomic displacement. The y-axis can therefore be converted to the normalised CDW amplitude. The result of these conversions is plotted in figure 3.9 (a). Included is the resistivity also as a function of temperature (measurements from Di Salvo et. al. [66], see also figure 2.7). Plotted in panel (b) is the theoretical behaviour of the energy gap as well as the resistivity as a function of temperature for a typical superconductor [58]. Since the amplitude of the CDW modulation is directly related to the band gap size in a CDW material (see section 2.2 and figure 2.3), comparison can now be drawn between the plots in the two panels.

Firstly, as in the superconductor, when approaching T_c from a higher temperature there is a sudden change in the resistivity of the CDW material at T_c when the gap starts appearing. In the CDW material the gap forms at the Fermi-surface (see figure 2.3) so it becomes electrically insulating and the resistivity increases while in the superconductor the gap causes the formation of electron Cooper-pairs which are free to flow without resistance and the resistance becomes zero.

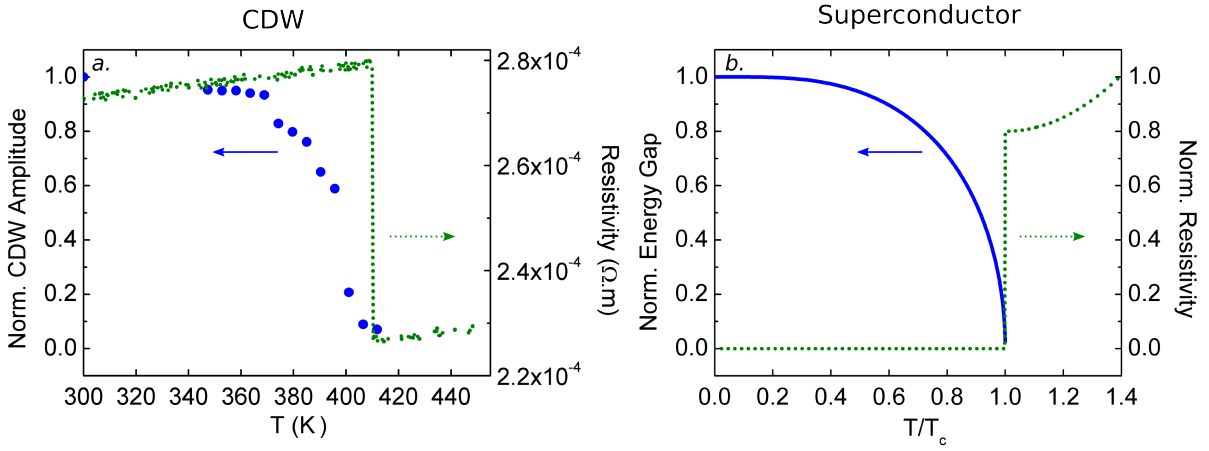

Figure 3.9: Plotted in panel (a) is the normalised CDW amplitude and the resistivity as a function of temperature of $4H_b$-$TaSe_2$ (resistivity from Di Salvo et. al. [66], see also figure 2.7). Panel (b) shows the theoretical behaviour of the energy gap and resistivity of a superconductor as a function of temperature, T_c is the critical temperature where super-conductance occurs.

Secondly, the size of the gap in the superconductor and the amplitude of the lattice modulation (i.e. size of the energy gap) in the CDW material have remarkable similar

Stellenbosch University http://scholar.sun.ac.za

trends. The gap size Δ in a superconductor is described by BCS (Bardeen-Cooper-Schrieffer) theory and given by [73]:

$$\frac{\Delta}{\Delta_0}(T) = \tanh\left[1.74\sqrt{\frac{T_c}{T} - 1}\right], \tag{3.6}$$

with $\frac{\Delta}{\Delta_0}$ the normalised energy gap and T_c the superconducting phase transition temperature and also the only free parameter. In figure 3.10 the CDW amplitude as a function of temperature (same data as panel (a) of figure 3.9) is plotted with the BCS prediction given by equation 3.6 with T_c set to the C-IC CDW phase transition temperature of 410 K. There is a very good agreement between the measurement and the BCS theory. Two things can be learned from this: (1) The calculation of mapping the fluence deposited into the sample to a temperature increase of the sample is correct. (2) The formation of the energy gap associated with the CDW modulation can possibly be described by the same theory that is used to describe the energy gap formation of superconductors. Since both are highly correlated material with strong electron-phonon coupling this might not be so surprising.

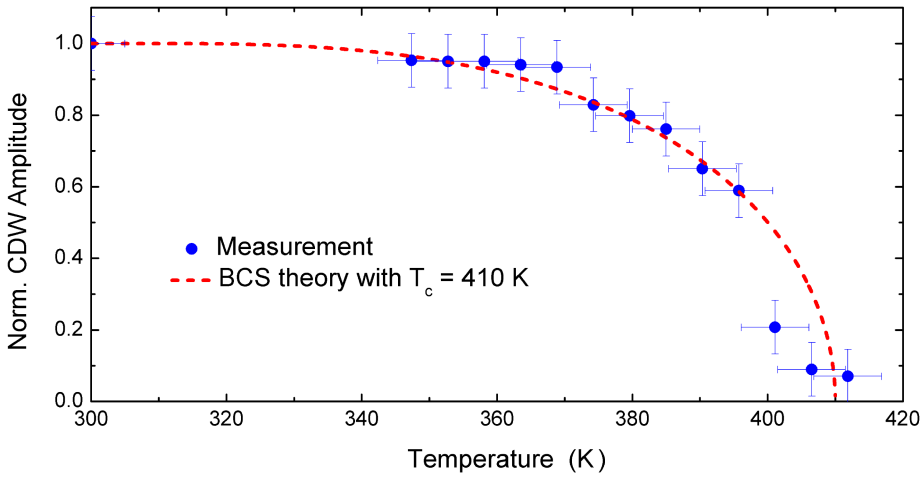

Figure 3.10: Plotted is the CDW amplitude as a function of temperature and the prediction from BCS theory (see equation 3.6) with T$_c$ set to the C-IC CDW phase transition temperature of 410 K in 4H_b-TaSe$_2$.

Closing remarks

For the experiment it is believed that the C-to-IC CDW phase transition is acheived but nowhere in the data is there evidence of the formation of the IC phase. From the values in table 2.1, the appearance of the IC-CDW peaks between and in-line with the

Stellenbosch University http://scholar.sun.ac.za

Bragg peaks is expected. These peaks are not visible in any of the collected diffraction patterns. There are two possible reasons: (1) the pump pulse was intense enough to directly drive the sample into the metallic phase or (2) the IC-CDW amplitude is too small for diffraction peaks to be generated with the current experimental setup. Reason one can be excluded since the IC-CDW signature would therefore have been visible at the lower fluence measurements, which was not the case. More recent measurements with our setup on a simaillar but different CDW material, $1T$-TaS_2, have shown the formation of the IC-CDW but the intensity of IC-CDW peaks were however much lower. This would make reason two the probable explanation.

Using the conventional scanning Femtosecond Electron Diffraction technique, extremely good quality data was collected of the structural evolution in $4H_b$-$TaSe_2$ during the C-to-IC CDW phase transition. The quality of the data and complexity of the sample under investigation is on par with the top current research outputs in the field of FED and an abundance of information about the atomic mechanisms involved with CDW formation could be extracted, analysed and discussed. Even so, there are some further experiments that could be pursued:

The result of the much longer, 150 ps, recovery time of the CDW signal in $4H_b$-$TaSe_2$ compared to 4 ps in $1T$-TaS_2 which comprises of only T-layers is contributed to the shielding effect of the non-CDW (at room temperature) carrying H-layers present in $4H_b$-$TaSe_2$. This decoupling of the CDW carrying T-layers results in a less stable CDW and hence the longer recovery time. What could be interesting is to conduct similar experiments on a polytype with even more shielding layers between the CDW carrying T-layers and see if the recovery time is even longer and therefore conclude that the CDW becomes even less stable. This would even further support recent studies [70] that challenge the classical picture of lower dimensionality favouring CDW formation.

Another interesting experiment would be to cool the sample to below 75 K such that there is a CDW present in both the T-layers and the H-layers (see table 2.1). The two CDW have different geometries and therefore spatially separated diffraction peaks and could be monitored individually. Pumping with a fluence that completely suppresses the H-layer CDW but not the T-layer CDW and monitoring their dependence on one another will be interesting.

Stellenbosch University http://scholar.sun.ac.za

3.2 Investigation of $4H_b$-$TaSe_2$ by means of Femtosecond Streaked Electron Diffraction

Motivation and Introduction

As already extensively discussed in Chapter 1, one of the major hurdles in conventional femtosecond electron diffraction at non-relativistic energies is maintaining sub-picosecond temporal resolution when increasing the electron number to above 10^3 e/pulse. Due to Coulomb repulsion within the laterally and longitudinally confined bunch, highly charged bunches dramatically broaden in pulse duration as they propagate (see figure 1.8). Since the temporal resolution in conventional scanning electron diffraction is limited by the convolution of the optical pump-pulse and the electron probe-pulse, the envisaged sub-picosecond resolution is lost. The simple and obvious approach to maintain good temporal resolution is is to keep the experimental setup as compact as possible and the electron number per bunch around 1000. This approach, as demonstrated in section 3.1, has successfully been applied to investigate for example ultrafast non-thermal melting processes and heating of metals, as well as charge density wave dynamics in transition metal dichalcogenides [19, 74, 75, 48, 20, 22]

An exciting recent development and trend to overcome the problem of Coulomb explosion but preserve large electron numbers involves re-compressing the broadened electron pulse using high-Q, radio-frequency, cavity or photo-triggered, open-cavity compressors [25, 26, 27, 76]. Reflectron compressors with static electric fields have also been proposed [23] but never realised due to their limited flexibility. Compressors have been reported to produce electron pulses of less than 100 fs containing 10^6 electrons [26] and have been successfully implemented in an actual pump-probe experiment [51]. While pilot experiments for high quality RF and photo-triggered open cavity compressors have proven the promising concepts, routine application will be implemented in the near future. However, a particular concern with conventional RF compressors is the synchronization of the laser generated electron pulse with the electronic RF signal which can lead to timing jitter of around 400 fs [26, 76] currently limiting the achievable temporal resolution.

In this section of the thesis an alternative solution to achieving sub-picosecond resolution is proposed and demonstrated. The technique aims to utilise the temporally Coulomb-broadened electron pulse to its advantage. As in the conventional pump-probe set up a 150 fs laser pump pulse is still used, but instead of an $\sim$400 fs electron probe pulse, a several picosecond long electron pulse is implemented to probe the sam-

Stellenbosch University http://scholar.sun.ac.za

ple. In this method different temporal components of the electron pulse are diffracted off the sample at different times before and after photo-excitation (see figure 3.11).

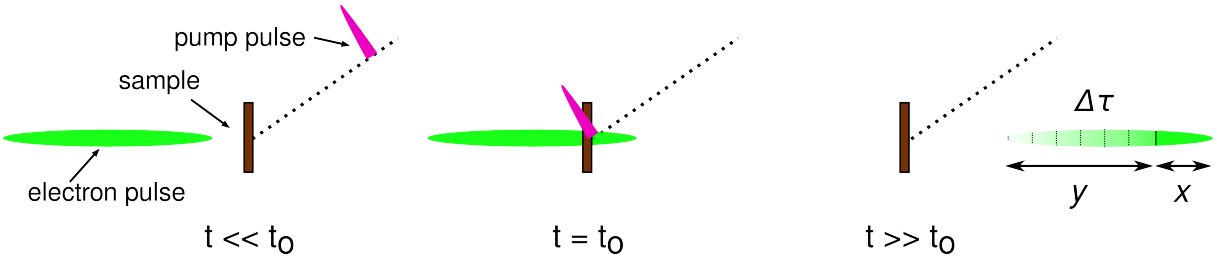

Figure 3.11: Principle of streaked diffraction: t_0 is chosen such that section x of the long electron pulse passes through unpumped sample while section y of the pulse observes the sample after it has been pumped. Different temporal components, $\Delta\tau$, of the electron pulse probe the sample at different times after photo-excitation.

The different temporal components of the diffracted signal are then spatially separated on the detector screen by means of an in-house developed photo-triggered streak camera (see figure 3.12 and section 1.3 for more details on the streak camera design and specifications). The resultant streaked diffraction pattern can be seen in figure 3.14 (b). The transient signal can then be obtained by taking an intensity profile of the streaked diffracted pulse.

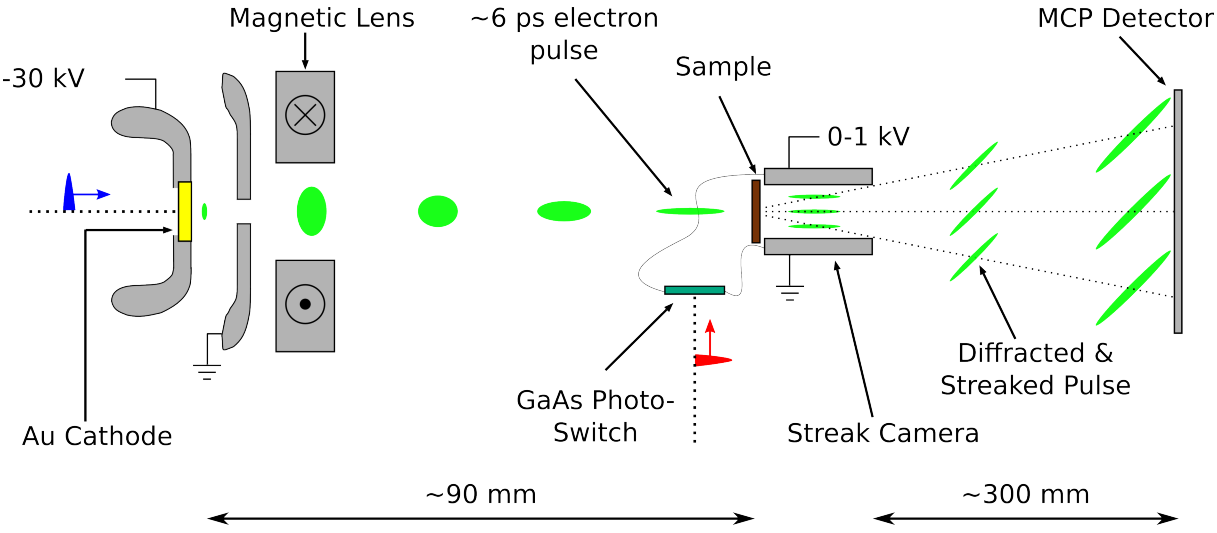

Figure 3.12: Principle of streaked diffraction continued: A highly charged electron pulse is allowed to Coulomb expand to ~6 ps, diffracted off the sample and then passed between the streaking plates. The streak-camera spatially separates different temporal components of the pulse on the detector screen by streaking each diffracted pulse.

The advantages of the streaked electron diffraction technique over conventional scanning electron diffraction include the following: (a) the entire temporal evolution of the

Stellenbosch University http://scholar.sun.ac.za

sample is contained in a single shot which means there is no need for a delay stage as in conventional pump-probe experiments. Fewer moving components allows for easier maintenance of pump-probe overlap as well as simplifying automated implementation of the experiment, (b) because of the parallel capturing of temporal information, as opposed to the serial data acquisition in conventional scanning electron diffraction, there is the potential for a significant increase in signal-to-noise ratio per data acquisition time, (c) because the entire temporal evolution of the sample is contained in a single shot and there is the potential for improved signal-to-noise there is the feasibility to perform a true single-shot-experiment on a sample that can only be pumped once and finally, (d) the experimental temporal resolution is not determined and limited by the electron pulse duration as in conventional scanning electron diffraction but rather on the streak camera's response, which with a photo-triggered streak camera design like ours can be around 150 fs [18], and thus there is scope for higher temporal resolution with this technique.

Disadvantages of the technique are that (a) the time-window of the observed transient can be relatively small (2-5 ps). This is limited by the length of the streaks allowed before overlapping of adjacent streaks occurs (discussed in more detail and quantified later). This problem can however be remedied by including a delay stage, shifting the observed time-window and stitching the data together. (b) The sensitivity for very small signals might be lower since the signal is now being spatially spread out of over detector but this again is not such a big issue since the electron number can be increased without sacrificing temporal resolution.

The technique of streaking the electron pulse to spatially separate different temporal components was already proposed in the 1980's [77]. Recently it was implemented with sub-picosecond resolution in time-resolved electron diffraction with relativistic electrons using an electronically synchronized high-Q, RF-cavity based streak camera [29, 78]. Since the technology used is the same as in the RF-cavity based compressor techniques, the resolution is again limited by electronic synchronisation jitter. The cited article however claims that recent progress on synchronisation of an optical laser pulse with an electronic RF signal can limit this jitter to less than 50 fs. In the reported experiment [78] they were also limited by the size of the detector and therefore had to reduce the streaking field to limit the streak lengths so that the streaks would fit on the detector. With the reduced streaking field they only managed a calculated streak camera resolution of 400 fs. Nevertheless, by generating a 16 ps electron pulse by means of a very closely spaced train of short UV pulses they were able to investigate the structural changes within a gold film upon ultrafast heating with a laser pulse. The transients plotted [78] however, only show dynamics on the 5-10 ps time-scale so the

Stellenbosch University http://scholar.sun.ac.za

expected 400 fs resolution was not really proven.

In order to demonstrate the successful implementation of the streaked electron diffraction technique with our optically-triggered streak camera the time-resolved, photo-induced dynamics in the charge density wave compound $4H_b$-$TaSe_2$ is investigated. Because the streak camera relies on optical rather than electronic synchronization the jitter between the streaking field and the electron pulse arrival is below 100 fs [18]. This allows for performing the experiment in accumulation mode without losing temporal resolution. The dynamics observed in $4H_b$-$TaSe_2$ are also in the sub-picosecond regime (see figure 3.4) so sub-picosecond resolution can be proven .The results from the streaking experiment are also compared to the results from the conventional electron diffraction technique shown in section 3.1.

Experimental Procedure

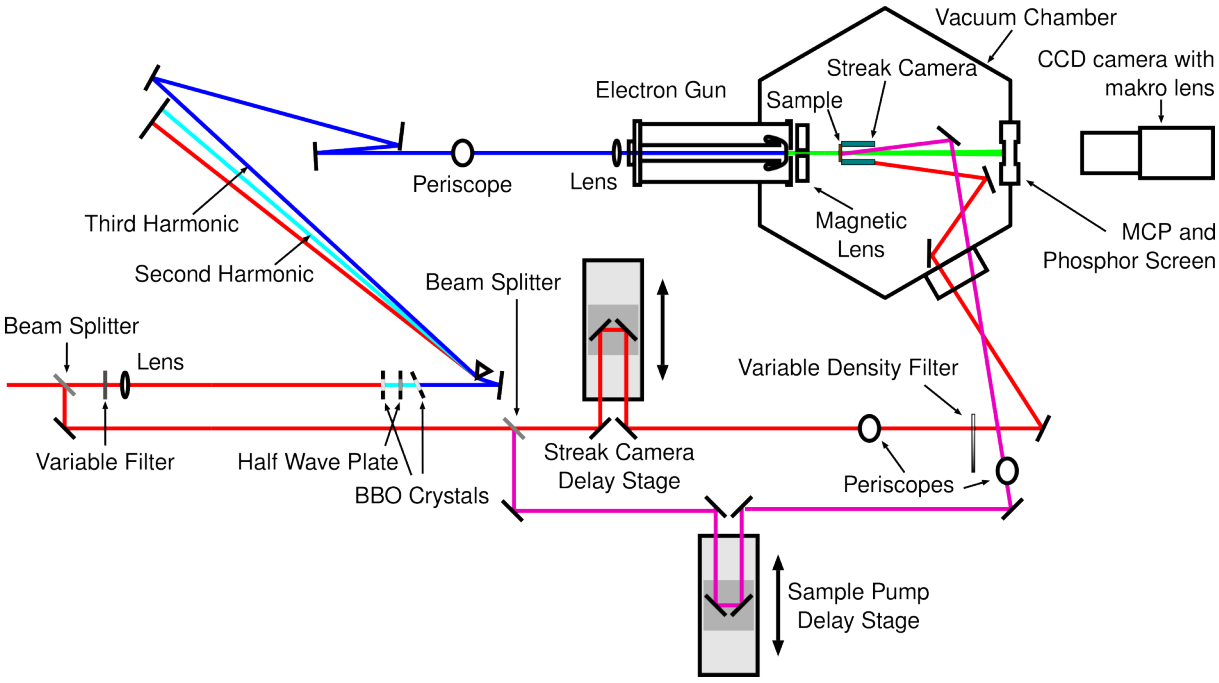

Figure 3.13: Overview of streaked diffraction setup: similar to the conventional pump-probe setup (see figure 1.1) but now two pump beams are implemented, one (red) to trigger the photo-switch of the streak camera and the other (pink) to pump the sample. The delay stage in each arm is only required to find the correct timing for all the pulses and then the delays are fixed during data collection.

The streaked electron diffraction setup is a slight modification of our existing conventional femtosecond electron diffraction setup discussed in detail in section 1.2. The amendments include: (a) one of our photo-triggered streak cameras (see figure 1.6) is

Stellenbosch University http://scholar.sun.ac.za

placed in the electron beam path after being diffracted by the sample and (b) an extra pump arm is included to trigger the streak camera (see figure 3.13). The sample and streak camera are placed 90 mm beyond the magnetic lens (see figure 3.12) to allow the electron pulse containing ∼20000 electrons to Coulomb-expand to ∼6 ps.

The 100 nm thick 4*Hb*-$TaSe_2$ sample is mounted directly on the streak camera's 100 μm entrance aperture located 2 mm in front of the streaking plates which have a slight increase in separation to 600 μm, allowing several diffraction orders to be streaked without being clipped on the plates. The distance between the streak camera and MCP detector is 300 mm. The streak plates were charged to 700 V and the trigger laser pulse is timed such that the temporal center of the electron pulse passes the streak camera at the E = 0 position (zero deflection) of the first oscillation so that streaking occurs during the most linear section of the oscillation (see figure 1.7).

Finally, the other pump beam is used to excite the 4*Hb*-$TaSe_2$ sample. The pump fluence was adjusted to 4 mJ/cm^2 to ensure full suppression of the CDW signal (see figure 3.8) and therefore maximised the signal to be observed. The pump pulse incidents on the sample between the streak plates counter propagating to the electron pulse. The delay stage timing is adjusted so that the pump pulse arrives at the sample after roughly a fifth of the electron pulse has been transmitted (see figure 3.11).

All three laser pulses, UV for photo-cathode, trigger for streak camera and pump for sample, are split from one master pulse and delayed with respect to each other by mechanical translation stages (see figure 3.13). Their temporal correlation and low-jitter of the streaking device enables in optimum temporal resolution of the entire setup of 150 fs.

Data Extraction Procedure

Shown in figure 3.14 (b) is the streaking effect on the diffraction pattern once the streaking voltage is switched on. The same *Labview* program that was used before for the conventional scanning electron diffraction was used to average over all available Bragg streaks to gain in signal-to-noise ratio. The resultant averaged image is shown in figure 3.15 (a). Here the bright Bragg streak can be seen in the center with the six surrounding CDW streaks not really visible due to their much lower intensity. With an adjusted intensity scaling of the 16-bit image, one of the six CDW streaks is displayed in panel (b) with the pump beam blocked. Once the pump beam is opened, t_0 (indicated in panel (c)) is clearly visible where the CDW streak abruptly stops indicating that the CDW modulation in the crystal is completely suppressed. Panel (d) shows the resultant im-

Stellenbosch University http://scholar.sun.ac.za

age after subtracting the pumped (panel (c)) and unpumped (panel (b)) streak images from each other. The dark region emphasises the complete disappearance of the CDW streak after t_0 .

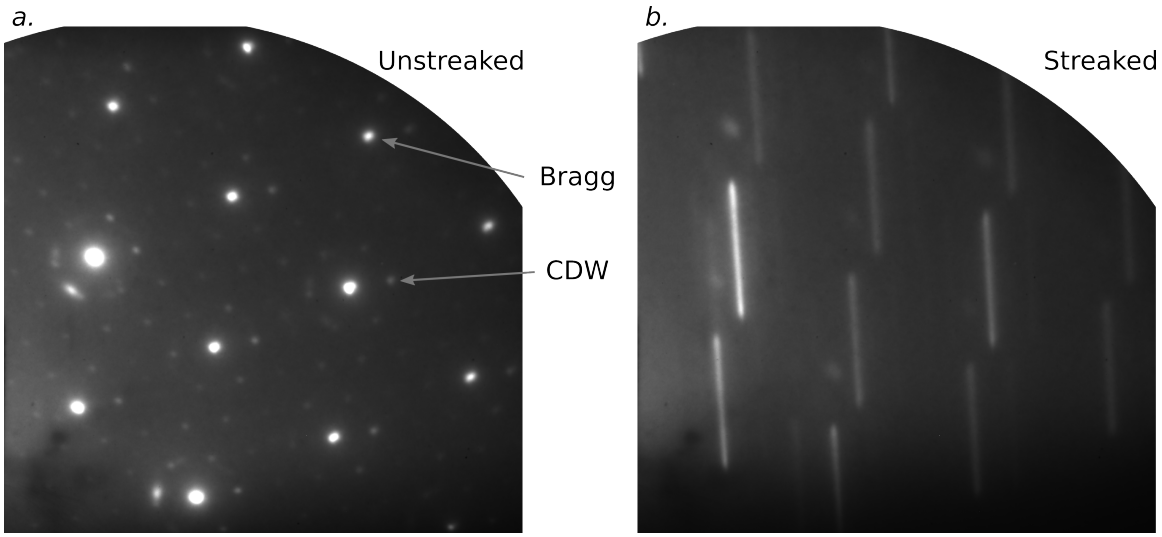

Figure 3.14: (a) Diffraction pattern of 4*Hb*-$TaSe_2$ with streak camera voltage switched off and (b) with voltage switched on.

To extract the transients from the detected Bragg and CDW streaks the following was done: the intensity profile in the vertical direction of the dotted rectangular boxes was analysed for pumped (I_p) and unpumped (I_{up}) images. The transient signals plotted in figure 3.16 are the normalised changes in scattering intensity given by equation 3.2 where as before a signal of zero indicates no change in intensity while a signal of -1 and 1 indicates a full suppression or doubling of intensity respectively. The data is also fitted with the same model explained in section 3.1 to extract time constants that can be compared with the time constants extracted in the conventional scanning experiment.

Theoretical Considerations and Performance

Three important parameters that will determine if streaked electron diffraction is able to compete with conventional femtosecond electron diffraction are: (1) the achievable temporal resolution, (2) the observable time-window per measurement and (3) the signal-to-noise ratio of the measurement.

(1) In conventional femtosecond electron diffraction the temporal resolution is determined by the convolution of the optical pump pulse and the electron probe pulse, this

Stellenbosch University http://scholar.sun.ac.za

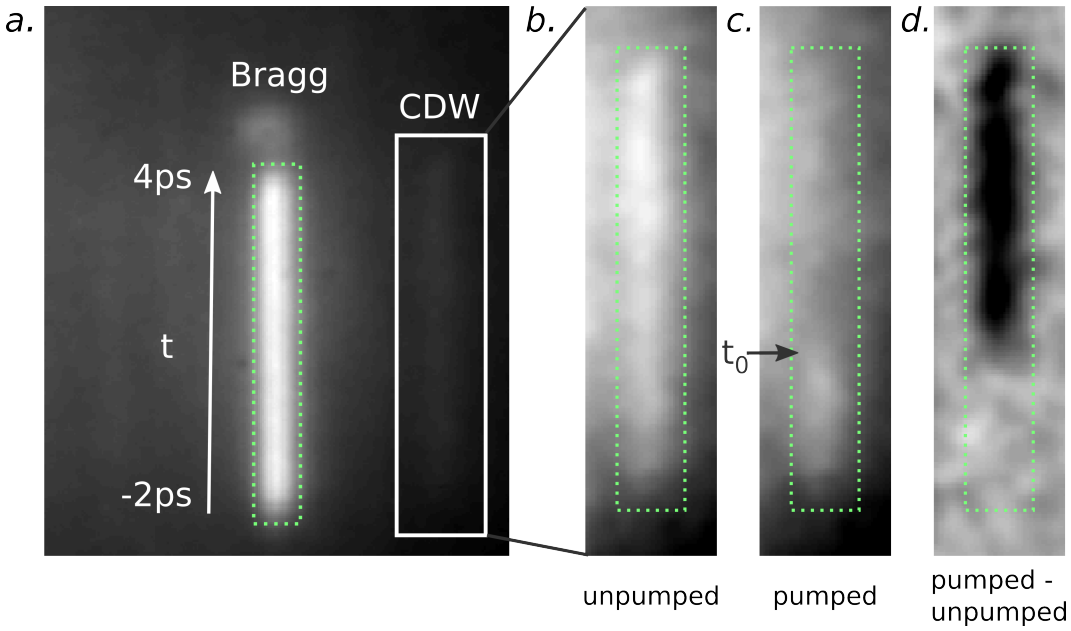

Figure 3.15: Shown in panel (a) is the result of averaging over all possible streaks shown in figure 3.12, the much fainter CDW streaks are not visible due to the intensity scaling of the 16-bit image. With an adjusted intensity scaling one of the six CDW streaks is displayed in panel (b) with panel (c) indicating the CDW streak with the pump beam on, t_0 is clearly visible. Panel (d) shows the pumped and unpumped images subtracted form each other, with the dark region emphasising a full suppression of the CDW signal after t_0.

is typically at best in the order of 500 fs. In streaked electron diffraction however, the resolution is determined by the optical pump pulse, the streak camera's resolution and the temporal jitter between the streaking field and the electron pulse arrival. The optical pump pulse will typically be in the order of 200 fs or less while the jitter of the streak camera is below 100 fs as the photo-triggered streak camera relies on optical rather than electronic synchronization [18]. The resolution of the streak camera is the ratio of the unstreaked beam's angular spread ϕ and the angular streak velocity ω_s as given by equation 1.2. The streak velocity is mainly dependent on the applied voltage and plate separation and can be directly determined through measuring the beam deflection vs. arrival time of the photo-switch trigger pulse (see section 1.3 for more details on how the angular streak velocity is determined). The angular streak velocity, with the experimental parameters as discussed previously, was measured to be 2.1 mrad/ps. The angular beam spread of both, the unstreaked Bragg and CDW diffraction spots (see figure 3.14 (a)) was measured to be 1.3 mrad. Given the above experimental conditions the expected resolution of the streak camera can be determined using equation 1.2 and was calculated to be 620 fs. Including the optical pump-pulse duration (150 fs) and the jitter (<100 fs), the overall temporal resolution of the experiment is expected to be 650 fs.

Stellenbosch University http://scholar.sun.ac.za

(2) The observable time-window of the transient is determined by the length of the incoming electron pulse, but this can not arbitrarily be made as long as desired. Since the technique is based on spatially separating different temporal components of the probe pulse on the detector the signal will be compromised if the streaks of the two adjacent diffraction spots had to overlap on the detector. The streak lengths therefore have to be limited such that no overlapping occurs (see figure 3.14 (b)). The lengths of the streaks on the detector are determined by the streaking angle, θ_{streak} while the separation of the diffraction spots is determined by the diffracting angle, θ_{diff}. To avoid overlapping of streaks, $\theta_{streak} < \theta_{diff}$. This condition can of course be relaxed if the rotation of the sample is such that the diffracting angle is not in the same plane as the streaking angle as is the case in figure 3.14 (b).

By evaluating the momentum difference, imposed by the streak camera, between the front-most and rear-most electron in the pulse it can be shown that streaking angle is given by [36]:

$$\theta_{streak} = \frac{\phi}{\Delta\tau_s}\Delta t, \tag{3.7}$$

with ϕ the angular beam spread, Δt the electron pulse length and $\Delta\tau_s$ the streak camera's response. Here the temporal resolution, $\Delta\tau_s$ is fixed by choosing the appropriate streak velocity in order to resolve the signal to be observed. The beam spread is also constant, so the only variable available to limit the streaking angle is the electron pulse duration i.e. the time-window.

The final value required to determine the maximum allowed time-window is the diffracting angle, θ_{diff}. This can be approximated using Bragg's law, $2d\sin\theta_n = n\lambda$, with $n = 1$. Imposing the limit that $\theta_{streak} \leq \theta_{diff}$ and substituting into equation 3.7 the maximum time-window is given by:

$$\Delta t = \frac{\theta_{diff}}{\phi}\Delta\tau_s. \tag{3.8}$$

Therefore a maximum time-window of between 4 and 17 ps can be expected with a beam divergence of 0.5 mrad and an electron energy of 30 keV if a sample with a crystal constant of between 10 and 2 Å is investigated and a resolution of 500 fs is required.

Equation (3.8) can now be used to verify that the choice of 6 ps for the electron pulse falls within the limit of the maximum allowed time-window to avoid the overlapping of streaks. With an atomic spacing, $d = 3.445$ Å for $4Hb$-$TaSe_2$ and the de Broglie wavelength for the 30 keV electron source being $\lambda = 0.07$ Å, we can calculate the diffraction angle, θ_{diff} to be 10.3 mrad. The maximum allowed time-window is then calculated to be 5 ps which is below but in the order of the chosen 6 ps.

Stellenbosch University http://scholar.sun.ac.za

(3) The final parameter to make the streaked diffraction technique favourable over conventional electron diffraction is the signal-to-noise ratio. As previously shown (see figure 1.8), for conventional scanning electron diffraction an electron number in the order 1000 e/pulse is required to assure pulse durations of under 500 fs at the sample. For streaked electron diffraction to have the same signal-to-noise per unit time the same number of electrons through the sample are required per unit time i.e. $\sim$1000 electrons per 500 fs. The streaking velocity also has to be such that these 1000 electrons fall on the same size area on the detector as the 1000 electrons in the unstreaked beam of the conventional experiment. In other words, the streak camera resolution should also be 500 fs such that for example a 500 fs pulse will have no significant streak length but just be a spot on the detector. If these parameters are ensured the signal-to-noise ratio per unit time in the transient will be the same for a single image. However, here comes the power of the streaking technique: because of the parallel data collecting regime the whole transient is collected in a single image as oppose to just one time-step in the conventional scanning method. In order to obtain a transient for the scanning method several images have to be taken (at least one pair of images per data point). For all the images taken in scanning method the same number of images can be taken for the streaking method (i.e. the same data collecting time) but in the streaking method each image contributes to reducing the signal-to-noise ratio of every point in the transient.

This is more easily explained by referring to the measurements displayed in figure 3.17 (a) and (c), where the data points indicated with circles is for the streaked experiment and the triangles for the conventional scanning experiment. The data collecting times for both the streaked and the scanning experiments were equal (60 min). The electron number for the scanning experiment was 1500 electrons per pulse with a temporal duration of 500 fs at the sample. For the streaked experiment the electron number was $\sim$20 000 electrons per pulse with a pulse duration of 6 ps (i.e. $\sim$1700 electrons per 500 fs, almost the same as the scanning method) and an appropriate streak velocity to provide for a temporal resolution of 620 fs (i.e such that the 1700 electrons were "not" streaked). With these pulse parameters the number of electrons per time unit in all transients is therefore equal. For the data analysis of the Bragg transients the same number of peaks was averaged for both methods, which now allows for the comparison of the signal-to-noise ratios. Since in the 60 min data collecting time, 30 pumped and 30 unpumped images could be taken (each pair giving one data point in the scanning method) the signal-to-noise of the streaked experiment is expected to be $\sqrt{30} \approx 5.5$ times better. At first glance this is indeed the case when comparing the transient Bragg signals in figure 3.17 (a) (the exact numbers are calculated in the next section). The improved signal-to-noise ratio for the CDW transients is not as evident,

Stellenbosch University http://scholar.sun.ac.za

because for the streaked experiment only one out of the six satellites could be analysed compared to all six well separated CDW peaks in the scanning experiment. Therefore the signal-to-noise ratio for the streaked CDW transient is expected to be only $\sqrt{30/6} \approx 2.2$ better. Comparing the transients in figure 3.17 (c) it does seem that this is the case.

Results and Discussion

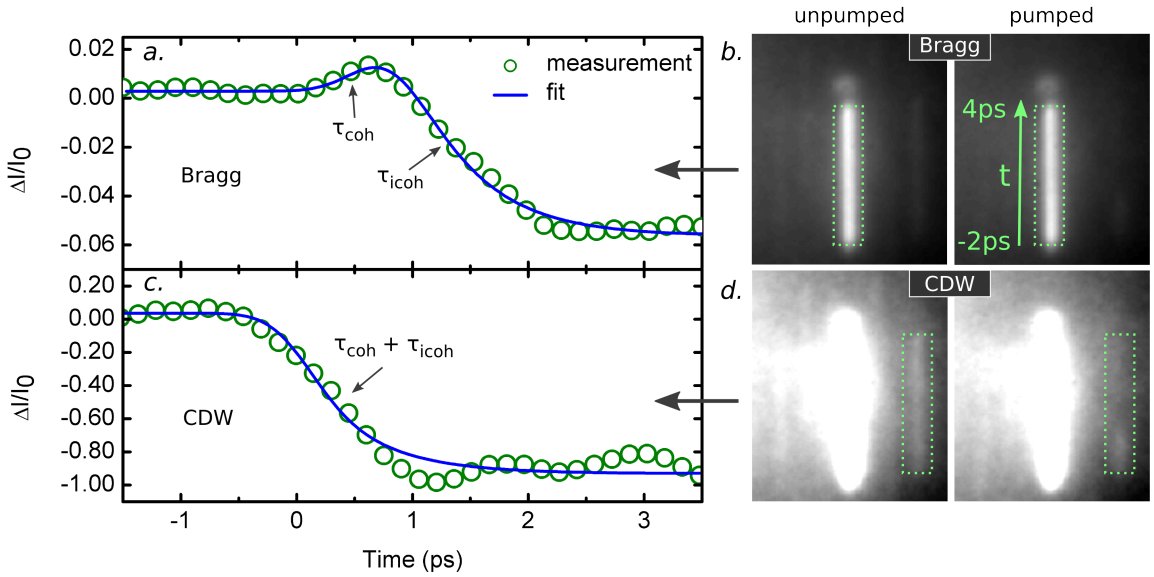

Figure 3.16: Plotted are the transient streak profiles of the Bragg (a) and the CDW (c) signals. The extracted time constant for τ_{icoh} from the fits (see section 3.1 and equation 3.3) is 550 fs for both the Bragg and CDW signals. This value agrees with the 550 fs obtained for the conventional scanning experiment. Insets (b) and (d) show the pumped and unpumped images intensity-scaled for easier identification of the Bragg and CDW signals respectively. With only a few percent change in the Bragg signal it is not possible to see any changes in the images but the sudden drop at t_0 of the CDW signal is clearly visible in panel (d).

Plotted in figure 3.16 are the transient streak profiles of the Bragg (a) and the CDW (c) signals. As in the conventional scanning experiment, an initial rise of a few percent then decay to below its original value is seen in the Bragg signal. The CDW signal decays to -1 (i.e. zero intensity) within 1-2 ps and remains that way for the displayed future time. The model that explains these trends in both the Bragg and CDW signal is discussed extensively in section 3.1. The fitted curves are from this model (see equation 3.3) and, after fixing $\tau_{coh} = 120$ fs as before and deconvolving with a Gaussian function with a FWHM = 660 fs to account for the overall temporal resolution of the setup, a time constant for the incoherent electron-phonon relaxation processes $\tau_{icoh} = 550$ fs

Stellenbosch University http://scholar.sun.ac.za

for both the Bragg and CDW transients was extracted. This value agrees with the 550 fs obtained for the conventional scanning experiment.

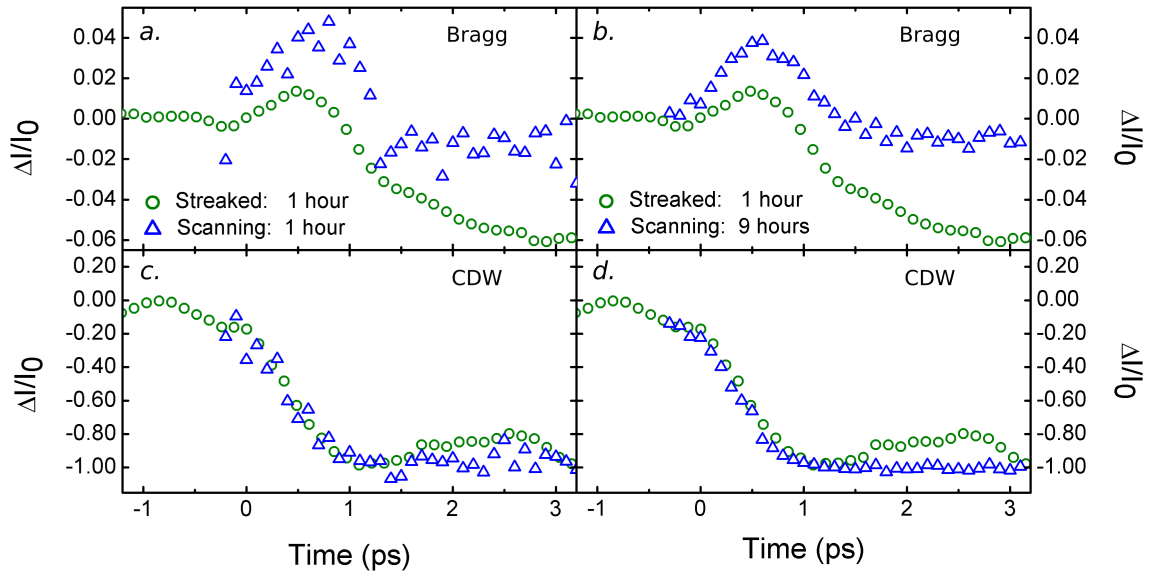

Figure 3.17: Plotted are the obtained transient signals of the Bragg and CDW peaks from the streaked experiment (green circles) and from the conventional scanning experiment (blue triangles). In panel (a) and (c) the data collecting time for both methods is equal (1 hour) and in panel (b) and (d) the data collecting time for the scanning experiment is 9 times longer (1 hour vs. 9 hours). With the same data collecting time there is a significant improvement in signal-to-noise ratio for the streaked experiment (see argument (3) in previous subsection)

In figure 3.17 the results from the streaked experiment are now more closely compared with the results from the scanning experiment. Included in the plots, are transients from the conventional scanning experiment for a pump fluence of 2.6 mJ/cm^2 (similar to the red curves in figure 3.6 but now averaging over only one "scan" as opposed to averaging over six "scans" previously). In panel (a) and (c) the data collecting time for both methods is equal and in panel (b) and (d) the data collecting time for the scanning experiment is 9 times longer than that of the streaking method.

The transients from the two techniques are similar, especially for the CDW signal where they are almost exactly the same. For the Bragg signal, at time-zero, a rise of only about 2% is observed instead of the 4% observed with the conventional femtosecond electron diffraction technique while the drop of 6% in the Bragg signal at 2-3 ps, due to the incoherent electron-phonon relaxation processes (Debye-Waller effect), is significantly more than the 1% drop observed previously. The more pronounced drop is probably due to the higher pumping fluence of 4 mJ/cm^2 vs. 2.6 mJ/cm^2 where

Stellenbosch University http://scholar.sun.ac.za

more energy is dumped into the electronic system and then transferred to the lattice through electron-phonon coupling.

As discussed before in point (3) of the previous subsection, the signal-to-noise ratio of the Bragg signal in the streaked diffraction vs. scanning experiment can now be compared. Plotted in figure 3.18 (a) and (b) are the Bragg signals for the scanning and streaking methods, respectively (the same data as in figure 3.17 (a)). This is the data from the same data collecting time and the signal-to-noise for the streaking method is expected to be 5.5 time better (see previous subsection - point (3)). Included in the plots are the fitted curves of the scanning measurement in figure 3.4 and streaking measurement in figure 3.16. Subtracting the data from the fitted curves gives the deviation from the fit and the standard deviation σ for each method is also indicated (see panel (c) and (d)). The improvement in signal-to-noise is then $\frac{\sigma_{scanning}}{\sigma_{streaking}} = \frac{0.0113}{0.0023} = 4.9$ which agrees well with the predicted value. Only after acquiring data for 9 hours does the signal-to-noise of the scanning experiment become comparable to the 1 hour collected streaked data (see figure 3.17 (b)).

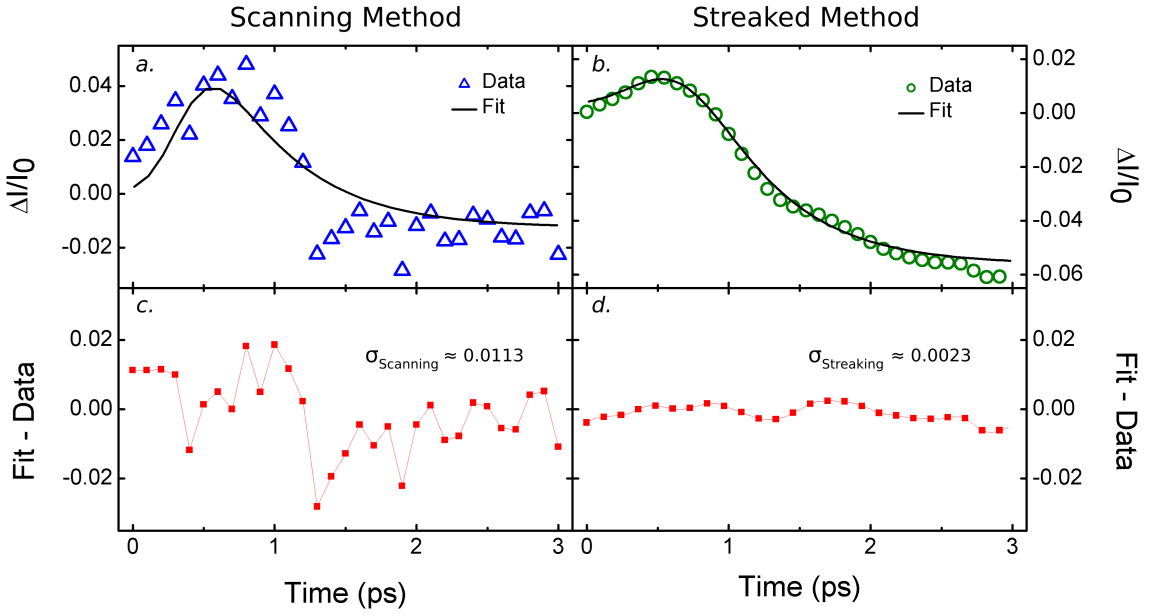

Figure 3.18: Plotted in figure are the Bragg signals for the scanning (a) and streaking (b) methods, respectively (the same data as in figure 3.17 (a)). Include in the plots are the fitted curves (solid black lines). Subtracting the data from the fitted curves (see panel (c) and (d)) gives the deviation from the fit and the standard deviation σ for each method is also indicated.

One more point of discussion is the appearance of an extra spot above all the streaks (see figures 3.14 (b) and 3.15 (a)). This is probably due to a double reflection of the electron generating UV pulse from the photo-cathode's front and back surface. This is

Stellenbosch University http://scholar.sun.ac.za

motivated by the following: (a) The number electrons generated form this extra pulse would be a small fraction of the main electron pulse. Very few electrons would result in very little Coulomb explosion and hence a short ($<$ 500 fs) electron pulse at the streak camera. With the resolution of the streak camera of 620 fs the extra spot above the main streak will have no streak length, which is the case. (b) The photo-cathode is 1 mm thick which means the extra UV pulse will be delayed by $2 \times 3.3 = 6.6$ ps, which in turn has two consequences. The generated electron pulse will have a delayed arrival time at the streak camera of 6.6 ps. If the streak in figure 3.15 (a) is 6 ps long then the delay between the center of the main electron pulse and the extra electron pulse is in the order of 6 ps. The extra 2 mm the UV pulse travelled will also mean that the coherence length of this extra electron pulse will be worse (see figure 1.10) since the extra electron pulse will not be generated at the focus of the UV beam. It does appear that the extra spot is slightly broader than the width of the streak which would be consistent with the coherence argument.

Closing remarks

The next obvious step is to improve the signal-to-noise ratio even further by trying to increase the electron number per unit time. The experimental procedure made use of the severe Coulomb repulsion within the pulse by generating a highly charged electron bunch ($\sim$20000 e/pulse) at the photo-cathode. This made it possible to achieve the electron pulse duration of 6 ps at the sample. Using the approach of utilising the Coulomb explosion has the problem that further increase in the electron number also increases the pulse duration which in turn counteracts the effort of obtaining more electrons per unit time. A different approach would be to first stretch the 200 fs UV to the desired electron pulse duration. This approach would have the advantage that the electron pulse duration and electron number within the pulse could be adjusted more independently and therefore it will be possible to have more control over the number of electrons per unit time.

For the results shown in figure 3.16 a temporal resolution of $\sim$700 fs with a time-window of 6 ps was demonstrated but calculations show that a resolution of 250 fs with a maximum time-window of around 2 ps should be achievable with a streak plate voltage of 1000 V and a streak plate separation of 250 μm. These streak camera parameters are realistically possible. A larger time-window than 2 ps would also possible if the orientation of the sample is adjusted to avoid the overlapping of streaks.

Stellenbosch University http://scholar.sun.ac.za

Summary and Conclusion

In the first chapter of this thesis, the experimental components and technique required to perform a successful femtosecond electron diffraction experiment were covered. Additionally, two important parameters of the probing electron pulse were experimentally determined: the pulse duration at the sample and the transverse coherence length of the electrons. The pulse duration was measured using an in-house developed, low-jitter, photo-triggered streak camera and it was shown that the pulse duration is highly dependent on the electron number and distance of propagation (see figure 1.8). Using the streak camera it was experimentally verified that with an electron number of 1000 e/pulse, an electron pulse duration of <500 fs was possible at the sample position. The electron pulse duration ultimately limits the total temporal resolution of the experiment. The transverse coherence length of the beam was experimentally shown to be around 10 nm (see figure 1.10). Chapter 1 was concluded by discussing several sample preparation techniques.

In the second chapter the broader concept of strongly correlated materials, and more specifically charge density wave materials, was introduced. The properties of the investigated charge density wave material $4H_b$-$TaSe_2$ was then discussed in greater detail. Chapter 2 was concluded by briefly motivating why time-resolved measurements are important to gain a deeper understanding behind the reason for CDW formation within the investigated material.

Chapter three was the main experimental chapter where two techniques were used to investigate the sub-picosecond structural evolution of $4H_b$-$TaSe_2$ upon photo-excitation. More specifically, the structural changes within the crystal lattice were monitored while optically driving the commensurate (C) to incommensurate (IC) charge density wave (CDW) phase transition in the T-layers (see figure 2.6). The first method, conventional scanning Femtosecond Electron Diffraction (FED), was used as the main investigating tool while a new approach namely Femtosecond Streaked Electron Diffraction (FSED) was an attempt at significantly increasing the signal-to-noise ratio of the transient signals for the same data acquisition time.

Stellenbosch University http://scholar.sun.ac.za

For the more established conventional scanning method the experimental results had three main findings:

(1) The periodic lattice distortion (PLD) associated with the CDW is destroyed via two processes after photo excitation (see figure 3.4): a coherent and incoherent process. Initial e-e scattering drastically modifies the electron density distribution which in turn smears out the inter-atomic potential related to the CDW periodicity. This causes a coherent relaxation or 'breathing" mode of the 13 Ta atoms back to their original unclustered positions. This process occurs within the temporal resolution of 400 fs of our experiment and could not be resolved. Electron-phonon coupling causes an incoherent vibration of the lattice and also contributes to the destruction of the CDW. This process was found to occur on a time-scale of 550 fs indicating strong electron-phonon coupling.

(2) The recovery time of the perturbed CDW was found to be 150 ps (see figure 3.7), much longer than the recovery time of 4 ps in a previous femtosecond electron diffraction study of 1T-TaS_2. This was attributed to the shielding effect of the non-CDW carrying H-layers present 4H_b-$TaSe_2$ which are not found in 1T-TaS_2. This decoupling of the CDW carrying T-layers results in in a less stable CDW and hence the longer recovery time. However, the decoupling of the CDW carrying T-layers also results in the lowering of the dimensionality of the system which contradicts the classical picture of lower dimensionality favouring CDW formation. These new results support other recent studies that challenge this classical picture of CDW formation.

(3) Measurements of the suppression of the CDW as a function of pumping fluence (see 3.8) showed that a pumping fluence of above 2.5 mJ/cm^2 was sufficient to completely destroy the CDW. Calculations showed that at this fluence the deposited energy is enough to raise the temperature of the sample to 410 K, the phase transition temperature. Extracting the amplitude of the CDW modulation (i.e. energy gap) from the same data showed that BCS theory, which is used to describe the energy gap in a superconductor as a function of temperature, perfectly fits our data. This could suggest that BCS theory could be applied in describing the energy gap formation associated with the CDW formation in CDW materials.

The section was concluded with some suggestions for future experiments.

For the streaked electron diffraction method, we were able to reproduce the transients of the Bragg and CDW diffraction signals from the conventional scanning method. A temporal resolution of 660 fs was demonstrated which was similar to the achievable temporal resolution of 500 fs in the conventional scanning method. However, because of the parallel data-collecting approach of the streaking method, a significant improve-

Stellenbosch University http://scholar.sun.ac.za

ment in the signal-to-noise ratio by a factor of $\sim$5 was demonstrated with the same data-collecting time (see figure 3.17). The method still shows great maturing potential and the section was concluded by suggesting the ways to further improvement in signal-to-noise ratio and to sub-250 fs resolution.

In conclusion, using two techniques that employ electron bunches as a probing source and ultrashort optical pulses as a means of instigating a phase transition, the structural dynamics were directly observed with a resolution of 400 fs in a relatively complex system as it undergoes a phase transition to a new state. The experiment, in respect of the complexity of the investigated system and the quality of the collected data, was on par with other leading research outputs using femtosecond electron or x-ray probes. The experimental measurements and analysis took over a year to master but the experimental setup is now fully operational and with the newly gained experience a system with similar complexity could be investigated in a much shorter time-span.

Stellenbosch University http://scholar.sun.ac.za

Appendices

Stellenbosch University http://scholar.sun.ac.za

A. Appendix

A.1 Data Extraction Procedure for conventional FED

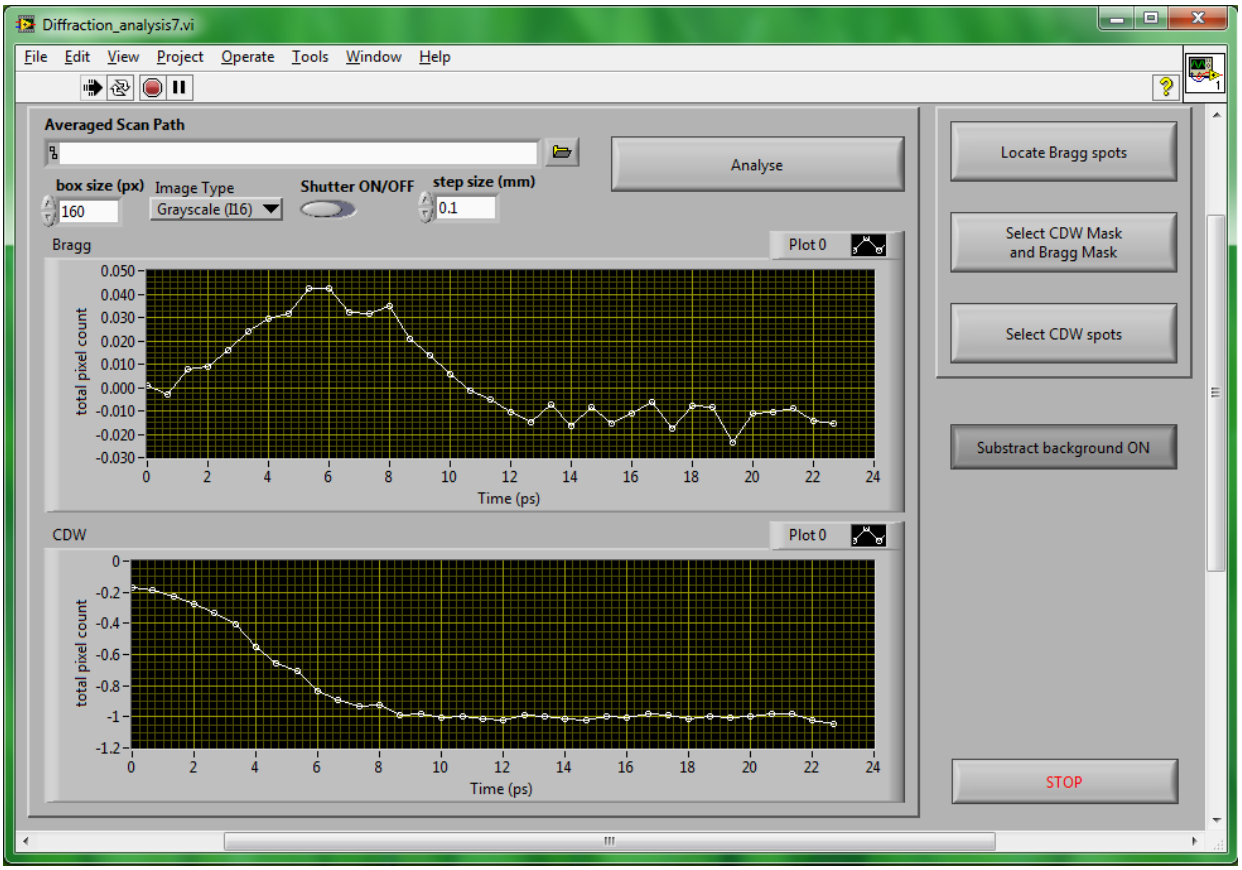

Figure A.1: The user front-end of the *Labview* program written to extract the data from the diffraction images as explained in Chapter 3.1. A folder with all the "pumped" and "unpumped" images can be selected, the Bragg peak positions detected and selected (see figure 3.1), the appropriate masks chosen and the transient signals for the Bragg and CDW peaks obtained as shown in the two plots.

Stellenbosch University http://scholar.sun.ac.za

A.2 Fitting Procedure for Transients

Below is the *Matlab* code for fitting the transients with the model given by equation 3.3.

```
%% import data from csv %%
data = importdata('data.csv');

time = data(:,1); % time
sig = data(:,2); % signal

%% fit initial guess values %%
A = 0.006;
tau_coh = 0.15; % ps
B = -0.007;
tau_icoh = 0.4; % ps
time_shift = -0.5; % ps
int_shift = 0.00005;

initial_fit_par = [A,tau_coh,B,tau_icoh,time_shift,int_shift];

%% fit data %%
lb=[-inf 0.11 -inf 0.2 -inf -inf]; % lower bound fitting parameter
ub=[inf 0.12 inf 1 inf inf]; % upper bound fitting parameter
final_fit_par = lsqcurvefit(@my_fit,initial_fit_par,time,sig,lb,ub)

%% plot data with final fit%%
final_fit = my_fit(final_fit_par,time);
figure
plot(time,sig,'o',time,final_fit,'*')

%% export fit transient as txt %%
dlmwrite('fit.txt', [time, final_fit] ,'delimiter','\t', 'newline','pc');
```

```
function fit_function = my_fit(par,t);

a = par(1);
t_coh = par(2); % ps
b = par(3);
t_icoh = par(4); % ps
t_shift = par(5); % ps
i_shift = par(6);
```

Stellenbosch University http://scholar.sun.ac.za


```
SR = 0.62; %system response FWHM in ps

%% generate step fucntion used to make all values before t0 = 0 %%
step_func = 0.5*(tanh(1000*(t+t_shift))+1);

%% two exponentials for fit %%
coh = a*(1-exp(-(t+t_shift)/t_coh));
icoh = b*(1-exp(-(t+t_shift)/t_icoh));

%% sum of exponentials, multiplied with step function %%
fit = step_func.*(coh+icoh) + i_shift;

%% fit function convoluted with temporal response of experiment %%
SR_gauss = exp(-4.*log(2)...
    .*((t-(max(t)+min(t))/2)./SR).^2); % guassian with FWHM = SR
fit_function = my_conv(t,fit,SR_gauss)';
```

Stellenbosch University http://scholar.sun.ac.za

A.3 Data Extraction Procedure for Streaked Diffraction

Below is the *Matlab* code for extracting the transients from the streaked diffraction images.

```
close all;
clc;

%% read in pumped and unpumped images %%
p = double(imread('C:\Streak Diffraction\p', 'png'));
u = double(imread('C:\Streak Diffraction\u', 'png'));

figure('Name','unpumped image scaled for CDW');
clims=[2000 12000];
imagesc(u,clims);
axis equal; colorbar;
colormap(gray);

figure('Name','unpumped image scaled for Bragg');
clims=[0 50000];
imagesc(u,clims);
axis equal; colorbar;
colormap(gray);

%% area for CDW %%
cdw_y1=66;
cdw_y2=317;
cdw_x1=304;
cdw_x2=316;

%% area for Bragg %%
bragg_y1=66;
bragg_y2=317;
bragg_x1=205;
bragg_x2=233;

%% shift for background area %%
bg_shift_cdw = 16;
bg_shift_bragg = 28;

%% masks for CDW %%
new_image = u;
new_image(cdw_y1:cdw_y2, cdw_x1:cdw_x2) = 5000;
new_image(cdw_y1:cdw_y2, cdw_x1+bg_shift_cdw:cdw_x2+bg_shift_cdw) = 5000;
```

Stellenbosch University http://scholar.sun.ac.za


```
new_image(cdw_y1:cdw_y2, cdw_x1-bg_shift_cdw:cdw_x2-bg_shift_cdw) = 5000;
figure('Name','masks for CDW');
clims=[2000 12000];
imagesc(new_image,clims);
axis equal; colorbar;
colormap(gray);

%% masks for bragg %%
new_image = u;
new_image(bragg_y1:bragg_y2, bragg_x1:bragg_x2) = 25000;
new_image(bragg_y1:bragg_y2,...
    bragg_x1+bg_shift_bragg:bragg_x2+bg_shift_bragg) = 25000;
new_image(bragg_y1:bragg_y2,...
    bragg_x1-bg_shift_bragg:bragg_x2-bg_shift_bragg) = 25000;
figure('Name','masks for Bragg');
clims=[0 50000];
imagesc(new_image,clims);
axis equal; colorbar;
colormap(gray);

%% pump profile for CDW %%
p_profile_cdw = mean((p(cdw_y1:cdw_y2, cdw_x1:cdw_x2))');
p_bg_cdw1 = mean((p(cdw_y1:cdw_y2,...
    cdw_x1+bg_shift_cdw:cdw_x2+bg_shift_cdw))');
p_bg_cdw2 = mean((p(cdw_y1:cdw_y2,...
    cdw_x1-bg_shift_cdw:cdw_x2-bg_shift_cdw))');
p_bg_cdw = (p_bg_cdw1+p_bg_cdw2)./2;
p_signal = p_profile_cdw-p_bg_cdw;

%% unpump profile for CDW %%
u_profile_cdw = mean((u(cdw_y1:cdw_y2, cdw_x1:cdw_x2))');
u_bg_cdw1 = mean((u(cdw_y1:cdw_y2,...
    cdw_x1+bg_shift_cdw:cdw_x2+bg_shift_cdw))');
u_bg_cdw2 = mean((u(cdw_y1:cdw_y2,...
    cdw_x1-bg_shift_cdw:cdw_x2-bg_shift_cdw))');
u_bg_cdw = (u_bg_cdw1+u_bg_cdw2)./2;
u_signal = u_profile_cdw-u_bg_cdw;

%% CDW transient signal
final_signal_CDW = (p_signal-u_signal)./u_signal;
x_CDW = (1:length(final_signal_CDW));
figure('Name','CDW');
plot(x_CDW,final_signal_CDW);

%% export CDW transient as txt %%
```

Stellenbosch University http://scholar.sun.ac.za


```
dlmwrite('CDW.txt',flipud(final_signal_CDW),...
    'delimiter','\t','newline','pc');

%% pump profile for Bragg %%
p_profile_bragg = mean((p(bragg_y1:bragg_y2, bragg_x1:bragg_x2))');
p_bg_bragg1 = mean((p(bragg_y1:bragg_y2,...
    bragg_x1+bg_shift_bragg:bragg_x2+bg_shift_bragg))');
p_bg_bragg2 = mean((p(bragg_y1:bragg_y2,...
    bragg_x1-bg_shift_bragg:bragg_x2-bg_shift_bragg))');
p_bg_bragg = (p_bg_bragg1+p_bg_bragg2)./2;
p_signal = p_profile_bragg-p_bg_bragg;

%% unpump profile for Bragg %%
u_profile_bragg = mean((u(bragg_y1:bragg_y2, bragg_x1:bragg_x2))');
u_bg_bragg1 = mean((u(bragg_y1:bragg_y2,...
    bragg_x1+bg_shift_bragg:bragg_x2+bg_shift_bragg))');
u_bg_bragg2 = mean((u(bragg_y1:bragg_y2,...
    bragg_x1-bg_shift_bragg:bragg_x2-bg_shift_bragg))');
u_bg_bragg = (u_bg_bragg1+u_bg_bragg2)./2;
u_signal = u_profile_bragg-u_bg_bragg;

%% Bragg transient signal %%
final_signal_bragg = (p_signal-u_signal)./u_signal;
x_bragg = (1:length(final_signal_bragg));
figure('Name','Bragg');
plot(x_bragg,final_signal_bragg);

%% export Bragg transient as txt %%
dlmwrite('Bragg.txt',flipud(final_signal_bragg),...
    'delimiter','\t','newline','pc');
```

Stellenbosch University http://scholar.sun.ac.za

Bibliography

[1] R. Peierls. *Quantum Theory of Solids*. Oxford University Press (1956).

[2] J. Wilson, F. Di Salvo, and S. Mahajan. Charge-density waves and superlattices in metallic layered transition metal dichalcogenides. *Advances in Physics*, **50**:1171 (1975).

[3] F. Di Salvo and T. Rice. Charge-density waves in transition-metal compounds. *Physics Today*, **32**:32 (1979).

[4] A. Zewail. Femtochemistry: Atomic-Scale Dynamics of the Chemical Bond Using Ultrafast Lasers. In *Nobel Lectures, Chemistry 1996-2000*, pages 274–367. World Scientific Publishing Co. (2003).

[5] M. Silies, H. Witte, S. Linden, J. Kutzner, I. Uschmann, et al. Table-top kHz hard X-ray source with ultrashort pulse duration for time-resolved X-ray diffraction. *Applied Physics A*, **96**:59 (2009).

[6] F. Zamponi, Z. Ansari, C. Korff Schmising, P. Rothhardt, N. Zhavoronkov, et al. Femtosecond hard X-ray plasma sources with a kilohertz repetition rate. *Applied Physics A*, **96**:51 (2009).

[7] R. Schoenlein, S. Chattopadhyay, H. Chong, T. Glover, P. Heimann, et al. Generation of femtosecond pulses of synchrotron radiation. *Science*, **287**:2237 (2000).

[8] S. Khan, K. Holldack, T. Kachel, R. Mitzner, and T. Quast. Femtosecond Undulator Radiation from Sliced Electron Bunches. *Physical Review Letters*, **97**:074801 (2006).

[9] T. Elsaesser and M. Woerner. Photoinduced structural dynamics of polar solids studied by femtosecond X-ray diffraction. *Acta crystallographica. Section A, Foundations of crystallography*, **66**:168 (2010).

[10] E. Möhr-Vorobeva, S. Johnson, P. Beaud, U. Staub, R. De Souza, et al. Nonthermal Melting of a Charge Density Wave in TiSe2. *Physical Review Letters*, **107**:036403 (2011).

Stellenbosch University http://scholar.sun.ac.za

[11] P. Emma, R. Akre, J. Arthur, R. Bionta, C. Bostedt, et al. First lasing and operation of an Angstrom-wavelength free-electron laser a. *Nature Photonics*, **4**:641 (2010).

[12] H. N. Chapman, P. Fromme, A. Barty, T. White, R. Kirian, et al. Femtosecond X-ray protein nanocrystallography. *Nature*, **470**:73 (2011).

[13] N. Erasmus. *The development of an electron gun for performing ultrafast electron diffraction experiments*. Masters thesis, Stellenbosch University, South Africa (2009).

[14] J. R. Dwyer, R. E. Jordan, C. T. Hebeisen, M. Harb, R. Ernstorfer, et al. Experimental basics for femtosecond electron diffraction studies. *Journal of Modern Optics*, **54**:923 (2007).

[15] A. Janzen, B. Krenzer, O. Heinz, P. Zhou, D. Thien, et al. A pulsed electron gun for ultrafast electron diffraction at surfaces. *The Review of Scientific Instruments*, **78**:013906 (2007).

[16] S. Nie, X. Wang, J. Li, R. Clinite, and J. Cao. Femtosecond electron diffraction: direct probe of ultrafast structural dynamics in metal films. *Microscopy research and technique*, **72**:131 (2009).

[17] B. J. Siwick, J. R. Dwyer, R. E. Jordan, and R. J. D. Miller. Ultrafast electron optics: Propagation dynamics of femtosecond electron packets. *Journal of Applied Physics*, **92**:1643 (2002).

[18] G. H. Kassier, K. Haupt, N. Erasmus, E. G. Rohwer, H. M. von Bergmann, et al. A compact streak camera for 150 fs time resolved measurement of bright pulses in ultrafast electron diffraction. *Review of Scientific Instruments*, **81**:105103 (2010).

[19] B. J. Siwick, J. R. Dwyer, R. E. Jordan, and R. J. D. Miller. An atomic-level view of melting using femtosecond electron diffraction. *Science*, **302**:1382 (2003).

[20] M. Eichberger, H. Schäfer, M. Krumova, M. Beyer, J. Demsar, et al. Snapshots of cooperative atomic motions in the optical suppression of charge density waves. *Nature*, **468**:799 (2010).

[21] T.-R. T. Han, Z. Tao, S. D. Mahanti, K. Chang, C.-Y. Ruan, et al. Structural dynamics of two-dimensional charge-density waves in CeTe3 investigated by ultrafast electron crystallography. *Physical Review B*, **86**:07514 (2012).

[22] N. Erasmus, M. Eichberger, K. Haupt, I. Boshoff, R. Birmurske, et al. Ultrafast dynamics of charge density waves in 4Hb -TaSe2 probed by femtosecond electron diffraction. *Physical Review Letters*, **109**:167402 (2012).

Stellenbosch University http://scholar.sun.ac.za

[23] G. H. Kassier, K. Haupt, N. Erasmus, E. G. Rohwer, and H. Schwoerer. Achromatic reflectron compressor design for bright pulses in femtosecond electron diffraction. *Journal of Applied Physics*, **105**:113111 (2009).

[24] S. Tokita, M. Hashida, S. Inoue, T. Nishoji, K. Otani, et al. Single-Shot Femtosecond Electron Diffraction with Laser-Accelerated Electrons: Experimental Demonstration of Electron Pulse Compression. *Physical Review Letters*, **105**:17 (2010).

[25] T. van Oudheusden, P. Pasmans, S. van der Geer, M. de Loos, M. van der Wiel, et al. Compression of Subrelativistic Space-Charge-Dominated Electron Bunches for Single-Shot Femtosecond Electron Diffraction. *Physical Review Letters*, **105**:264801 (2010).

[26] M. Gao, H. Jean-Ruel, R. R. Cooney, J. Stampe, M. de Jong, et al. Full characterization of RF compressed femtosecond electron pulses using ponderomotive scattering. *Optics Express*, **20**:12048 (2012).

[27] G. H. Kassier, N. Erasmus, K. Haupt, I. Boshoff, R. Siegmund, et al. Photo-triggered pulsed cavity compressor for bright electron bunches in ultrafast electron diffraction. *Applied Physics B*, **108** (2012).

[28] M. Gao, L. Cheng, J. Hubert, and R. J. D. Miller. Organic Conductors: Direct Observation of Molecular Motions Leading to Metallic Behaviour. *Nature*, **Submitted** (2012).

[29] R. Li, W. Huang, Y. Du, L. Yan, Q. Du, et al. Note: Single-shot continuously time-resolved MeV ultrafast electron diffraction. *Review of Scientific Instruments*, **81**:036110 (2010).

[30] U. Megerle, I. Pugliesi, C. Schriever, C. Sailer, and E. Riedle. Sub-50 fs broadband absorption spectroscopy with tunable excitation: putting the analysis of ultrafast molecular dynamics on solid ground. *Applied Physics B*, **96**:215 (2009).

[31] G. Sciaini and R. J. D. Miller. Femtosecond electron diffraction: heralding the era of atomically resolved dynamics. *Reports on Progress in Physics*, **74**:096101 (2011).

[32] H. Elsayed-Ali and J. Herman. Picosecond time-resolved surface-lattice temperature probe. *Applied Physics Letters*, **57**:1508 (1990).

[33] D. H. Dowell and J. F. Schmerge. The quantum efficiency and thermal emittance of metal photocathodes*. *Physical Review Special Topics - Accelerators and Beams*, **12**:74201 (2009).

Stellenbosch University http://scholar.sun.ac.za

[34] A. Zangwill. *Physics at Surfaces*. Cambridge University Press (1988).

[35] D. Eastman. Photoelectric Work Functions of Transition, Rare-Earth, and Noble Metals. *Physical Review B*, **2**:1 (1970).

[36] G. H. Kassier. *Ultrafast electron diffraction: source development, diffractometer design and pulse characterisation*. Doctoral thesis, Stellenbosch University, South Africa (2010).

[37] H. D. Young and R. A. Freedman. *University Physics*. Pearson, eleventh edition (2004).

[38] M. Berger, J. Coursey, M. Zucker, and J. Chang. Stopping- Power and Range Tables for Electrons, Protons, and Helium Ions. *NIST, Physical Measurement Laboratory* (2005).

[39] Tectra Physikalische Instrumente. *MCP Data Sheet and Set-up Manual* (2007).

[40] R. L. Fork and F. A. Beisser. Real-time intensity autocorrelation interferometer. *Applied Optics*, **17**:3534 (1978).

[41] P. Wasylczyk. Ultracompact autocorrelator for femtosecond laser pulses. *Review of Scientific Instruments*, **72**:2221 (2001).

[42] B. J. Siwick, A. A. Green, C. T. Hebeisen, and R. J. D. Miller. Characterization of ultrashort electron pulses by electron-laser pulse cross correlation. *Optics Letters*, **30**:1057 (2005).

[43] C. T. Hebeisen, R. Ernstorfer, M. Harb, T. Dartigalongue, R. E. Jordan, et al. Femtosecond electron pulse characterization using laser ponderomotive scattering. *Optics Letters*, **31**:3517 (2006).

[44] C. T. Hebeisen, G. Sciaini, M. Harb, T. Dartigalongue, S. G. Kruglik, et al. Grating enhanced ponderomotive scattering for visualization and full characterization of femtosecond electron pulses. *Optics Express*, **16**:3334 (2008).

[45] Hamamatsu. *Guide to Streak Cameras* (2008).

[46] L. Bergmann and C. Schaefer. *Textbook of Experimental Physics - Optics*. Walter de Gruyter, tenth edition (2004).

[47] E. Hecht. *Optics*. Addison-Wesley Publishing Company, second edition (1987).

Stellenbosch University http://scholar.sun.ac.za

[48] M. Ligges, I. Rajkovic, P. Zhou, and O. Posth. Observation of ultrafast lattice heating using time resolved electron diffraction. *Applied Physics Letters*, **94**:101910 (2009).

[49] G. Sciaini, M. Harb, S. G. Kruglik, T. Payer, C. T. Hebeisen, et al. Electronic acceleration of atomic motions and disordering in bismuth. *Nature Letters*, **458**:56 (2009).

[50] P. P. H. Gnaegi, D. Studer, E. Bos and J. Pierson. Ultramicrotomy in biology and materials science: an overview. In *European Microscopy Congress*, page 797 (2008).

[51] H. Jean-Ruel, R. R. Cooney, M. Gao, C. Lu, M. A. Kochman, et al. Femtosecond Dynamics of the Ring Closing Process of Diarylethene: A Case Study of Electrocyclic Reactions in Photochromic Single Crystals. *Journal of Physical Chemistry A*, **115**:13158 (2011).

[52] M. Eichberger, M. Krumova, H. Berger, and J. Demsar. Sample preparation methods for femtosecond electron diffraction experiments. *Ultramicroscopy*, **online** (2012).

[53] L. Giannuzzi and F. Stevie. A review of focused ion beam milling techniques for TEM specimen preparation. *Micron*, **30**:197 (1999).

[54] J. Li, T. Malis, and S. Dionne. Recent advances in FIB-TEM specimen preparation techniques. *Materials Characterization*, **57**:64 (2006).

[55] N. Ashcroft and N. Mermin. *Solid State Physics*. Saunders College (1976).

[56] M. Wahab. *Solid State Physics - Structure and Properties of Materials*. Apha Science International Ltd., second edition (2005).

[57] R. Thorne. Charge-density-wave conductors. *Physics Today*, **49**:42 (1996).

[58] C. Kittel. *Introduction to Solid State Physics*. John Wiley & Sons, fith edition (1976).

[59] F. Karutz, J. von Schütz, H. Wachtel, and H. Wolf. Optically Reversed Peierls Transition in Crystals of Cu(dicyanoquinonediimine)2. *Physical Review Letters*, **81**:140 (1998).

[60] J. Demsar, L. Forró, H. Berger, and D. Mihailovic. Femtosecond snapshots of gap-forming charge-density-wave correlations in quasi-two-dimensional dichalcogenides 1T-TaS2 and 2H-TaSe2. *Physical Review B*, **66**:041101 (2002).

Stellenbosch University http://scholar.sun.ac.za

[61] S. Hellmann, C. Sohrt, M. Beye, T. Rohwer, F. Sorgenfrei, et al. Time-resolved x-ray photoelectron spectroscopy at FLASH. *New Journal of Physics*, **14**:013062 (2012).

[62] S. Hellmann, T. Rohwer, M. Kalläne, K. Hanff, C. Sohrt, et al. Time-domain classification of charge-density-wave insulators. *Nature Communications*, **3**:1069 (2012).

[63] E. Revolinsky, B. E. Brown, D. J. Beerntsen, and C. H. Armitage. Journal of the less-common metals 63. *Journal of Less-Common Metals*, **8**:63 (1965).

[64] J. Luedecke, S. van Smaalen, A. Spijkerman, J. L. de Boer, and G. A. Wiegers. Commensurately modulated structure of 4Hb-TaSe2 determined by x-ray crystal-structure refinement. *Physical Review B*, **59**:6063 (1999).

[65] R. Moret and E. Tronc. CDW induced atomic shifts in 4Hb-TaSe2. *Physica B+C*, **99**:56 (1980).

[66] F. Di Salvo, D. Moncton, J. Wilson, and S. Mahajan. Coexistence of two charge-density waves of different symmetry in 4Hb-TaSe2. *Physical Review B*, **14**:1543 (1976).

[67] W. G. Stirling, B. Dorner, J. Cheeke, and J. Revelli. Acoustic phonons in the transition-metal dichalcogenide layer compound, TiSe2. *Solid State Communications*, **18**:931 (1976).

[68] C. Riekel. Structure Refinement of TiSe2 by Neutron Diffraction. *Journal of Solid State Chemistry*, **17**:389 (1976).

[69] T. Nakashizu, T. Sekine, K. Uchinokura, and E. Matsuura. Raman study of charge-density-wave excitations in 4Hb-TaS2. *Physical Review B*, **29**:3090 (1984).

[70] M. D. Johannes and I. I. Mazin. Fermi surface nesting and the origin of Charge Density Waves in metals. *Physical Review B*, **77**:165135 (2008).

[71] A. R. Beal, H. P. Hughes, and W. Y. Liang. The reflectivity spectra of some group VA transition metal dichalcogenides. *Journal of Physics C : Solid State Physics*, **8**:4236 (1975).

[72] A. S. Bolgar, Z. A. Trofimova, A. V. Blinder, and A. A. Yanaki. Thermodynamic properties of tantalum diselenide over a wide temperature range. *Powder Metallurgy and Metal Ceramics*, **31**:601 (1992).

[73] M. Tinkham. *Introduction to Superconductivity*. McGraw-Hill, second edition (1996).

Stellenbosch University http://scholar.sun.ac.za

[74] H. Park, X. Wang, S. Nie, R. Clinite, and J. Cao. Direct and real-time probing of both coherent and thermal lattice motions. *Solid State Communications*, **136**:559 (2005).

[75] M. Harb, R. Ernstorfer, T. Dartigalongue, C. T. Hebeisen, R. E. Jordan, et al. Carrier Relaxation and Lattice Heating Dynamics in Silicon Revealed by Femtosecond Electron Diffraction â . *Journal of Physical Chemistry B*, **110**:25308 (2006).

[76] R. P. Chatelain, V. R. Morrison, C. Godbout, and B. J. Siwick. Ultrafast electron diffraction with radio-frequency compressed electron pulses. *Applied Physics Letters*, **101**:081901 (2012).

[77] G. Mourou and S. Williamson. Picosecond electron diffraction. *Applied Physics Letters*, **41**:44 (1982).

[78] P. Musumeci, J. Moody, C. M. Scoby, M. S. Gutierrez, M. Westfall, et al. Capturing ultrafast structural evolutions with a single pulse of MeV electrons: Radio frequency streak camera based electron diffraction. *Journal of Applied Physics*, **108**:114513 (2010).